MASTERARBEIT / MASTER'S THESIS

Titel der Masterarbeit / Title of the Master's Thesis

„Episodic Accretion on T-Tauri Stars"

verfasst von / submitted by

Ing. Bernhard Wolfgang Ratschiner, BSc

angestrebter akademischer Grad / in partial fulfilment of the requirements for the degree of

Master of Science (MSc)

Wien, 2020 / Vienna 2020

Abstract

The reason for the variability of the luminousity of T Tauri stars is still under debate. A possible explanation is a episodic accretion of protostellar disk mass onto the central protostar. In this scenario, a bi-stable disk alters between a phase of low and high accretion rate several times during it's lifetime. In the latter a huge amount of matter is accreted onto the star in comparable short time, causing an accretion outburst notable as steep rise in accretion luminousity. The FU Orionis (FUOR) and EX Orionis (EXOR) objects are well studied examples of this phenomenon. A mechanism that can be responsible for the onset of a burst is thermal instability causing a fast rise in temperature. Following the Shakura-Sunyaev viscosity description, a high temperature results in a higher local viscosity and thus in an enhanced accretion rate. In this context it is important to conduct simulations that consistently treat the inner regions of the disk, where sufficient high temperatures are achieved.

Currently applied numerical codes that facilitate the simulation of protostellar disks, utilize explicit integration schemes to solve the necessary differential equations. Such codes are not able to deal with the regions close to the star due to the Courant–Friedrichs–Lewy (CFL) condition and thus unable to consistently show the detailed time evolution of accretion outbursts.

This thesis gives an overview about stellar formation and the corresponding equations of radiation hydrodynamics (RHD), to describe viscous protostellar disks. It reviews how accretion is connected to viscosity of the disk and how magneto rotational instability (MRI) acts as viscosity. The long term evolution of the disk is calculated with an implicit 1+1D code (TAPIR). It utilizes axial-symmetry to solve the equations of radiation hydrodynamics in radial direction. The results present thermal instability as reason for a fast rise of the gas temperature close to the star. This leads to a enhanced accretion rate in a short time which manifests itself as an enhanced accretion luminousity by releasing gravitational energy. Furthermore, a detailed evolution of the accretion burst and the long-term evolution of the entire disk is presented.

Zusammenfassung

Die Ursache für die Variabilität der Leuchtkraft von T Tauri Sternen ist noch immer nicht vollständig geklärt. Eine mögliche Erklärung bietet die episodische Akkretion von Masse aus der Protoplanetaren Scheibe auf den zentralen Protostern. In diesem Zusammenhang wechselt eine bi-stabile Scheibe mehrmals während ihrer Lebenszeit zwischen einer Phase von niedriger und hoher Akkretionsrate. Im zweiten Fall wird eine große Menge an Masse in vergleichbar kurzer Zeit auf den Stern akkretiert, was einen Akkretionsausbruch zur Folge haben kann, der als merklicher Anstieg der Leuchtkraft beobachtet werden kann. Die FU Orionis (FUOR) und EX Orionis (EXOR) Objekte sind gut untersuchte Beispiele für dieses Phänomen. Ein Mechanismus, der für den Beginn eines solchen Ausbruchs verantwortlich sein kann, ist eine thermische Instabilität in der Scheibe, die für einen schnellen Anstieg der Temperatur sorgt. Folgt man der Shakura-Sunyaev-Beschreibung der Viskosität, so führt eine Erhöhung der Temperatur zu einer Erhöhung der Viskosität und damit zu einer größeren Akkretionsrate. In diesem Zusammenhang ist es wichtig Simulationen durchzuführen, die den Innenbereich der Protoplanetaren Scheiben vollständig berücksichtigen, da dort eine ausreichend hohe Temperatur erreicht werden kann.

Zurzeit verwendete numerische Schemata, die Protoplanetare Scheiben simulieren, nutzen explizite Integrations-Schemata um die nötigen Differentialgleichungen zu lösen. Mit solchen Codes ist es jedoch aufgrund der Courant–Friedrichs–Lewy (CFL) Bedingung nicht möglich, den Innenbereich der Scheibe zu berechnen und daher kann eine detaillierte zeitliche Entwicklung der Akkretionsausbrüche in diesem Ausmaß nicht gezeigt werden.

Diese Arbeit liefert einen Überblick über die Sternentstehung samt den entsprechenden Gleichungen der Strahlungshydrodynamik (RHD), die verwendet werden um viskose Protoplanetare Scheiben zu beschreiben. Sie wiederholt wie Akkretion mit der Viskosität der Scheibe zusammenhängt, und wie eine Magnetorotationsinstabilität (MRI) ähnlich wie Viskosität wirkt. Die Langzeitentwicklung der Scheibe wird mit Hilfe eines impliziten 1+1D Codes (TAPIR) berechnet. Dieser nutzt Axialsymmetrie um die Gleichungen der Strahlungshydrodynamik in radialer Richtung zu lösen. Die Resultate zeigen thermische Instabilitäten als Ursache für einen rapiden Anstieg der Temperatur nahe am Stern. Das führt in kurzer Zeit zu einer erhöhten Akkretionsrate, die sich in einem Leuchtkraftausbruch durch Freisetzen von Gravitationsenergie manifestieren. Zusätzlich wird eine detaillierte Entwicklung der Akkretionsausbrüche sowie eine Langzeitentwicklung der gesamten Scheibe präsentiert.

Danksagung

Zu Beginn möchte ich mich bei Prof. Dr. Ernst Dorfi bedanken, der mir diese Arbeit ermöglicht hat und durch dessen Wissen und Erfahrung viele Probleme gelöst werden konnten. Besonderer Dank gilt meinen Kollegen und Freunden Florian Ragossnig und Daniel Steiner. Dem Flo danke ich dafür, dass er mich mit einem großen Maß an Zeit und Geduld in allen Belangen bei dieser Arbeit unterstützt hat. Dem Daniel möchte ich dafür danken, dass er mich in die Arbeitsgruppe, damals noch als Tutor, eingeladen hat, wodurch ich den Pfad der theoretischen Astrophysik für mich entdeckt habe.

Ich bedanke mich bei meinem Großvater Ing. Gert Ratschiner und meiner Mutter Judith Ratschiner, die mich über das Studium hinweg nicht nur finanziell sondern auch mental und emotional unterstützt haben.

Weiters bedanke ich mich bei meinem Chef und Kollegen Dr. Joachim Pargfrieder dafür, dass ich mir meine Arbeitszeit so frei einteilen darf und für ein Arbeitsumfeld, das es wohl kein zweites Mal in der Privatwirtschaft gibt.

Ich möchte hier auch noch meine Studienfreunde Roman Miksch, Nikolaus Heu, Victoria Biedermann, Dr. Thomas Maindl, Ines Ringseis und Lukas Gehrig erwähnen. Egal wie das Studium sonst verlaufen wäre, wenn man solche Leute dabei kennenlernt, war es das auf alle Fälle wert. Meiner guten Freundin Gerda Planinger gilt besonderer Dank, da sie mir damals den Mut gemacht hat, mein Studium zu wechseln wodurch ich schließlich bei der Astrophysik gelandet bin. Danke auch an Georg Angerer, der in den Sommerferien 2013, nach Verlust meines HTL-Diplomzeugnisses, ermöglicht hat, dass dieses erneut ausgestellt wurde. Ohne ihn, wäre damals eine Anmeldung zu diesem Studium nicht möglich gewesen.

Zuletzt geht ein großer Dank auch an alle meine Langzeitfreunde, insbesondere Marijan Ilijasević, Rüdiger Rieder, Markus Woisetschläger, Roman Bruckböck, Daniela Fürweger, Dominik Loidl und Marion Habrina, durch die nicht nur meine Studienzeit zu einem Lebensabschnitt wurde, an den ich mich gerne zurückerinnern werde.

Ich widme diese Arbeit meinem Großvater, Ing. Gert Ratschiner († 12.01.2019).

"Ever tried. Ever failed. No matter. Try again. Fail again. Fail better."

Samuel Beckett

Contents

List of Figures

List of Tables

Chapter 1

Introduction

Stars are important and well studied objects in the universe and thus of great interest in astrophysics. These objects are born in slow rotating, dense and cold molecular clouds as a result of a gravitational collapse (Jeans 1902). The conservation of angular momentum leads to the development of a differential rotating disk of gas and dust around the still forming star (e.g Armitage 2010). In the following this disk is assumed to be the birthplace of planets.

Since stars are assumed to gain their bulk mass from accretion (Armitage 2010), and accretion is tightly coupled with the redistribution of angular momentum in the protostellar disk (DeSouza & Basu 2017), it is important to understand the physics, that drives these mechanisms. A possible explanation next to gravitational effects can be given by viscous torques. In this context magneto rotational instabilities (MRI) (Pringle 1981) are widely suggested to be responsible for turbulent viscosity in protostellar disks (Balbus & Hawley 1991). A common method to parameterize the turbulent viscosity is by using the α-viscosity according to Shakura & Sunyaev (1973).

A method to treat effects of MRI on accretion, is to divide the disk into two or more vertical layers (layered disk, Turner et al. 2014), a surface layer, where X-rays or cosmic rays are the dominant source of ionization (close to the surface) and a deep layer, where external radiation is unable to contribute to the heating and thermal ionization is prevalent. These layers can be defined by utilizing an viscosity model by means of the surface density and the disk temperature. A commonly used value range for the existence of a deep layer is a surface density of $> 10 - 100$ g cm^{-2} (e.g Armitage 2010, p. 99). While it is assumed that the surface layer is always ionized to some degree, ionization within the deep layer of the disk can only occur at a sufficient high temperature.

Parts of the disk are called MRI-active if ionized gas and dust couples with the magnetic field. Magnetic field lines are dragged along with the rotating material in the disk and thus get convoluted. Magnetic tensions try to straighten the lines again. This acts like viscosity and appears as transport of angular momentum (Balbus & Hawley 1991). MRI-inactive regions within the disk are commonly known as dead-zones. In such regions of low viscosity, material is likely to be

accumulated and hardly any angular momentum is transported. However, if the temperature in these dead-zones exceeds a certain threshold, e.g. $T_{active} = 1500$ K (Bae et al. 2013), material is rapidly ionized and a thermal instability (Bell & Lin 1994) occurs. This thermal instability is responsible for a steep rise in temperature, resulting in an enhanced mass flow (e.g. Audard et al. 2014) and the onset of a MRI in this region. If the material within the dead-zone is removed, during this phase of high accretion rate, the mass transport efficiency is reverted to its initial low value.

A rapid accretion of material onto the star eventually results in an accretion outburst (noticeable as a spike in the stellar luminosity) that are already observed (e.g. Semkov et al. 2017). The accretion outbursts are assumed to have periodical nature (Herbig 1977) what supports the assumption of a two phase mechanism (e.g. thermal instabilities) where the disk changes from a quiet phase into a eruptive phase (e.g. Turner et al. 1997).

Chapter 2

Stellar Formation

Today it is assumed (e.g. Mihalas & Binney 1981) that the interstellar medium (ISM) consists of at least 5 phases mainly depending on temperature, density, extension and degree of ionization. Prerequisite for the formation of molecular gas is atomic gas and cold, dense, molecular gas is needed to form stars. If taking the standard formation paradigm for low mass stars into account, stars form within the cores of molecular clouds of gas and dust. Molecular clouds are interstellar clouds, high in density and size. Due to these properties they provide shielding from dissociating radiation (e.g. ultra violet radiation) and permit the formation of molecules, in general H_2 (molecular hydrogen).

Figure 2.1: Color composite of optical (VIS) and near-infrared (NIR) images of the molecular cloud Bernard 68 by the 8.2m VLT ANTU telescope. Since the dust particles in the cloud absorb light at these wavelength it is completely opaque. Credits: ESO

The stability of large molecular clouds is supported by magnetic fields (affecting charged particles, ions), thermal pressure (related to the temperature by the equation of stat for gas) and rotation (outward centrifugal forces, perpendicular to the rotation axis). Two common mechanisms for the collapse are known as the Parker (e.g. Parker (1966), Parker (1967)) and Jeans instability (Jeans 1902). While Parker deals with differential vertical buoyancy of varying-density regions

along magnetic field lines parallel to the mid-plane, the theory of Jeans is about differential in-plane self-gravity of regions with varying surface density (McKee & Ostriker 2007), without consideration of magnetic field lines. It has shown, that instability mechanisms without inclusion of magnetic fields are too efficient. However to trigger a disturbance of the pressure equilibrium and thus the formation of such overdensities an initial perturbation (e.g. shocks or pressure waves from a distant supernova or a passing star) is needed. Due to that partial overdensities, different regions in the cloud satisfy the collapse criterion individually and start to collapse. This phenomenon is called fragmentation, where many small stars are formed out of one giant molecular cloud. While not on the main-sequence, the stellar system is referred to as young stellar object (YSO). The following two subsection describe the collapse of a molecular cloud to a low/intermediate-mass main-sequence star.

2.1 First collapse

The first collapse can be divided into two phases, the isothermal collapse (where fragmentation occurs) and the adiabatic collapse (where fragmentation stops). The virial theorem (Clausius 1870) which describes the equilibrium between kinetic and potential energy, reads as

$$2E_{kin} + E_{pot} = 0 \,. \tag{2.1.1}$$

By assuming an ideal gas and setting the kinetic energy equal to the thermal energy $E_{kin} = E_{th}$ one can write

$$E_{kin} = E_{th} = \frac{3}{2}nkT = \frac{3}{2}\frac{M}{\mu m_H}kT \,, \tag{2.1.2}$$

where n is the number density, k Boltzmann's constant and T the temperature. For the potential energy, hydrostatic equilibrium of a rotational symmetric spherical cloud

$$\frac{\partial P}{\partial r} = -\frac{Gm(r)\rho(r)}{r^2} \,, \tag{2.1.3}$$

and a constant density is assumed so that

$$m(r) = \frac{4}{3}\pi\bar{\rho}r^3 \,. \tag{2.1.4}$$

An infinitesimal mass element dm thus writes as

$$dm = 4\pi\bar{\rho}r^2 dr \,, \tag{2.1.5}$$

and the gravitational potential energy can be solved by using Eq. 2.1.4 and Eq. 2.1.5 so that

$$E_{pot} = E_{grav} = -\int_0^M \frac{Gm(r)}{r}dm = -\frac{3}{5}\frac{GM^2}{R} \,. \tag{2.1.6}$$

Substituting E_{pot} and E_{kin} into the virial theorem (Eq. 2.1.1) and solving Eq. 2.1.5, delivers (for a given chemical composition, density ρ and temperature T)

the Jeans stability criterion for a non-magnetized cloud. A cloud that exceeds the Jeans mass M_J (Jeans 1902) will undergo a gravitational collapse.

$$M > \mathrm{M_J} = \left(\frac{3}{4\pi\bar{\rho}}\right)^{\frac{1}{2}} \left(\frac{5\mathrm{kT}}{\mathrm{G}\mu\mathrm{m_H}}\right)^{\frac{3}{2}} \propto \rho^{-\frac{1}{2}}\mathrm{T}^{\frac{3}{2}} \qquad (2.1.7)$$

Given that the majority of young stars is found in multiple star systems (Goodwin et al. 2007) the turbulent fragmentation of clouds into individual collapsing clumps is preferred over the monolithic collapse scenario where a single cloud collapses into a giant protostar.

In the first phase, the thermal energy, that is caused by the conversion of gravitational potential energy, can be easily radiated away because dust and gas in the center of the cloud is optically thin and thus transparent to infrared wavelengths. The energy is transported radiatively what provides efficient cooling and thus the temperature of the optically thin cloud persists approximately constant (isothermal collapse). The timescale on which the gravitational collapse appears, is the free-fall timescale τ_{ff} (e.g. McKee & Ostriker 2007).

$$\tau_{\mathrm{ff}} = \sqrt{\frac{3\pi}{32\mathrm{G}\rho}} \propto \frac{1}{\sqrt{\rho}} \qquad (2.1.8)$$

Layers of a collapsing pressure-free, spherical cloud just feel the gravitational potential (collapse under self-gravity), thus falling with higher velocities than the local speed of sound towards the center. Because the core is initially more dense than the envelope, the interior collapses much faster than the surrounding. The collapse spreads from inside to outside and is often referred to as "inside-out-collapse", where a hot collapsing core is embedded in an envelope of cold molecular gas. The increase in density means a decrease of Jeans-mass for isothermy

$$\mathrm{M_J} \propto \rho^{-\frac{1}{2}}, \qquad (2.1.9)$$

and a declining free-fall time. This means that the small dense fragments start collapsing on their own and much faster than the overall cloud itself. The contraction and (the further fragmentation) also highly depends on the cooling time scale τ_{c} which is dependent on the so called cooling function $\Lambda(\mathrm{T})$.

$$\dot{\mathrm{E}}_{\mathrm{th}} = \frac{\mathrm{d}}{\mathrm{dt}}\left(\frac{3}{2}\mathrm{nkT}\right) = -\mathrm{n}^2\Lambda(\mathrm{T}) \rightarrow \tau_{\mathrm{c}} = \frac{3\mathrm{kT}}{2\mathrm{n}\Lambda(T)} \propto \frac{1}{\rho} \qquad (2.1.10)$$

As described by Rees & Ostriker (1977) and later Omukai et al. (1998) the ratio of the free-fall time scale and the cooling time scale give an important insight to the further dynamical evolution of the collapsing cloud. As long $\tau_{\mathrm{ff}} > \tau_{\mathrm{c}}$ the gas cools too quick and dynamical processes are unable to adjust the pressure configuration in a way that a hydrodynamical equilibrium can be established. Pressure that acts against gravity gets "lost" and the collapse continues at free-fall time. But as $\tau_{\mathrm{ff}} < \tau_{\mathrm{c}}$ (ineffective cooling) while the cloud cools, the cloud has enough time to regulate a stable hydrostatic configuration.

The cooling time actually decreases during the collapse as the number density increases.

- If the medium is optical thin, the energy can be radiated → efficient cooling, rapid contraction

- If the medium gets optically thick, radiation is trapped in the interior and can only escape from the surface → inefficient cooling, slow contraction

As time passes, the density of the core rises continuously and certainly the cloud gets opaque to its own infrared radiation. At this point fragmentation also stops since the rising temperature causes a rise in the Jeans mass M_J and the object developed a cold photosphere. The heat can no more be radiated and thus the temperature of the cloud increases. This phase where heat is not exchanged with the environment and increasing temperature, is called adiabatic collapse. The rising core temperature eventually is the source of thermal pressure and balances the gravitational pressure until the dynamical collapse of the core is stopped as it reaches hydrostatic equilibrium (see Eq. 2.1.3) while the outer layers continue to collapse isothermal. The YSO (young stellar object) is now called quasi-static protostellar core (protostar) and appears on the H-R-diagram (Hertzsprung Russel diagram). Shock waves, generated by still free-falling matter onto the core, cause further heating of the core. At this time accretion provides the luminosity of the protostar by converting the gravitational energy into radiation (accretion luminosity L_{acc}) and thermal energy (heats the core).

$$L_{acc} = \eta \frac{GM\dot{M}}{r} \qquad (2.1.11)$$

The factor η denotes the amount of accretion energy radiated (Hartmann et al. 2016). This parameter is often set to $\eta = \frac{1}{2}$ (Hartmann et al. 2011) and arises from the assumption that only half of the energy is converted into luminosity and the other half into thermal energy. The quantity $\dot{M}$ is the mass accretion rate. The accretion of the surrounding gas, generally happens through an accretion disk. Due to the conservation of angular momentum the initially slow rotating cloud is accelerated and centrifugal forces build up a disk rather than an spherical envelope around the small and fast rotating protostar.

2.2   Second Collapse

The shock waves increase the temperature to about 2000 K, high enough to cause the molecular hydrogen H_2 to dissociate into atomic hydrogen H (e.g Bate 2011). This causes a rise in the specific heat (rise in the degrees of freedom f) and the first adiabatic exponent Γ_1 (that is $\frac{7}{5}$ for diatomic molecules such as H_2) drops below $\frac{4}{3}$. This is a critical value for dynamic stability of the equilibrium of the spherically symmetric core

$$\Gamma_1 = \left(\frac{\partial \log P}{\partial \log \rho} \right)_S = \frac{f+2}{f}, \qquad (2.2.1)$$

meaning that the energy which is used for the dissociation does not contribute to the stabilization of the core against the gravitational collapse anymore. The so called second collapse sets in. After the dissociation stops and $\Gamma_1 = \frac{5}{3}$ (for

mono-atomic gas) the collapse stops as stability is restored. Further dynamical collapses can occur e.g. when H or He are ionized ($T \approx 10^4$ K) until the core of the protostar again reaches a hydrostatic equilibrium. The second hydrostatic core (stellar core) has developed inside the first core (e.g. Mo et al. 2010). The dynamical collapse slows down to a quasi-static contraction. This contraction is much slower than the initial collapse and happens on Kelvin-Helmholtz time scales. Thus that phase is also often referred to as Kelvin-Helmholtz contraction (e.g. Kippenhahn et al. 2012).

$$\tau_{\mathrm{KH}} = \frac{GM^2}{RL} \gg \tau_{\mathrm{ff}} \,. \tag{2.2.2}$$

The following phase is a phase of approximately constant (slightly rising) temperature but decreasing luminosity because of less surface area (decreasing radius) due to the contraction. At that point also accretion slows down and finally stops. The star is visible in optical wavelengths as its dusty envelope is dispersed, has nearly acquired its total mass and is now called a pre-main-sequence star as hydrogen burning is not just yet ignited. The main contributor to the luminosity at this stage is no more accretion but gravitational contraction (e.g. Kippenhahn et al. 2012)

$$\mathrm{L} = 4\pi \mathrm{r}^2 \sigma_{\mathrm{SB}} \mathrm{T}_{\mathrm{eff}}^4 \,. \tag{2.2.3}$$

If the temperature exceeds $5 \times 10^5 - 10^6$ K (e.g Chabrier et al. 2000) nuclear reactions start and deuterium (in low mass stars $\mathrm{M}_\star > 0.1$ $\mathrm{M}_\odot$) or hydrogen (for $\mathrm{M}_\star > 0.8$ $\mathrm{M}_\odot$) is fused into helium (^{3}He) by proton capture. The core heats while the surface cools causing the interior of the protostar to be fully convective. From Deuterium burning and only in the photosphere the energy transport remains radiative. The YSO evolves along the Hayashi line in the H-R-diagram as $\nabla > \nabla_{\mathrm{ad}}$. The nuclear energy participates in the heating of the core and thus in the core's pressure balance until the deuterium supply is exhausted and the contraction takes over again. The former convective core slowly gets dominated by radiative energy transport as the opacity $\bar{\kappa} \propto \rho \mathrm{T}^{-3.5}$ (Kramers' opacity law) decreases due to high temperatures. A star with $\mathrm{M} > 0.5$ $\mathrm{M}_\odot$ will now enter the so called Henyey track. Here, the temperature rises at approximately constant until the luminosity is dominated by nuclear fusion rather then gravitational energy. Stars with lower mass will directly enter the main-sequence after leaving the Hayashi line when hydrogen burning starts. As the core gets dense and the central temperature reaches about 10^7 K, hydrogen burning starts in the core and nuclear fusion generates the pressure that finally stops the collapse. Since pressure balances the gravitational force, hydrostatic equilibrium is now maintained over the lifetime of the star and the interior of the star is in radiative and thermal equilibrium.

Chapter 3

Eruptive Stars: Observation and Burst Mechanisms

A protostar is a young star, still embedded in its primordial molecular cloud and gaining mass due to accretion of material within its circuumstellar disk (e.g. Kippenhahn et al. 2012). That earliest phase in the stellar evolution lasts for about 0.5 Myr (e.g Dunham et al. 2014) for low-mass stars. The phase starts with the gravitational collapse of the molecular cloud to stellar densities and ends when the protostar has developed into a pre-main-sequence star.

Protostars belong to the family of variable stars. A variable star is an object that changes brightness as seen from earth, thus a variety of objects fit in the classification of Samus et al. (2001). Two different main categories, namely intrinsic and extrinsic stars, exist. While intrinsic stars alter their luminosity due to processes within the star (e.g. pulsation, explosion, accretion) extrinsic stars change because of an eclipsing event (e.g. a planet or a companion stars darkens the object as it moves in front of it). Hence, protostars belong to the class of intrinsic variable stars.

Observations show a variety in the morphology of the burst and different duration (Herbig 1977). It is assumed, that this variation depends on the mechanism that causes the outburst (Hartmann & Kenyon 1996).

3.1 Eruptive Stars

It is assumed that FU Orionis (FUOR) and EX Orionis (EXOR) stars are protostars, showing large and abrupt increases in their brightness (e.g. Nayakshin & Lodato 2012) due to a variability in the accretion rate onto the star. Depending on physical parameters of the star and the disk, the rate and luminosity of the bursts change.
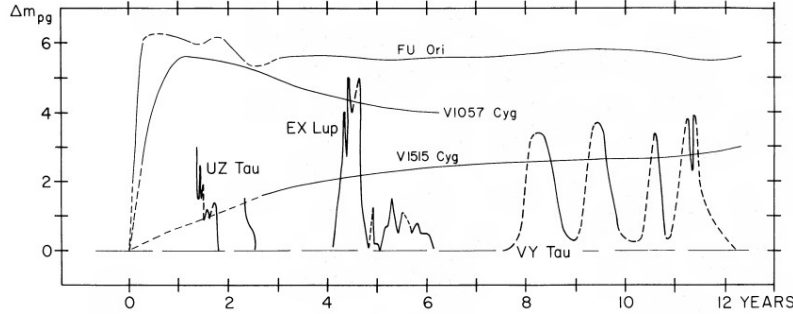
Figure 3.1: The x-Axis shows the duration of the burst and the y-axis the magnitude of the burst. A variety of eruptive variable stars showing differences in duration and burst behavior (Herbig 1977).

They show a large and abrupt increase in their brightness (Nayakshin & Lodato 2012) of about 5 mag or more (Herbig 1977), notable in the optical wavelength range. Spectral features show strong similarities to F-G super-giants in the optical (VIS) and to K-M super-giants in the near-infrared (NIR) wavelength range (Zhu et al. 2007). Both spectra are dominated by a CO overtone absorption (Zhu et al. 2007), what traces the inner hot ($1000-5000$ K) disk region (Lee et al. 2016).

It is assumed (Hartmann & Kenyon 1996) that FUOR burst are related with the transition between T Tauri stars (TTS) with disks disks and TTS with disks and envelopes, while EXOR burst are associated to instabilities within the disk.

3.1.1 Outbursts Mechanisms

A paradigm behind these outbursts is assumed to be a viscous unstable accretion disk that alters between a stable (quiescent) and an unstable (eruptive or outburst) phase (e.g. Nayakshin & Lodato 2012). Following Hartmann & Kenyon (1996), the accretion rate can alter between $\sim 10^{-7} - 10^{-4}$ M$_\odot$yr^{-1}.

The range for the origin of the burst, alters with the utilized model (Zhu et al. 2007).

- Thermal instabilities due to H$^-$ opacity in (partially) ionized inner regions < 0.1 AU of the accretion disk. Since the effective viscosity is proportional to the temperature, mass transfer can be modulated in this way to reproduced observe outbursts (Bell & Lin 1994).

- Combination of magneto-rotational instability (MRI) and gravitational instabilities (GI), where the region with higher accretion rates extend up to

0.5 AU (Armitage et al. 2001).

- Accretion of larger clumps in highly gravitational unstable accretion disks predict an inner radius of 10 AU where increased accretion rates occur (Vorobyov & Basu 2007).

Spectroscopic analysis suggests, that the innermost disk < 1 AU (Zhu et al. 2008) is the source of this variable behavior. It is assumed that such bursts can last about $10 - 100$ yr (Nayakshin & Lodato 2012) while the time for the onset of the outburst is in the order of $1 - 10$ yr (Zhu et al. 2007). Statistics suggest that a protostar undergoes about $10 - 20$ burst in its life, what is assumed to be the lower limit (Hartmann & Kenyon 1996).

3.1.2 Thermal Instabilities

Disks with low and intermediate masses (minor percentage of the stellar mass) will hardly exhibit regions that sustain gravitational instabilities. Hence, thermal instabilities are widely accepted to account as origin for FU Orionis outbursts (e.g. Turner et al. (1997), Bell & Lin (1994)). In this scenario, the protostellar disk is in an early evolution stage, still embedded in its birth cloud, while matter still falls from the cloud onto the outer edge of the disk. The distribution of mass is highly coupled to viscosity. At a certain radius close to the star, material piles up and is irradiated more effectively by the light of the central star due to the increased scale height. Hence, temperature rises up to approximately 1500 K (Bae et al. 2013) where hydrogen starts to be ionized. Following Beuther et al. (2014) the thermal instability is connected to a thermal runaway process when the hydrogen starts to be ionized. The viscous protostellar disk is thermally stable as long as the opacity changes slowly with temperature. The ionization of hydrogen leads to drastically increase in opacity with temperature. Hence, a slight increase in temperature leads to an huge amount of energy trapped with in the disk. This leads again to an increase in temperature and results in a thermal runaway. Since viscosity is proportional to temperature (Shakura & Sunyaev 1973)

$$\nu = \alpha \frac{c_S^2}{\Omega} \propto \alpha \frac{T}{\Omega} \, , \tag{3.1.1}$$

a high disk temperature can lead to a high accretion rate.

3.2   Protostellar Disk

As described in the previous chapter, disks are assumed to form as a natural result
of the star formation. As described by e.g. Vorobyov & Pavlyuchenkov (2017),
massive disks change between gravitative stable and unstable periods. While
their stable state the disks appear to be radial symmetric. Even if they become
unstable in outer parts of the disk, the inner most parts still stay stable, because
they hardly become Toomre unstable (Toomre 1964) due to high temperatures
and velocities in these regions. Hence, it is assumed, that they still preserve radial
symmetry. A recent ALMA survey (see. Figure 3.2) supports this assumption.
About 80% of the observed disks show radial symmetry. The remaining 20% are
either too large and heavy and became gravitational unstable or the star resides
in a multi-star system and gravitational or tidal forces disrupted the disk.
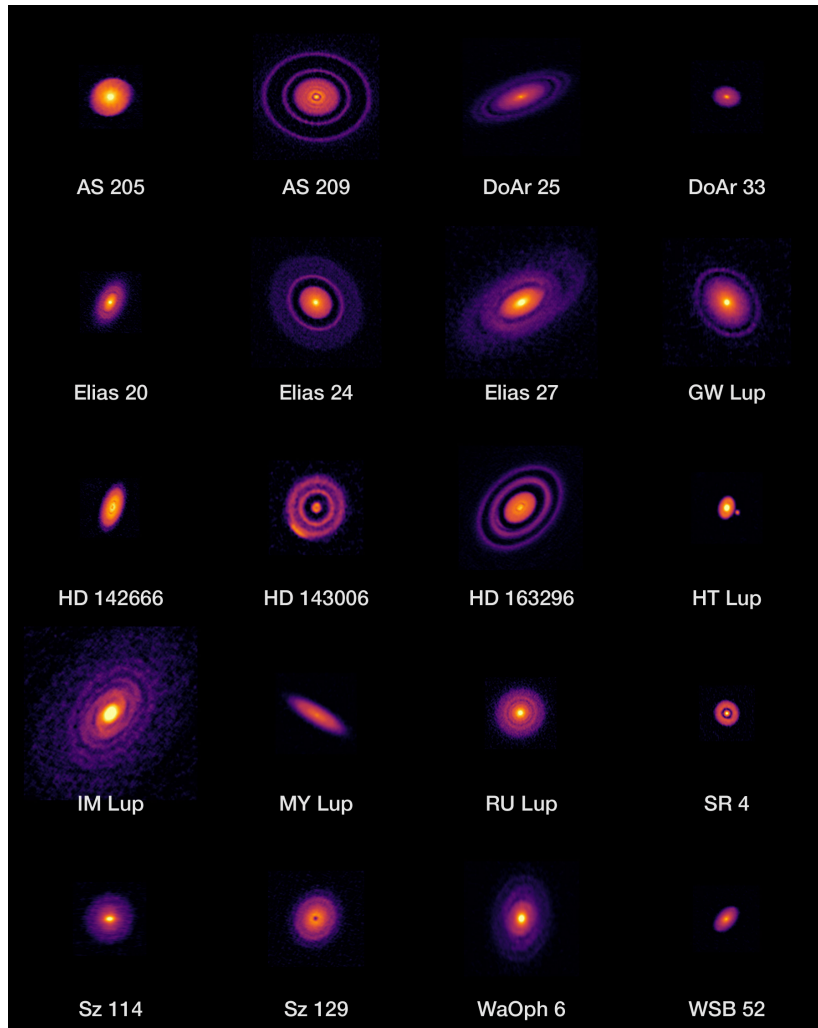
Figure 3.2: Sample of high-resolution images of near-by protoplanetary disks observed by
ALMA. Credit: ALMA (ESO/NAOJ/NRAO), S. Andrews et al.; N. Lira

Chapter 4

Basic Physics

Hydrodynamics, or fluid dynamics in general, is governed by conservation equations for mass, momentum and energy, also known as continuity equations, Navier-Stokes equations and energy equations (e.g. Tey et al. 2017). Further constituents can be added for non-homogeneous fluids e.g the conservation of charge. A detailed derivation for the conservation equations can be seen in Landau & Lifschitz (2019).

4.1 Lagrangian and Eulerian Derivertives

In continuum mechanics the Lagrangian (material) derivative describes the rate of change of a physical field at the place of the fluid element while carried through this field by a flux. Therefore, this derivative includes the change of the strength of the field depending on the spatial location of the particle and a time dependent change of the field at the spatial location of the particle in the field.

- Eulerian time derivative - temporal rate of change of a given physical property of the fluid at a fixed point in a stationary reference system

- Lagrangian time derivative - temporal rate of change of a given physical property of the fluid within a certain fluid element and thus in a moved reference system along the fluid with flow velocity

For any macroscopic tensor field $\phi = \phi(\mathbf{u}, t)$ the Lagrangian derivative is defined as

$$\frac{D\phi}{Dt} = \frac{\partial \phi}{\partial t} + (\mathbf{u} \cdot \nabla) \, \phi \, , \tag{4.1.1}$$

where $\frac{\partial \phi}{\partial t}$ is the local change of the field and describes the explicit time dependency of the field at a fixed location $\mathbf{x}$ while $(\mathbf{u} \cdot \nabla) \, \phi$ denotes the convective change of the field. Furthermore it describes the additional change which occurs due to the movement of the fluid element with the flow velocity $\mathbf{u} = \mathbf{u}(\mathbf{x}, t)$.

4.2 System vs. Control Volume

In fluid dynamics the term "system" is used to describe a continuous and homogeneous mass of fluid, that is conserved within a closed boundary. However,

the boundary may change and move over time. This refers to the *Lagrangian* description.

A mathematically abstract but more convenient description is given by the control volume approach. Its a fixed region in space where mass, momentum and energy cross the boundaries of that region, something like a window through which we can observe the properties of the flow. Performing a balance of mass, momentum and energy gives a possibility to deduct the net change of properties within this region. Commonly a fixed control volume is used but in general it can be moving rotating and also rigid or deformable. The control volume V is bordered by the control surface $S(V)$ or ∂V. This description refers to the *Eularian* description.

4.3 Conservative Axioms in Conservative Form

All governing equations can be written in an differential or integral form. A major advantage of conservative differential equations is, that they can be integrated at once on a control volume. The consevative form shows the net change in flux and the conservation of flux quantities through the control surface

$$\underbrace{\frac{df}{dx} = g(x)}_{\text{diff. form}} \longleftrightarrow \underbrace{f(b) - f(a) = \int_a^b g(x)\, dx}_{\text{int. form}}\,, \qquad (4.3.1)$$

in the one dimensional case. Using common field variables, $f = f(t, x_1, x_2, x_3)$ and $g = g(t, x_1, x_2, x_3)$ are functions of time and the three dimensional space. Hence, partial derivatives $\frac{\partial}{\partial t} = \partial_t$ for temporal and the ∇-operator (Nabla-operator) for spatial derivatives are used. To change differentials to surface flux integrals, the integral theorem of Gauss

$$\int_V (\nabla \cdot \mathbf{F})\, dV = \oint_{S(V)} (\mathbf{F} \cdot \hat{\mathbf{n}})\, dS\,, \qquad (4.3.2)$$

is suitable.

The quantity $\mathbf{F}$ is an arbitrary vector and $\hat{\mathbf{n}}$ again is the unit-normal vector on the surface element dS. The general equation of continuity for any integrated physical quantity Φ (also accounts for sinks and sources s), acting on or in this volume that can contribute to or withdraw something from this quantity.

$$\partial_t \Phi + \nabla \cdot (\Phi \mathbf{u} - D\nabla \Phi) + s(\Phi) = 0 \qquad (4.3.3)$$

$$\partial_t \int_V \Phi\, dV = -\oint_{S(V)} (\Phi \mathbf{u} - D\nabla \Phi)\, \hat{\mathbf{n}}\, dS - \int_V s(\Phi)\, dV \qquad (4.3.4)$$

The left part of Eq. 4.3.4 represents the rate change of the quantity Φ (scalar or vector) in the control volume. The middle part of the equation is a flux term (advection and diffusion) with diffusivity D, showing the amount of Φ moving across through the boundary surface of the volume $S(V)$. The right-hand part

is the so called sink or source term that shows how much of the property Φ is lost or gained inside the boundary $S(V)$. In the case of mass, the equation of continuity states, that the change of the mass inside a given volume only depends on the mass flux over the boundary of the control volume because there are no existing sinks or sources where mass is destroyed or produced. Any system that does not fulfill this requirement (differential operators are "outside" all terms involving dependent variables) is a non-conservative form. An explanation of the advantages of the conservative form is given in the Appendix 10.1.1.

4.4   Conservation of Mass

Assuming a control volume filled with a fluid. Since there are neither sinks nor sources for the mass, the change of mass in time can be simply expressed as

$$\dot{m} = \frac{\partial m}{\partial t} = \partial_t m \,. \tag{4.4.1}$$

The integrated mass is defined as

$$m = \int_V \rho \, dV \,. \tag{4.4.2}$$

As a result of the conservation of mass, the mass contained within the volume can only decrease if a mass flux over the boundary of the volume is established. The escaping fluid describes a flux written as $\rho \mathbf{u}$ in the direction $\hat{\mathbf{n}}$ (outward-pointing unit-normal vector),

$$\int_V \partial_t \rho \, dV = - \oint_{S(V)} \rho \mathbf{u} \cdot \hat{\mathbf{n}} \, dS. \tag{4.4.3}$$

By applying the divergence theorem of Gauss and a short reposition Eq. 4.4.3 can be written as

$$\int_V \left(\partial_t \rho + \nabla \cdot \rho \mathbf{u} \right) \, dV = 0 \,. \tag{4.4.4}$$

This integral yields zero only if

$$\partial_t \rho + \nabla \cdot \rho \mathbf{u} = 0 \tag{4.4.5}$$

is valid. This equation is called **equation of continuity** and shows that the rate change of the mass inside any control volume V is equal to the amount of mass that flows in or out this volume across the boundary surface of this volume. This form is already a conservative form. For an incompressible fluid, where the density $\rho = $ const., the equation simplifies to $\nabla \cdot \mathbf{u} = 0$. This states that for an incompressible fluid the volume is conserved.

4.5   Conservation of Momentum

With similar considerations about a control volume one can derive the equation of motion (Newton's second law). Assuming a control volume and a pressure exerted on a surface element dS on the boundary of the volume. The divergence theorem of Gauss aims

$$\mathbf{F} = - \oint_{S(V)} P\,\hat{\mathbf{n}}\,dS = - \int_{V} \nabla \cdot P\,dV \qquad (4.5.1)$$

The force $\mathbf{F}$ accelerates a mass m within the control volume with $\frac{D\mathbf{u}}{Dt}$ (since the mass element is inside the control volume the material derivative is used). Using Newton's second law $F = m\,a$, the integral can be rewritten as

$$\int_{V} \rho \frac{D\mathbf{u}}{Dt}\,dV = - \int_{V} \nabla \cdot P\,dV \to \int_{V} \left(\rho \frac{D\mathbf{u}}{Dt} + \nabla \cdot P \right) dV = 0\,. \qquad (4.5.2)$$

Thus the **equation of momentum** in non-conservative (convective) form reads as follows

$$\rho \frac{D\mathbf{u}}{Dt} + \nabla \cdot P = \rho\left[\partial_t \mathbf{u} + (\mathbf{u} \cdot \nabla)\mathbf{u}\right] + \nabla P = 0\,. \qquad (4.5.3)$$

These equations state for a force equilibrium and links the temporal change of velocity at a certain location with the ambient pressure gradient. Now we can add several other external forces such as forces due to gravity e.g. the gravitational force density $-\rho\mathbf{g}$. In absence of viscosity the fluid is an ideal fluid without conduction or dissipation. This can be changed by adding the divergence of the viscous shear stress tensor $\nabla \cdot \underline{\tau}$. After some calculations (see Appendix 10.1.2) the Navier-Stokes momentum equation

$$\rho\left[\frac{\partial \mathbf{u}}{\partial t} + (\mathbf{u} \cdot \nabla)\mathbf{u}\right] = -\nabla P + \rho\nu\nabla^2\mathbf{u} + \rho\mathbf{g}\,. \qquad (4.5.4)$$

is attained. The pressure term $-\nabla P$ denotes that the fluid flow points on the direction of the largest pressure gradient. The viscous force term accounts for viscosity controlled velocity diffusion. The gravitational force term contributes for gravity as external force. Further external forces can be e.g. electromagnetic forces or forces due to radiation.

A possibility to derive the conservative form of the equation of motion is by utilizing the mass conservation and reshaping Eq. 4.4.5 to units of momentum. Adding this to Eq. 4.5.4 gives

$$\underbrace{\mathbf{u}\,\partial_t\rho + \mathbf{u}\,\nabla \cdot (\rho\mathbf{u})}_{\mathbf{u}\,\cdot\,\text{Eq.4.5.4}} + \rho\,\partial_t\mathbf{u} + \rho\,(\mathbf{u} \cdot \nabla)\mathbf{u} = -\nabla P + \rho\nu\nabla^2\mathbf{u} + \rho\mathbf{g}\,. \qquad (4.5.5)$$

Using the chain rule for derivative twice, this equation simplifies to the expression

$$\partial_t(\rho\mathbf{u}) + \nabla \cdot (\rho\mathbf{u}\mathbf{u}) = -\nabla P + \rho\nu\nabla^2\mathbf{u} + \rho\mathbf{g}\,. \qquad (4.5.6)$$

Using the Poisson equation for the gravitational potential in radial symmetry,

$$\triangle\psi = \frac{1}{r^2}\frac{d}{dr}\left(r^2\frac{d}{dr}\psi\right) = 4\pi G\rho\,, \tag{4.5.7}$$

the gravitational acceleration can be defined as

$$\nabla\psi = -\mathbf{g} \tag{4.5.8}$$

and Eq. 4.5.6 can be written as

$$\partial_t(\rho\mathbf{u}) + \nabla\cdot(\rho\mathbf{u}\mathbf{u}) + \nabla P + \nabla\cdot\underline{\underline{Q}} + \rho\nabla\psi = 0 \tag{4.5.9}$$

where $\underline{\underline{Q}} = -\underline{\underline{\tau}}$ is viscous pressure tensor.

4.6 Conservation of Energy

The total energy in a closed control volume remains constant, even if energy is transformed from one form to another. In general the equation of energy conservation is suggested by the first law of thermodynamics

$$\Delta U = \delta Q - \delta W\,, \tag{4.6.1}$$

where ΔU is the change in inner energy of a system, δQ is the heat added to the system and ΔW is the work that is applied by this system to its surroundings.

Following (Landau & Lifschitz 2019) (or in short Appendix 10.1.3) the energy equation reads

$$\partial_t(\rho e) + \nabla\cdot(\rho\mathbf{u}e) + P\nabla\cdot\mathbf{u} + \underline{\underline{Q}} : \nabla\mathbf{u} + \nabla\cdot\mathbf{q} - 4\pi\rho\kappa\,(J - S) = 0\,. \tag{4.6.2}$$

Here, $\rho\kappa$ is the absorption coefficient, $\epsilon_q = \underline{\underline{Q}} : \nabla\mathbf{u}$ is the viscous energy dissipation, J is the radiation energy density,and S is the source function.

4.7 Equation of State

To describe the internal structure of gas, an equation of state is necessary. It relates a set of thermodynamic variables, describing the state of matter under the conditions given. In the case of an ideal gas it connects pressure P, volume V and temperature T in the following form

$$PV = n\mathcal{R}T\,, \tag{4.7.1}$$

where n is the number of particles and $\mathcal{R}$ the universal gas constant. Another way to express this equation is by using the density ρ and Boltzmann's constant k

$$P = nkT\,. \tag{4.7.2}$$

This equation can be rewritten by using $n = \rho\bar{m}^{-1}$ (with the average mass per particle $\bar{m} = \mu m_H$ where μ is the unit-less mean molecular weight and hydrogen atom mass m_H)

$$P = \rho\frac{kT}{\bar{m}} \tag{4.7.3}$$

The equation of the speed of sound reads

$$c_s = \sqrt{\Gamma_1 \frac{kT}{\bar{m}}} \qquad (4.7.4)$$

where Γ_1 is the first adiabatic exponent (see Eq. 2.2.1) that links the isochoric c_V and isobaric c_P heat capacity, thus also known as heat capacity ratio.

$$\Gamma_1 = \frac{c_P}{c_V} \rightarrow PV^{\Gamma_1} = \text{const.} \qquad (4.7.5)$$

Applying $\Gamma_1 = 1$ for isothermy on Eq. 4.7.4 and substituting this into Eq. 4.7.3 the **isothermal equation of state** for an ideal gas,

$$P = \rho c_S^2 \qquad (4.7.6)$$

can be obtained. Eq. 4.7.6 is widely used in stellar astrophysics and in this thesis.

Chapter 5

Physics of Circuumstellar Disks

Because of the conservation of angular momentum, the interstellar cloud is not capable to collapse immediately to stellar densities and thus forms an accretion disk as natural consequence of the gravitational collapse. A usable quantity to describe the formation and evolution of a protoplanetary disk is the specific angular momentum

$$l = \mathrm{r} \mathrm{v}_{\phi,\mathrm{gas}} = \mathrm{r}^2 \Omega = \sqrt{\mathrm{GM}_\star \mathrm{r}}\,, \tag{5.0.1}$$

where $M_\star$ is the mass of the central star, Ω is the angular velocity, r is the distance from the Star and G is the gravitational constant. For a geometrically thin disk the angular velocity is equal to that of a Keplarian orbit (Armitage 2010). Additionally, the specific angular momentum is increasing with the radius of the disk.

For the disk to evolve, gas has to be accreted inwards towards the central star and thus has to lose angular momentum. Since angular momentum is a conservative quantity it cannot be lost but redistributed outwards (Pringle 1981).

In this chapter, I closely follow Armitage (2010).

5.1 Conservation of Angular Momentum

The following chapter illustrates, that a cloud collapses if centrifugal forces are negligible in the beginning and that this collapse leads to a protostellar disk, if centrifugal forces become important in the later stages of the collapse. In this content, the collapse is divided into an initial (collapse of an initial stable configuration) and final phase (collapse onto a disk).

5.1.1 Initial State

The equation of motion consists of terms for inertia, flux, pressure (thermal and magnetic), magnetic friction and gravity (from left to right).

$$\rho \frac{\partial \mathbf{v}}{\partial \mathrm{t}} + \rho(\mathbf{v}\nabla)\mathbf{v} = -\nabla\left(\mathrm{P} + \frac{\mathrm{B}^2}{8\pi}\right) + \frac{(\mathbf{B}\nabla)\mathbf{B}}{4\pi} + \rho\nabla\Psi \tag{5.1.1}$$

It is assumed, that magnetic fields are insignificant shortly before the collapse due to ambipolar diffusion ("$\mathbf{B} = 0$", see e.g. Armitage 2010) and so magnetic terms are negligible. Assuming rotational symmetry (spherical symmetry), $\mathbf{v} \approx 0$ for the flux term. Centrifugal forces are non-relevant for the stability of the core of the cloud which simplifies Eq. 5.1.1 to

$$\rho \frac{\partial v}{\partial t} + \frac{\partial P}{\partial r} = \rho \nabla \Psi = -\rho \frac{GM_r}{r^2} \,. \tag{5.1.2}$$

Taking into account the following assumptions and simplifications

- hydrostatic equilibrium

$$\frac{\partial P}{\partial r} = -\rho \frac{GM_r}{r^2} \tag{5.1.3}$$

- the integrated mass

$$M_r = \int_0^r \rho(r')4\pi r'^2 dr' \tag{5.1.4}$$

- the isothermal equation of state.

$$P = \rho c_S^2 \tag{5.1.5}$$

(where c_S is the isothermal speed of sound) the following differential equation can be obtained.

$$c_S^2 \frac{\partial \rho}{\partial r} = -\rho \frac{G}{r^2} \int_0^r \rho(r')4\pi r'^2 dr' \tag{5.1.6}$$

The solution in equilibrium yields

$$\rho(r) = \frac{c_S^2}{2\pi G r^2} \propto \frac{1}{r^2} \,, \tag{5.1.7}$$

a density profile for a state of equilibrium for a non-magnetized, isothermal, spherical cloud. The cloud rotates and contracts. The conservation of angular momentum leads to an increase in rotational speed and thus centrifugal forces are increasing and become more important. At larger distances the gravitational influence is negligible and thus the equation of motion simplifies to

$$\rho \frac{\partial v}{\partial t} + \frac{\partial P}{\partial r} \approx 0 \,. \tag{5.1.8}$$

Thermal pressure and centrifugal force both tend to expand the system. An equilibrium van be established when taking Eq. 5.1.8 into account

$$\frac{\partial P}{\partial r} = -\rho \frac{\partial v}{\partial t} = \rho \frac{v_{rot}^2}{r} \,. \tag{5.1.9}$$

For the rotational velocity $v_{rot} = \Omega r$ a Keplerian orbit is assumed and the cloud (gas sphere) is treated as rigid rotator $\Omega \approx$ const. By applying Eq. 5.1.5 and Eq. 5.1.7, the thermal radius

$$R_{th} = \sqrt{2} \frac{c_S}{\Omega} \,, \tag{5.1.10}$$

is obtained. At this radius thermal pressure and centrifugal force are equal. Values for a stable rotating cloud like T = 10 K, $\bar{m}$ = 2.33 m_p, $\Omega = 10^{-14}s^{-1}$ ($\tau_{rot} = 2 \times 10^7$ yr) lead to c_S = 190 m/s and so $R_{th} \approx 0.9$ pc. This is much larger than typical radii for collapsing clouds and justifies the assumption of negligible centrifugal forces in the initial state of a rotational symmetric, non-magnetized, isothermal cloud. If this would not be the case, the centrifugal forces will prevent the cloud from collapsing onto a star.

> In the initial state of the star formation, gravity overtakes centrifugal forces to enable a collapse in a molecular cloud. Due to ambipolar diffusion, even magnetic fields are unable to prevent the collapse.

In the initial state of a collapse, centrifugal forces are negligible because based on the hydrostatic equilibrium and isothermy a density profile for this state of equilibrium can be calculated. The conservation of angular momentum yields to an increase in the rotational velocity. At a certain radius (thermal radius R_{th}) the centrifugal force and the thermal pressure, both expanding forces, are equal. Under realistic circumstances, $R_{th} \approx 1$ pc, that is larger than the extension of the initial collapsing cloud. Hence, centrifugal forces are initially insignificant and cannot prevent the cloud from the collapse.

5.1.2 Final State

Due to the assumption of ambipolar diffusion and a low degree of ionization, magnetic fields are irrelevant during the collapse. Additionally, the pressure increases not as fast as negligible gravitational forces and only centrifugal forces act against gravity. A mass element forced onto a Keplerian orbit thus complies an equilibrium between centrifugal and gravitational forces $F_C = F_G$

$$\frac{\partial P}{\partial r} = -\rho\frac{\partial v}{\partial t} = -\rho\frac{v_{rot}^2}{r} = -\frac{G\rho M_r}{r^2} \, . \tag{5.1.11}$$

The rotational velocity $v_{rot} = \Omega r$ for a Keplerian orbit leads to the radius R_K and the velocity v_K of a body on such an orbit.

$$R_K = \left(\frac{GM_r}{\Omega^2}\right)^{1/3} \tag{5.1.12}$$

$$v_K = \sqrt{\frac{GM_r}{r}} = \Omega r \tag{5.1.13}$$

$$\Omega = \sqrt{\frac{GM_r}{r^3}} \tag{5.1.14}$$

Analyzing Eq. 5.1.14, that the orbital velocity $v_K(r)$ is a function of the radius r. This leads to velocity gradients and thus to friction within the disk. Hence, viscosity will take a leading part in the further evolution of the protostellar disk.
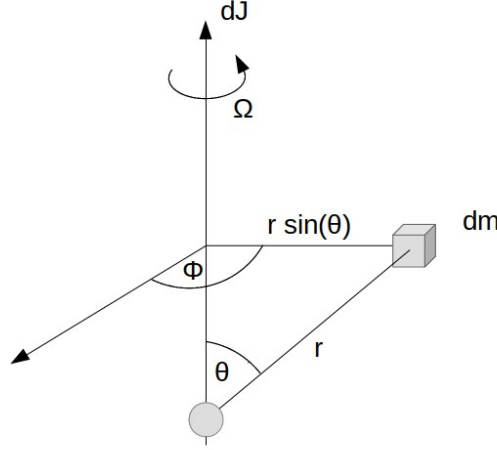
Figure 5.1: Geometry of a mass element dm (yellow cube) orbiting a central star (yellow circle) at a distance r with an orbital velocity $v_{\text{rot}} = \Omega r$. The orthogonal radius $r_\perp = r \sin\theta$ is used to calculate the differential angular momentum dJ

If not discharged, the angular momentum of an infinitely small mass element dm is conserved while the collapse goes on. Following the geometry in Figure 5.1, the differential angular momentum reads

$$dJ = r_\perp v_{\text{rot}} dm = r \, \sin\theta \, v_{\text{rot}} \, \rho d^3 x \,, \tag{5.1.15}$$

where the mass element is rewritten as $dm = \rho dV = \rho d^3 x$ at a distance of $r \sin(\theta)$ of the axis of rotation. In spherical geometry $d^3 x = r^2 \sin\theta \, d\theta d\phi dr$ and $v_{\text{rot}} = \Omega r \sin(\theta)$, Eq. 5.1.15 can be solved by using Eq. 5.1.7.

$$J(r) = \int_0^R dJ = \frac{c_S^2 \Omega}{G} \frac{r^3}{3} \int_0^\pi \sin^3\theta \, d\theta = \frac{c_S^2 \Omega}{G} \frac{4 r^3}{9} \tag{5.1.16}$$

Solving Eq. 5.1.4 by inserting the density profile (see Eq. 5.1.7) leads to

$$M_r = \int_0^r \rho(r') 4\pi r'^2 dr' = \frac{2 c_S^2}{G} r \tag{5.1.17}$$

By substituting Eq. 5.1.17 into Eq. 5.1.16 the angular momentum can be rewritten (the leading $\frac{2}{9}$ defines a structure factor for the sphere)

$$J(r) = \frac{2}{9} M_r r^2 \Omega = \frac{2}{9} M_r r v_{\text{rot}} \,. \tag{5.1.18}$$

The mass element dm travels from its initial position at radius r_i to its final position at radius r_f. Along its path, the angular momentum is conserved

$$v_{\text{rot}}(r_i) r_i = v(r_f) r_f \,. \tag{5.1.19}$$

The quantity $v(r_f)$ defines the tangential velocity of the mass element at its new position, and can be written by using $v_{\text{rot}}(r_i) = \Omega_i r_i \sin\theta$ as

$$v(r_f) = \frac{r_i^2 \sin\theta \Omega_i}{r_f} \,. \tag{5.1.20}$$

The mass element falls freely from r_i until centrifugal $F_C(r_f)$ and gravitational forces $F_G(r_f)$ are equal at the final position r_f (until a Keplerian orbit is reached).

$$F_C(r_f) = F_G(r_f) \rightarrow \sin\theta \frac{v^2(r_f)}{r_f \sin\theta} = \frac{GM(r_f)}{r_f^2} \qquad (5.1.21)$$

Substituting Eq. 5.1.20 into Eq. 5.1.21 the radius r_f of the new position is obtained. For this step it is considered, that during the collapse onto the disk the entire mass falls from r_i to r_f which leads to $M(r_f) = M(r_i)$.

$$r_f = \frac{(r_i^2 \Omega_i)^2 \sin^2\theta}{GM(r_i)} \qquad (5.1.22)$$

At this position the mass element is forced onto a circular orbit (Keplerian orbit) and cannot exceed this radius because beyond r_f the centrifugal force is larger than the inwards pulling gravitational force. If $r_i = R$ is the initial radius of the initial gas sphere (cloud) then radius $r_f = R_C$, is the centrifugal radius $R_C(\theta)$ and is a function of the inclination θ of the direction vector to the axis of rotation

$$R_Z(\theta) = \frac{(R^2 \Omega)^2 \sin^2\theta}{GM} . \qquad (5.1.23)$$
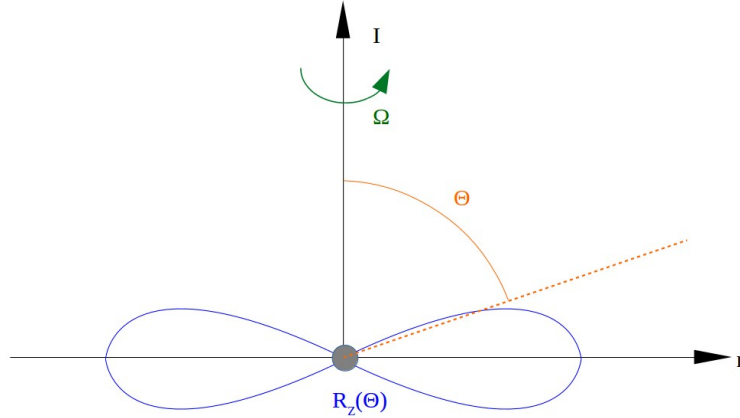
Figure 5.2: The blue contour represents the centrifugal radius for a given orbit and inclination of the infalling mass element. Mass elements, located perpendicular to r have no angular momentum ($\theta = 0$) while mass elements at the equator ($\theta = \pi/2$) have maximal angular momentum. Thus, the formation of a disk is a natural consequence of the contraction of a rotating sphere.

A further contraction can now only happen in z-direction.

In the final state, the collapsing cloud enters a gravitational runaway, so neither magnetic fields nor thermal pressure can act against gravity. Only centrifugal forces operate as counterpart to gravitational forces. In equilibrium ($F_G = F_C$) an initial (in direction of the star) free falling mass element must reach a certain radius (centrifugal radius $R_C(\theta)$ as function of inclination θ in the direction of the axis of rotation) where it is forced onto a Keplerian orbit. The mass element cannot exceed $R_C(\theta)$ because beyond this point $F_Z > F_G$. The dependency of

the angular momentum on θ additionally shows, that an infalling mass element at $\theta = 0$ has no angular momentum, thus falling in free fall onto the star, while an element at $\theta = \pi/2$, has maximal angular momentum and is forced onto the maximal distance. This process ultimately leads to a disk-like structure.

5.2 Conservation of Energy

During the collapse a reallocation of potential and kinetic energy takes place. Initially the potential energy dominates in the form of gravitational energy which is transformed into 50% kinetic energy (orbital energy) and 50% thermal energy (friction). For the sake of simplicity, radiation due to heat conduction is not taken into account. The following equation defines the conservation of energy from an initial state i to a final state f.

$$E_{pot,i} + E_{kin,i} = E_{pot,f} + E_{kin,f} + \Delta E \tag{5.2.1}$$

Since the cloud collapses from i to f, the enclosed mass M_r is conserved.

$$-\frac{GM_r\Delta m}{r_i} + \frac{1}{2}\Delta m(\Omega_i r_i)^2 = -\frac{GM_r\Delta m}{r_f} + \frac{1}{2}\Delta m(\Omega_f r_f)^2 + \Delta E \tag{5.2.2}$$

By using the Keplerian velocity (see Eq. 5.1.13) the virial theorem is obtained.

$$E_{kin} = \frac{1}{2}\Delta m(\Omega r)^2 = \frac{GM_r\Delta m}{2r} = \frac{1}{2}E_{pot} \tag{5.2.3}$$

To permit a collapse $F_C < F_G$ has to be valid.

$$\frac{(\Omega r_i)^2}{r_i} < \frac{GM_r}{r_i^2} \tag{5.2.4}$$

During the collapse the cloud contracts considerably which means that $r_f \ll r_i$. Hence, $E_{kin,i} < |E_{pot,i}| \ll |E_{pot,f}|$ and utilizing Eq. 5.2.1, $E_{kin,i} + E_{pot,i} \approx 0$. Therefore, the right side of 5.2.1 has to cancel out

$$0 \approx -\frac{GM_r\Delta m}{r_f} + \frac{1}{2}\Delta m(\Omega_f r_f) + \Delta E, \tag{5.2.5}$$

$$\frac{GM_r\Delta m}{r_f} \approx \frac{1}{2}\Delta m(\Omega_f r_f) + \Delta E. \tag{5.2.6}$$

This shows that during the collapse half of the potential energy is transformed into kinetic energy and the other half, namely ΔE, corresponds to the energy that is radiated due to friction (viscosity)

$$\Delta E = \frac{1}{2}\frac{GM_r\Delta m}{r}. \tag{5.2.7}$$

5.3 Accretion in Protoplanetary Disks

The accretion disk can be considered as an axis-symmetric, geometrically thin disk and can be divided into annuli with a certain thickness Δr at different radii r. Considering Eq. 5.1.13 different radii rotate at different radial velocities $v_r = r\,\Omega(r,t)$ (assumed to be small) around the star, thus leading to friction between the annuli, since the disk is a viscous fluid. Friction is energy conservation into heat and leads to a change in energy, momentum and accretion (inwards moving of mass). The disk can be described by the density profile $\Sigma(r,t)$

$$\Sigma = \int_{-\infty}^{+\infty} \rho(z)\,dz\,. \tag{5.3.1}$$

Using the thickness Δr, the mass within a differential annulus Δm and the momentum can be defined as follows

$$\Delta m = 2\pi r\,\Delta r \Sigma(r,t)\,, \tag{5.3.2}$$

$$\Delta p = 2\pi r\,\Delta r \Sigma(r,t)\,r^2 \Omega(r,t)\,. \tag{5.3.3}$$

5.3.1 Change of Mass

Due to the conservation of mass, the gas content in one annulus only changes by an in- or out-flow of gas over the boundaries with the radial velocity v_r (per definition $v_r < 0$). The change of mass δm is defined positive if mass leaves the annulus and defined negative if mass is added to the mass content in the annulus (Armitage 2010). Mass enters the annulus over the outer boundary $r + \Delta r$ and leaves it in δt over the inner boundary r in the direction of the star. In this way mass travels in from one ring to the other and will finally fall onto the star. Using Eq. 5.3.2 and substituting $\Delta r \rightarrow v_r(r,t)\delta t$, the evolution of $\Sigma(r,t)$ can be written as (e.g. Pringle 1981).

$$\frac{\delta}{\delta t}\left(2\pi r\,\Delta r \Sigma(r,t)\right) = 2\pi r\,\Sigma(r,t)v_r(r,t) - 2\pi(r+\Delta r)\,\Sigma(r+\Delta r,t)v_r(r+\Delta r,t)\,. \tag{5.3.4}$$

Applying further simplifications (e.g. see Appendix 10.1.5), leads to the **Equation of Continuity**

$$r\frac{\partial \Sigma}{\partial t} + \frac{\partial}{\partial r}(\Sigma\,v_r r) = 0\,, \tag{5.3.5}$$

where r is the radius of the annulus, Σ is the surface density and v_r is the radial velocity.

5.3.2 Change of Angular Momentum

The change of angular momentum depends on the flow of mass through an annulus. Additionally, a momentum of inertia acts between the differential rotating annuli due to friction (e.g. Pringle 1981). Using Eq. 5.3.3 and by substituting

$\Delta r \to v_r(r, t)\delta t$, the change of angular momentum reads

$$
\begin{aligned}
\frac{\delta}{\delta t}(2\pi r \, \Delta r \Sigma(r, t) \, r^2\Omega(r, t)) &= 2\pi r \, v_r(r, t)\Sigma(r, t) \, r^2\Omega(r, t) \\
-2\pi(r + \Delta r) \, v_r(r + \Delta r, t)\Sigma(r + \Delta r, t) & \, (r + \Delta r)^2\Omega(r + \Delta r, t) \\
&-G(r) + G(r + \Delta r) \,.
\end{aligned}
\tag{5.3.6}
$$

The first two lines in Eq. 5.3.6 resemble for the radial angular momentum, while the third line stands for the torque exerted from one ring to the adjacent ring due to viscous friction. Applying further simplifications (see Appendix 10.1.5) lead to the **Equation of Motion**

$$
r\frac{\partial}{\partial t}(\Sigma r^2\Omega) + \frac{\partial}{\partial r}(\Sigma r^2\Omega \, v_r r) = \frac{1}{2\pi}\frac{\partial G}{\partial r} \,,
\tag{5.3.7}
$$

where r is the radius of the annulus, Σ is the surface density, v_r is the radial velocity, Ω is the Keplerian angular velocity and G is the torque.

5.3.3 Viscous Accretion

The friction that is responsible for the torque G is assumed to be caused by viscosity. A liquid that is moving with differential velocity can be divided into multiple shearing layers with surfaces A at distances Δx. The difference in velocity and distance leads to a velocity gradient $\Delta v/\Delta x$. The force of friction F acts at A, perpendicular to the x-axis and against the velocity Δv. This leads to Newton's law of friction

$$
F = \mu_Q A \frac{\Delta v}{\Delta x} \,.
\tag{5.3.8}
$$

The viscosity constant is a material property that acts as proportionality constant μ_Q and is called dynamic viscosity

$$
\mu_Q = \nu\rho \,,
\tag{5.3.9}
$$

where ν is the kinematic viscosity and ρ the mass density. In an accretion disk $v = v_{rot}$ and utilizing $A = 2\pi r \int dh$ and $\frac{\Delta v}{\Delta r} = r\frac{d\Omega}{dr}$ ("shearing") and Eq. 5.3.1 the force of friction can be written as

$$
F = 2\pi r \, \nu \underbrace{\int dh \, \rho}_{\Sigma} \, r\frac{d\Omega}{dr} \,.
\tag{5.3.10}
$$

As a consequence the torque becomes

$$
G = F \, r = 2\pi r \, \Sigma\nu \, r\frac{d\Omega}{dr} r \,.
\tag{5.3.11}
$$

For Keplerian orbits (by substituting Eq. 5.1.14 in Ω) this leads to

$$
\frac{\partial G}{\partial r} = -\frac{\pi}{3}\frac{\partial}{\partial r}\left(\nu\Sigma\sqrt{GM_\star r}\right) \,.
\tag{5.3.12}
$$

The substitution (Eq. 5.3.12 into Eq. 5.3.7) leads to a **diffusive partial differential equation** for $\Sigma(r,t)$

$$\frac{\partial \Sigma}{\partial t} = \frac{3}{r}\frac{\partial}{\partial r}\left[\sqrt{r}\frac{\partial}{\partial r}\left(\nu\Sigma\sqrt{r}\right)\right].$$ (5.3.13)

This can be interpreted as an evolution equation of the surface density in an axis-symmetric, thin disk with internal angular momentum transport. The diffusive character of this equation can easily be seen by applying a variable substitution and assumption of constant viscosity ν Armitage (2010). By defining

$$X = 2\sqrt{r},$$
$$f = \frac{3}{2}\Sigma X,$$ (5.3.14)

Eq. 5.3.13 takes the form of a typical diffusion equation

$$\frac{\partial f}{\partial t} = D\frac{\partial^2 f}{\partial X^2},$$ (5.3.15)

where D is the diffusion coefficient given by

$$D = \frac{12\nu}{X^2}.$$ (5.3.16)

Although, a constant viscosity is not necessarily realistic for a protoplanetary disk, a Green's function solution and the qualitative illustration of the behavior of Eq. 5.3.13 is possible. Initial conditions at $t = 0$ for this problem are given in (Armitage 2010) where all matter is embedded in a tenuous ring of mass m at radius r_0

$$\Sigma(r,t=0) = \frac{m}{2\pi r_0}\delta(r-r_0),$$ (5.3.17)

where $\delta(r-r_0)$ is the Dirac delta function. Boundary conditions that enforce zero-torque at $r = 0$ and free expansion at $r \to \infty$ yield (Lynden-Bell & Pringle 1974)

$$\Sigma(x,\tau) = \frac{m}{\pi r_0^2}\frac{1}{\tau}x^{-\frac{1}{4}}\exp\left[-\frac{(1+x^2)}{\tau}\right]I_{1/4}\left(\frac{2x}{\tau}\right),$$ (5.3.18)

for the time-dependent solution for Eq. 5.3.13. The variables x and τ represent unitless variables

$$x = \frac{r}{r_0},$$
$$\tau = 12\nu r_0^{-2}t,$$

and $I_{1/4}$ the modified Bessel function of the first kind .

The Equation Eq. 5.3.13 leads to the following conditions:

- An initial annulus of mass broadens in time.

- The major part of mass flows in direction of the star $\to$ accretion. Angular momentum is transported outwards along with a small amount of mass, since angular momentum is coupled with mass.

- For t → ∞ all mass moves to r → 0 and all angular momentum shifts to r → ∞

Figure 5.3 shows the numerical and analytical (e.g Pringle 1981) solution for the diffusion equation Eq. 5.3.13. The numerical solution was calculated by the TAPIR code for protoplanetary disks (see e.g. Stoekl & Dorfi 2014).
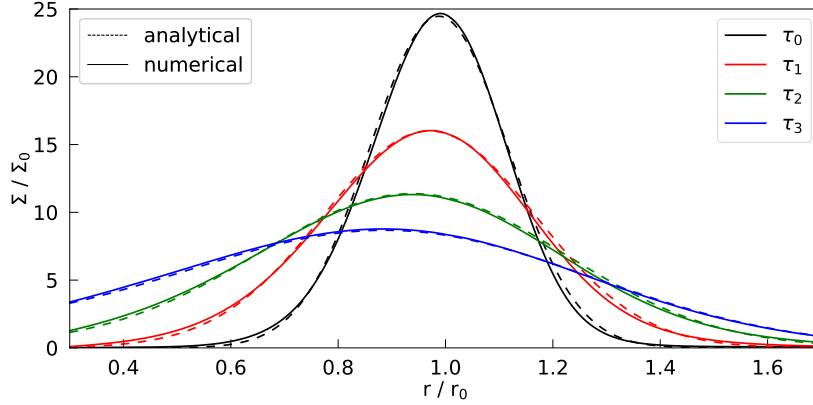
Figure 5.3: This figure shows the difference between the analytical (e.g Pringle 1981) and the numerical solution of the diffusion equation Eq. 5.3.13 for four different time-steps τ_0 to τ_3. The horizontal axis shows the radius, normalized to the initial radius of the ring of mass and the vertical axis shows the normalized surface density. The numerical solution was calculated with the TAPIR code. It shows how an arbitrary annulus of mass spreads, beginning at an distance $r = r_0$ from the star. The viscosity ν is constant in this example. Each line represents the disk advanced in time. The ring spreads in both directions but primary to the left. This represents that some of the mass travels away from the star (since angular momentum is coupled to mass) but the net flow of mass is accreted inwards.

5.4   Viscosity in Protoplanetary Disks

A possibility to quantify the efficiency of viscous transport of material is the viscous timescale (derivation see Eq. 5.5.21). Assuming only molecular viscosity, and using characteristic values for protostellar disks (see e.g. Armitage 2010, p. 79), the viscous timescale yields

$$t_\nu \approx \frac{r^2}{\nu} \approx 3 \times 10^{13} \text{yr} \,. \tag{5.4.1}$$

This is about 6-7 orders of magnitude higher than the estimated lifetime of the protoplanetary disk which is of the order of 10^6 yr (e.g. Armitage 2011). This emphasizes that if viscosity is important for the evolution of the disk, another source of viscosity has to exist. A common accepted solution for this problem is turbulent viscosity (Shakura & Sunyaev 1973).

Usually a variety of instabilities (e.g. gravitational, magentorotational, hydrodynamical or convective instabilities) can occur in an accretion disk. Such instabilities cause turbulences that allow an outwards transportation of angular momentum. The effect of turbulence on angular momentum transport can be

characterized by the turbulent viscosity, which can be parameterized in the α-disk prescription (Shakura & Sunyaev 1973). Turbulence plays two significant roles in protoplanetary disks

1. Turbulence can be responsible for the redistribution of angular momentum towards the outer edge of the disk due to the exertion of torques on the disk. This enables accretion towards the central object.

2. Turbulence provide the conversation of gravitational energy into thermal energy as the mass falls onto the star. This energy dissipation contributes to the total luminosity and is observable.

The main processes that drive the transport or redistribution of mass and angular momentum within the disk are

- viscous torques due to turbulences, triggered by magneto-rotational instability (MRI) (Balbus & Hawley 1991) in the inner regions of the disk and

- gravitational torques due to gravitational instabilities in massive disks, described e.g. by Lin & Pringle (1987).

A brief overview of these processes will be given in the following sections.

5.4.1 Shakura-Sunyaev Viscosity Description

In absence of a complete turbulence theory, turbulence is simulated by the kinematic viscosity ν (Canuto et al. 1984). At first one can assume that ν is related to the standard molecular viscosity. Hence, it is the consequence of thermal collisions between individual fluid elements in the protoplanetary disk. In this case

$$\nu \approx \sqrt{\frac{k_B T}{\bar{m}}} \lambda = v_T \lambda \,, \tag{5.4.2}$$

describes the viscosity as function of a typical thermal velocity v_T and the mean-free path λ of an arbitrary molecule.

The standard Reynolds number for molecular viscosity reads as

$$Re = \frac{\Lambda \upsilon}{\nu} \,, \tag{5.4.3}$$

where Λ is the characteristic length and υ a characteristic velocity of the fluid. If Re is sufficiently high, hydrodynamic turbulence sets in. The random eddies (swirling of a fluid) of this turbulence would cause viscosity, just as random thermal motions cause viscosity on molecular scales. From dimensional arguments, the turbulent viscosity can be written as

$$\nu \sim \Lambda_t \upsilon_t \,, \tag{5.4.4}$$

where Λ_t is the size of the largest eddy and υ_t is the characteristic turbulent velocity. Assuming a thin disk, the largest eddy cannot exceed the pressure scale height $\lambda \leq H$ (H represents the thickness of the disk). Furthermore, it is unlikely

that the turbulences will be supersonic because otherwise shocks would form and the kinetic energy of the turbulent motions would tend to be thermalized. As a result, the characteristic velocity will stay below the local speed of sound $v_t \leq c_S$. In their prescription Shakura & Sunyaev (1973) used the dimensionless value $0 \leq \alpha \leq 1$ to scale these upper limits in the equation for the turbulent, kinematic viscosity

$$\nu = \alpha c_S H \, . \tag{5.4.5}$$

Usually the value of α is much lower than unity (Hartmann & Bae 2018).

5.4.2   Magneto-rotational Instability (MRI)

Pringle (1981) stated, that the ordinary molecular viscosity is to inefficient to explain the angular momentum transfer within the protoplanetary disk. Assuming a magnetized and perfectly conductive fluid, magnetic forces connect fluid elements (Chandrasekhar 1960). This can be interpreted as elastic band or spring, that tend to cause an attractive force proportional to a force exerted onto the element to displace it. Although this seems to stabilize a stationary system, it can cause a destabilization in differential rotating systems. This destabilization mechanism is known as the magneto-rotational instability (MRI) and work only if the ionization fraction is high enough so that the magnetic field can couple with the gas. On the other hand, the field has to be weak enough so that in such a way magnetic tension is not dominant (Armitage 2015). The mechanism behind MRI is illustrated in Figure 5.4. The importance of this behavior for the theory of accretion disk and in particular for the generation of a turbulent viscosity was firstly described by Balbus & Hawley (1991): Assuming a protostellar disk and an vertical magnetic field that penetrates it. The disk is assumed to rotate deferentially at constant Keplerian angular velocity $\Omega(r)$. The magnetic field lines tend to establish rigid rotation between outwards (in radial direction) displaced fluid elements, elastically connected by the magnetic field. This happens due to resisting sharing forces. The field now tries to force the element farther away from the star to rotate at higher velocity than predetermined by its current orbit (and vice versa for the element closer to the star). Hence, the centrifugal forces, increase proportional to the velocity, drive the outer fluid element further away, while the inner element is drawn towards the star. This leads to an interchange in both mass and angular momentum. However, regions, near the disk mid-plane, are shielded from external radiation, remain neutral and are not magnetized. These parts of the disk are of low viscosity and are referred to as dead zone (Gammie 1996).
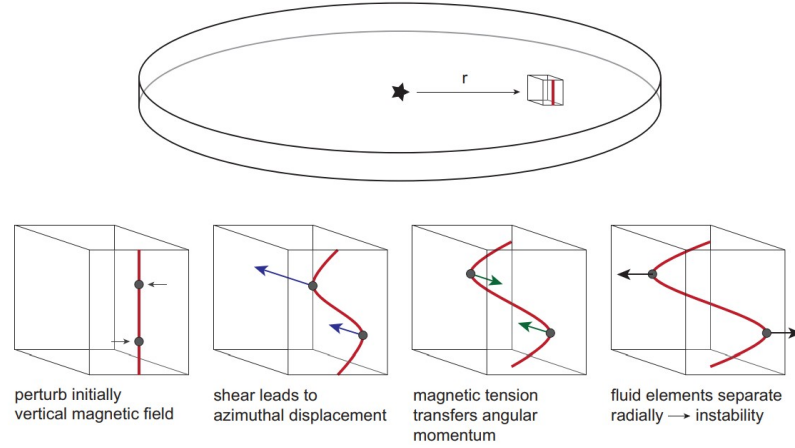
perturb initially
vertical magnetic field

shear leads to
azimuthal displacement

magnetic tension
transfers angular
momentum

fluid elements separate
radially ⟶ instability

Figure 5.4: This figure shows the development of a magentorotational instability within an Keplarian disk. Initially a uniform vertical magnetic fields penetrates the disk and connects two fluid elements. The field has to weak enough that magnetic tension is not dominant. Due to viscous shearing (and differential rotation) in the disk, the inner fluid element advances (azimuthally) faster than the outer element. Due to magnetic tension along the field line, angular momentum is transferred from the inner to the outer fluid element, causing further radial displacement that eventually leads to an radial displacement of the elements and finally to an instability (e.g Armitage 2015).

MRI and non-linear MHD

Following Latter & Balbus (2012), the protoplanetary disk (PPD) can be divided in three regions with respect to MRI. Gas in the mid-plane is thermally ionized by stellar radiation to sufficient levels for MRI to operate but only very close to the star (< 0.1 AU). From about 0.1 to 1.0 AU, where stellar radiation fails to ionize the gas, turbulent heating succeeds in providing temperatures needed for MRI (Gammie 1996; Riols & Lesur 2018). However, this requires initially high temperatures in this region but if it starts cold (poorly ionized) it will remain inactive (Latter & Balbus 2012). Beyond 1 AU non-thermal sources are necessary for ionization e.g. external radiation. It is assumed that this is the inner edge of the dead zone but as described by Latter & Balbus (2012) the dead zone can also extend into the "bi-stable" region between 0.1 and 1.0 AU. Moreover, it is assumed, that at radii beyond 1 AU, non-linear MHD effects like ambipolar diffusion and Ohmic dissipation tend to quench the effect of MRI (e.g. Lesur et al. 2014). However, in this thesis no non-linear MHD effects are included.

5.4.3 MRI and the Layered Disk Model

The protoplanetary disk can be divided into several vertical layers due to the temperature, viscosity and MRI-activity (e.g. Armitage 2011).

A simple schematic structure of a layered disk is presented in Figure 5.5. Because of the low ionization fraction, the angular momentum transport due to MRI is quenched at radii larger than approximately 1 AU for solar like stars. At these distances, dead-zone (regions of low viscosity) can form within the protoplanetary disk. The surface layer of the disk is always partially ionized, either by stellar

radiation (e.g. X-rays, produced from the generated flares as as consequence of releasing magnetic energy by reconnection) or external radiation (e.g. cosmic rays). However, these sources of ionization fail to penetrate to the mid-plane, so other mechanisms, for example collisional ionization or thermal instabilities (see Section 3.1.2), are required to increase the transport of matter in these regions.
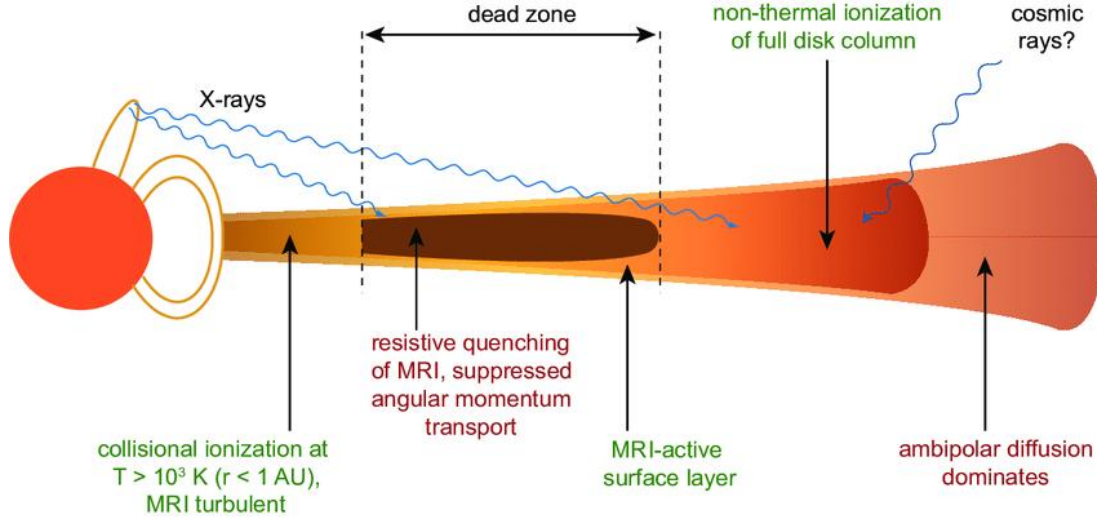
Figure 5.5: Schematic vertical profile of a layered disk including a dead-zone. The surface layer is always MRI-active due to stellar or external radiation, while the deep layer close to the star only becomes MRI-turbulent if it is partially ionized (Armitage 2011).

An example for the numerical implementation of the layered disk model is described in Section 8.2.

5.5 Stationary Disk Discussion

For a better understanding of the evolution of the accretion disk one can imagine the life of the disk as series of snapshots. Looking at one arbitrary snapshot, all physical quantities remain constant in time. Such a disk model is called steady-state disk and implies undermost that $\dot{M}$ = const. The solution of the hydrodynamic equations in the steady state leads to the equilibrium structure of gas, that is orbiting a star in a disk.

5.5.1 Structure

This section describes the structure of a stationary disk in radial and vertical direction.

Radial Structure

In the steady-state, the equation of continuity can be written as

$$\frac{\partial}{\partial r}(\Sigma v_r r) = 0 \rightarrow 2\pi \Sigma v_r r = \dot{M} = \text{const.} \tag{5.5.1}$$

The radial part of the equation of momentum delivers the orbital velocity of the disk gas. Using Eq. 5.1.1 for an unmagnetized and inviscid fluid, the equation of momentum for a stationary, axis-symmetric flow within a gaseous protoplanetary disk, where the potential is dominated by the star, can be written as (Armitage 2010)

$$\frac{v_{\text{rot}}^2}{r} = \frac{GM_\star}{r^2} + \frac{1}{\rho}\frac{\partial P}{\partial r} \,. \tag{5.5.2}$$

Substituting the Keplerian velocity (Eq. 5.1.13) the equation reads

$$\frac{v_{\text{rot}}^2}{r} = \frac{v_{\text{K}}^2}{r} + \frac{1}{\rho}\frac{\partial P}{\partial r} \,. \tag{5.5.3}$$

In general, the pressure close to the mid-plane decreases with increasing radius, leading to a negative pressure gradient. Hence, the rotational velocity of the gas is slightly less than the Keplarian velocity of a point mass at the same orbit. Writing the pressure as a power-law

$$P = P_0 \left(\frac{r}{r_0}\right)^{-n} , \tag{5.5.4}$$

at reference radius r_0 with pressure $P_0 = \rho_0 c_S^2$ yields

$$v_{\text{rot}} = v_{\text{K}} \left(1 - n\frac{c_S^2}{v_{\text{K}}^2}\right)^{1/2} , \tag{5.5.5}$$

where

$$\mathcal{M} = \frac{v_k}{c_S} = \frac{r}{H}$$

is the Mach number, c_S the speed of sound and H the pressure scale height. Concluding, the deviation of the rotation velocity of the gas from the Keplerian velocity is of order $\mathcal{O}(H/r)^2$. When considering geometrical thin disks, where $H \ll r$ and the motion of gas alone, the difference is altogether negligible and $v_{\text{rot}} \approx v_{\text{K}}$. However, the slightly lower gas velocity results in an aerodynamic drag and in a decreasing orbital distance of an arbitrary mass element. This is important for the evolution of solid bodies within the disk (Armitage 2010).

Vertical Structure

The structure of a stationary disk results from radial and angular momentum conservation and the assumption that the vertical component of gravity from the star is balanced by the vertical gas pressure gradient $\rightarrow$ vertical hydrostatic equilibrium (e.g. Dominik 2015). For the vertical hydrostatic structure two simplifications are necessary (e.g. Armitage 2010):

- Only stellar gravity contributes to the overall potential of the system $M_{\text{disk}} \ll M_\star$, the potential of disk is neglected.

- The vertical scale height is small compared to the radius of the disk, aiming a geometrically thin disk $H \ll r$.
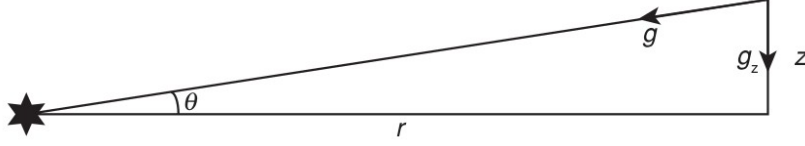
Figure 5.6: Simplified vertical structure of a geometrical thin disk, developed by an equilibrium between the vertical component of the stellar gravitation acceleration g_z and the vertical pressure gradient $\frac{\partial P}{\partial z}$ (Armitage 2010)

.

In a disk around a star with mass $M_\star$, a force balance between the vertical component of the gravitational potential and vertical pressure gradient at any radius r is considered at an arbitrary height z above the mid-plane of the disk

$$\frac{\partial P}{\partial z} = g_z \rho = g \sin(\theta)\, \rho \,, \tag{5.5.6}$$

Applying the geometry given in Figure 5.6, leads to an equation for the vertical component of the gravitational, potential and reads

$$g_z = g \sin(\theta) = -\frac{GM}{r^2 + z^2} \frac{z}{\sqrt{r^2 + z^2}} \,. \tag{5.5.7}$$

Assuming a thin disk ($z \ll r$), Eq. 5.5.7 can be simplified to

$$\frac{1}{\rho} \frac{\partial P}{\partial z} = -\frac{GM\,z}{(r^2 + z^2)^{3/2}} \approx -\frac{GMz}{r^3} \,. \tag{5.5.8}$$

With the equation of state $P = \rho c_S^2$, the Keplarian angular velocity Ω and the vertical scale height $H = c_S/\Omega = rc_S/v_{\mathrm{rot}} = r/\mathcal{M}$, Eq. 5.5.8 can be rewritten and reads

$$\frac{d\rho}{\rho} = \frac{1}{c_S^2} \frac{GM}{r^3} z\, dz = \frac{\Omega^2}{c_S^2} z\, dz = \frac{1}{H^2} z\, dz \,. \tag{5.5.9}$$

Integration of Eq. 5.5.9 over z, results in the vertical density profile of the disk

$$\rho(z) = \rho_0 e^{-\frac{z^2}{2H^2}} \,. \tag{5.5.10}$$

This equation is comparable with the barometric formula. Implementing Eq. 5.5.10 into Eq. 5.3.1 results in

$$\Sigma(r) = \int_{-\infty}^{+\infty} \rho_0 e^{-\frac{z^2}{2H^2}}\, dz = \sqrt{2\pi}\rho_0 H \,, \tag{5.5.11}$$

where the mid-plane density ρ_0 can be derived (see. Appendix 10.1.4) as

$$\rho_0 = \frac{\Sigma}{H\sqrt{2\pi}} \,. \tag{5.5.12}$$

5.5.2 Accretion

For a physical explanation of accretion (the process of mass transport towards the star), we start with the equation of momentum Eq. 5.3.7, neglecting the time dependent derivative due to stationarity

$$\frac{\partial}{\partial r}(\Sigma r^2 \Omega \, v_r r) = \frac{1}{2\pi}\frac{\partial G}{\partial r} \, . \tag{5.5.13}$$

Substituting Eq. 5.3.11 into Eq. 5.5.13 and integration leads to the expression,

$$\Sigma r^3 \Omega \, v_r = r^3 \nu \Sigma \frac{\partial \Omega}{\partial r} - \frac{C}{2\pi} \tag{5.5.14}$$

where C is an integration constant.

To obtain C, it is assumed that the magnetic fields of the star couple with the innermost parts of the disk. Due to this connection and the transport of angular momentum, the star and the inner parts of the disk start to co-rotate. This is the transition between the disk and the magnetosphere of the star, and the radius at this location is called co-rotation radius r_{co} so that $r \geq r_{co}$ leads to $\frac{\partial \Omega}{\partial r} = 0$ because below r_{co} every annulus of the disk rotates with the same angular velocity as the star. This assumption defines C, which can be interpreted as like a flux of angular momentum.

$$C = -2\pi r \Sigma v_r \, r \, r\Omega \bigg|_{r=r_{co}} = \dot{M} r \, v_{rot} \bigg|_{r=r_{co}} = \dot{M}\sqrt{GMr_{co}} \tag{5.5.15}$$

In Eq. 5.5.15 one can use a simple definition for the mass accretion rate $\dot{M}$ e.g. by the equation of continuity in cylindrical symmetry (integrating over the height of the disk) as written in Eq. 5.3.5.

In the steady-stat disk all temporal derivatives vanish leading to $r\Sigma v_r = $ const. Thus, multiplying $r\Sigma v_r$ by 2π results in a constant mass accretion rate $\dot{M}$ in a steady-state disk. The negative sign states negative sign states for the inwards orientated accretion flow, $v_r < 0$. Therefore, we can define the accretion rate

$$\dot{M} = -2\pi r \Sigma v_r \, . \tag{5.5.16}$$

According to e.g Armitage (2010) the integration constant C is often defined as the flux of angular momentum that is accreted onto the star together with the mass. For $r > r_{co}$ the rotation is still Keplarian. Substituting Eq. 5.1.14 and Eq. 5.5.15 into Eq. 5.5.14 the mass flux $\dot{M}$ and thus by using Eq. 5.5.16, the radial velocity component v_r can be written as

$$\dot{M} = 3\pi \nu \Sigma \frac{1}{1 - \sqrt{\frac{r_{co}}{r}}} = -2\pi r \Sigma v_r \, , \tag{5.5.17}$$

$$v_r = -\frac{3\nu}{2r\left(1 - \sqrt{\frac{r_{co}}{r}}\right)} \, . \tag{5.5.18}$$

Since the co-rotation radius r_{co} is very close to the star, the assumption that $r_{co} \ll r$ simplifies Eq. 5.5.17 and Eq. 5.5.18

$$v_r \approx -\frac{3\nu}{2r} \, , \tag{5.5.19}$$

$$\nu\Sigma \approx \frac{\dot{M}}{3\pi} = \text{const.} \, , \tag{5.5.20}$$

which means that, the accretion rate in a steady-state disk is equal in every annulus.

In a viscous accretion disk, the viscosity ν adjusts itself to induce the required mass flux $\dot{M}$ at a given surface density Σ and vice versa.

For example, high viscosity in an arbitrary ring causes more friction which leads to a deceleration of the encapsulated mass and thus a higher accretion rate onto the star. Typical time scales can be derived by using Eq. 5.5.18.

$$t_\nu \approx \frac{r}{v_r} \approx \frac{r^2}{\nu} \tag{5.5.21}$$

The higher the viscosity of the fluid, the smaller t_ν becomes and thus the viscous transport is more efficient.

Chapter 6

Complete Set of Physical Equations

The conservation equations and the equation of state, described in Chapter 4, define a complete system of non-linear, time-dependent equations, which can be solved numerically. Within the scope of this thesis, self gravity of the protostellar disk is neglected. More details on the physical content of the equations can be found in the appendix.

Equation of Continuity

The equation of continuity describes the conservation of mass.

$$\partial_t \rho + \nabla \cdot \rho \mathbf{u} = 0$$

In this equation ρ is the density and $\mathbf{u}$ is the velocity.

Equation of Motion

The equation of motion describes the conservation of momentum.

$$\partial_t (\rho \mathbf{u}) + \nabla \cdot (\rho \mathbf{u}\mathbf{u}) + \nabla P + \nabla \cdot \underline{\underline{Q}} + \rho \nabla \psi = 0$$

In this equation ρ is the density, $\mathbf{u}$ is the velocity, P is the pressure, $\underline{\underline{Q}}$ is the viscous pressure tensor and ψ is the gravitational potential.

Equation of Energy

The equation of energy describes the conservation of energy.

$$\partial_t (\rho e) + \nabla \cdot (\rho \mathbf{u} e) + P \nabla \cdot \mathbf{u} + \underline{\underline{Q}} : \nabla \mathbf{u} + \nabla \cdot \mathbf{q} - 4\pi \rho \kappa \left(J - S \right) = 0$$

In this equation ρ is the density, $\mathbf{u}$ is the velocity, e is the specific energy, $\underline{\underline{Q}}$ is the viscous pressure tensor, $\mathbf{q}$ is heat flux due to diffusion, J is the zeroth moment of the radiation field and S is the source function.

Equation of State

The isothermal equation of state describes the internal structure of gas.

$$P = \rho c_S^2$$

In this equation P is the pressure, ρ is the density and c_S is the sound speed. The equation of state is used to calculate all quantities in z-direction.

Chapter 7

Numerical Methods

Complex systems of partial-differential equations can be solved by using numerical methods. The differential equations of hydrodynamics describe fluid flows in space and time. The numerical integration of these equations requires the discretization of space and time and also an adequate discretization of all equations. A discretization method utilizes a grid to divide the simulated domain into discrete and finite grid-cells. The integration can be done either by using an implicit or explicit numerical integration schemes. In the first section the numerical methods for solving physical equations are presented. The second section shows how physical equations are discretized so that they can be solved by utilizing the discussed numerical methods.

7.1 Explicit and Implicit Integration Schemes

The system of non-linear, time-dependent differential equations in a simulation can be solved either by utilizing explicit or an implicit integration schemes. The main difference between these two methods is how the solution at the new time-step is obtained. In the explicit case only values at the previous time-steps are used, while in the implicit case, also values at the new time-steps are applied to calculate the new values.
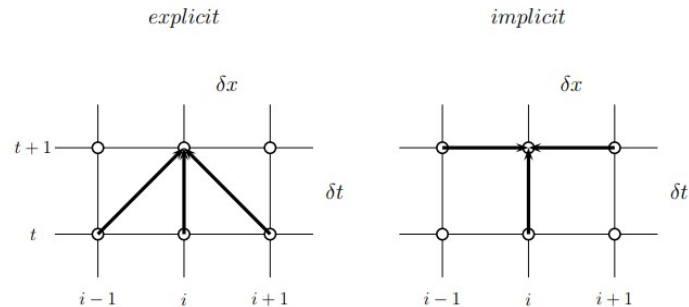
Figure 7.1: The variable i denotes for the grid point t for the current time and δt for the time-step. The picture shows, that the explicit method (left) uses values at three different spacial grid-pints ($i-1$, i and $i+1$) from the old time t to calculate the value at the $i-$th point for the new time $t+1$. In the opposite the implicit method (right) uses old and new values to calculate the solution for the new time. Credits: Florian Ragossnig

Assuming that $\mathbf{x}_i$ is the solution vector at the $i-$th grid point, then the discretization for a set of equation reads

$$\begin{aligned}
\mathbf{x}_i &= (x_{1,i}, x_{2,i}, x_{3,i}, ..., x_{M,i}) \,, \\
\mathbf{x} &= (\mathbf{x}_1, \mathbf{x}_2, \mathbf{x}_3, ..., \mathbf{x}_N) \,,
\end{aligned} \tag{7.1.1}$$

where $i \in [1, N]$ is the number of grid points and M is the number of variables/equations (density, energy, velocity, ...) defined for each grid point.

7.1.1 Explicit Method

For explicit methods assume the following differential equation where $F(\mathbf{x}_i)$ is an arbitrary function only of the old solution vector

$$\frac{d\mathbf{x}}{dt} = F(\mathbf{x}) \,. \tag{7.1.2}$$

To define the temporal change for the solution vector $\mathbf{x}$ in the explicit way, the differential equation can be rewritten in discretized form as

$$\left(\frac{d\mathbf{x}}{dt}\right)^{old} \approx \frac{\mathbf{x}^{new} - \mathbf{x}^{old}}{\delta t} = F(\mathbf{x}^{old}) \,. \tag{7.1.3}$$

Rewriting this equation, the solution vector for the new time-step $\mathbf{x}^{new}$ yields

$$\mathbf{x}^{new} = \mathbf{x}^{old} + \delta t\, F(\mathbf{x}^{old}) \,. \tag{7.1.4}$$

It can be seen, that the new solution is an extrapolation of the old one, what makes this method highly dependable from the size of the time-step δt, that is limited by the Currant-Friedrichs-Levy (CFL) condition (e.g. LeVeque 2002, p. 52),

$$\delta t \leq \frac{\delta x}{|u| + c_S} \,, \tag{7.1.5}$$

where c_S is the local speed of sound and δx the length interval between the grid points, here in one dimension (note, that the minimal value of the right part of Eq. 7.1.5 for all grid points is decisive). This condition is a necessary, but not necessarily sufficient stability criteria while solving the partial differential equations in this science case. A heuristic description can be done by an example e.g. a shock that is advected through a grid. The time step is neither allowed to be as large as the time for the shock needed to be transported to the adjacent grid point nor to exceed the maximal time for the transport of information defined by c_S. Otherwise, the numerical solution will diverge highly from the true one. As stated in LeVeque (2002) the numerical solution will change to the true one in the limit $\delta x \to 0$ and $\delta t \to 0$.

7.1.2 Implicit Method

On the other hand implicit methods use both, the old and the new solution to solve the set of equations. Formally this can be written as

$$\left(\frac{d\mathbf{x}}{dt}\right)^{old} \approx \frac{\mathbf{x}^{new} - \mathbf{x}^{old}}{\delta t} = F(\mathbf{x}^{old}, \mathbf{x}^{new}) \,. \tag{7.1.6}$$

Such systems of equations are usually non-linear and thus cannot be solved in an explicit way. However, the solution can be approximated iteratively by a root searching algorithm, e.g. by a Newton-Rhapson iteration. For this reason the entire system of equations has to be known for the old time (initial value problem). A set $\mathcal{G}_m$ of M equations per grid point can be rewritten for an arbitrary grid point $i \in N$ and at current time (t) as

$$\mathcal{G}_{m,i}\left(\mathbf{x}^{(t)}\right) = 0 \ \ m \in [1, M]\,, \tag{7.1.7}$$

so that they equal zero. This yields a system of $N \times M$ equations. For each grid-point $i \in [1, N]$ all equations $m \in [1, M]$ have to be solved. Since this system also has to be valid for the new time (t+1),

$$\mathcal{G}_{m,i}\left(\mathbf{x}^{(t+1)}\right) = 0 \ \ m \in [1, M]\,, \tag{7.1.8}$$

has to be valid too. This system of equations is not linear, hence it cannot be solved explicitly. However, a Taylor expansion around the old solution $\mathbf{x}^n$ can be done to approximate the solution. For an arbitrary gird point i this can be written as

$$\mathcal{G}_{m,i}\left(x^{(t+1)}\right) = \mathcal{G}_{m,i}\left(x^{(t)}\right) + \sum_{j=1}^{N} \frac{\partial \mathcal{G}_{m,i}\left(x^{(t)}\right)}{\partial x_j^{(t)}} \left(x_j^{(t+1)} - x_j^{(t)}\right) + \mathcal{O}\left[\left(x^{(t+1)} - x^{(t)}\right)^2\right]$$

$$\approx \mathcal{G}_{m,i}\left(x^{(t)}\right) + \underbrace{\sum_{j=1}^{N} \frac{\partial \mathcal{G}_{m,i}\left(x^{(t)}\right)}{\partial x_j^{(t)}} \left(x_j^{(t+1)} - x_j^{(t)}\right)}_{\mathcal{J}_{m,i}} \qquad .$$

$$\tag{7.1.9}$$

Where the derivatives denote for elements of the Jacobin matrix $\mathcal{J}_{m,i}$. This is clear by writing this in detail

$$\mathcal{G}_m\left(x^{(t+1)}\right) = \begin{pmatrix} \mathcal{G}_{m,1}\left(x^{(t+1)}\right) \\ \mathcal{G}_{m,2}\left(x^{(t+1)}\right) \\ \vdots \\ \mathcal{G}_{m,N}\left(x^{(t+1)}\right) \end{pmatrix}$$

$$\approx \begin{pmatrix} \mathcal{G}_{m,1}\left(x^{(t)}\right) \\ \mathcal{G}_{m,2}\left(x^{(t)}\right) \\ \vdots \\ \mathcal{G}_{m,N}\left(x^{(t)}\right) \end{pmatrix} + \underbrace{\begin{pmatrix} \frac{\partial \mathcal{G}_{m,1}\left(x^{(t)}\right)}{\partial x_1} & \cdots & \frac{\partial \mathcal{G}_{m,1}\left(x^{(t)}\right)}{\partial x_N} \\ \vdots & \ddots & \vdots \\ \frac{\partial \mathcal{G}_{m,N}\left(x^{(t)}\right)}{\partial x_1} & \cdots & \frac{\partial \mathcal{G}_{m,N}\left(x^{(t)}\right)}{\partial x_N} \end{pmatrix}}_{\mathcal{J}_m} \begin{pmatrix} \delta \mathbf{x}_1 \\ \vdots \\ \delta \mathbf{x}_N \end{pmatrix} = 0$$

$$\tag{7.1.10}$$

the Jacobian-matrix for a variable m is denoted as $\mathcal{J}_m$ and $\delta \mathbf{x}_i = \mathbf{x}_i^{(t+1)} - \mathbf{x}_i^{(t)}$. By inversion of matrix $\mathcal{J}_m$ the solution vector $\mathbf{x}_i^{(t+1)}$ for an arbitrary grid-point i at the new time can be computed by

$$\mathbf{x}_i^{(t+1)} = \mathbf{x}_i^{(t)} - \mathcal{J}_{m,i}^{-1} \mathcal{G}_{m,i}\left(\mathbf{x}^{(t)}\right)\,. \tag{7.1.11}$$

Since this is an first order approximation, the above described procedure is repeated until a certain accuracy ϵ is attained (e.g. LeVeque et al. 1997)

$$\left(\frac{|\delta\mathbf{x}_{i,m}|}{|\mathbf{x}_{i,m}| + \eta_{i,m}} \right) \leq \epsilon \,, \tag{7.1.12}$$

where m = 1...M is the number of the variable/equation (see Eq. 7.1.1). The value $\eta_{i,m} \ll \mathbf{x}_{i,m}$ is introduced to avoid a division by zero.

7.2   Discretization

The numerical integration of differential equations requires a discretization of space, time and all equations. Therefore, a physical system like a protoplanetary disk is divided into a number of cells which define a radial grid. The conservative quantitities (mass, energy and momentum) are redistributed form one cell to an other during the simulation. To ensure, that the conservation laws are not violated, an adequate advection scheme has to be utilized. In this section, I closely follows Stökl & Dorfi (2014) but without taking advantage of the adaptive grid.

7.2.1   Computational Domain

The computational domain is the space, that extends from the inner boundary to outer boundary of the protoplanetary disk. Gridpoints are logarithmically distributed, where the innermost grid point is denoted as i = 1 and the outermost as i = N. A grid cell can be seen as the minimum spatial resolution which spans from a grid point i to an adjacent gridpoint i + 1. The discretization of the given system of time-dependent partial differential equations (see Chapter 6) at a given grid point i needs (e.g. for the derivatives and differences) also needs solutions of neighboring grid points. In this thesis a *5-point stencil* is utilized to relate the next two adjacent grid points (see Figure 7.2).
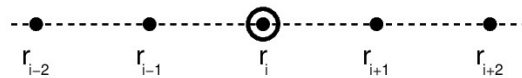
Figure 7.2: Shematic view of a *5-point stencil* for a 1D simulation. The term r_i represents the radius at the i − th grid point. Credits: Alexander Stökl.

Following LeVeque (2002), the values calculated in the simulation are defined

- in the middle of a grid cell, if the value is a scalar quantity (e.g. density ρ, volume ΔV, energy e or temperature T) or

- on the cell boundaries, if the value is a vectorial quantity (e.g. velocity $\mathbf{u}$ or flux).

This method is known as "staggered mesh" and can be seen as two different grids that superpose as shown in Figure 7.3. The vectorial grid cell or vectorial

volumina (see Figure 7.3, *vect. Vol.*) are shifted with respect to the scalar grid or scalar volumina (see Figure 7.3, *scal. Vol.*).
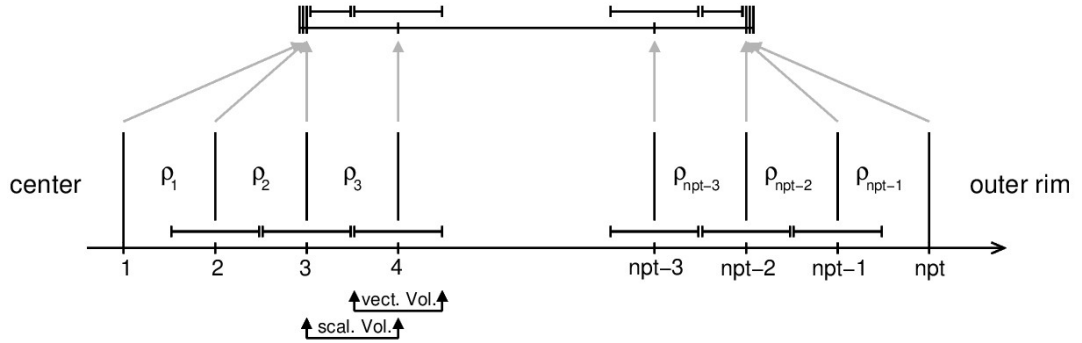
Figure 7.3: This figure represents an overall picture of a cylindrical (or spherical) configuration in one dimension. In this notation *npt* stands for "number of points" and is referred to as N in this thesis. Commonly, for a staggered mesh, a scalar quantity, like the density ρ_1 for the grid point i = 1, is defined in the middle of the 1*st* grid cell. Credits: Alexander Stökl

Figure 7.3 shows that the *5-point stencil* extends the physical domain (Gridpoint i = 3 to i = N − 2) of the protoplanetary disk by two additional grid points at the inner and outer boundary. The first tow grid points i = 1, 2 and the last two grid points i = N − 1, N are referred to as "ghost cells" and are not part of the physical disk but keep the Jacobi-matrix structure simple. Ghost cells have zero volume and are described via a set of boundary conditions (see Section 7.2.2).

7.2.2   Boundary Conditions

In reality, the protostellar disk, the central star and the environment oft this system are highly coupled. In disk simulations it is elaborate to consistently simulate a star and the interstellar environment. Instead of that, the numerical domain is limited to the protostellar disk and boundary conditions are utilized to specify the equations on the outer edge of the disk.

The boundary conditions have to be chosen carefully since they have high impact on the evolution of the protoplanetary disk (Ragossnig et al. 2019a). The proper definition of the inner and outer boundary of the protostellar disk is hard to specify. The inner boundary of the disk is highly coupled to the stellar magnetic field and rotational speed of the star. Inevitably, the disk eventually couples to the central star, so additionally stellar parameters like, stellar mass, radius and luminousity have high impact onto the inner edge of the disk. The outer boundary is in principle defined by the transition to ISM (interstellar medium) values and the ambient temperature. Moreover, the implicit nature of the code and the associated matrix inversion (see. Chapter 7.1) requires boundary conditions that keep the matrix regular. Otherwise an inversion would not be possible.

The definition of the boundary conditions depends on the actual problem and thus multiple interpretations are possible. This work implements the following definitions.

- Constant boundary values: In this case the innermost (i = 1) and outermost (i = N) grid points are set to a constant value $\mathbf{x}_{inner}$ and $\mathbf{x}_{outer}$, respectively. This has to be defined for each equation m.

$$\mathcal{G}_{m,1} = 0 = \mathbf{x}_1 - \mathbf{x}_{inner}$$

$$\mathcal{G}_{m,N} = 0 = \mathbf{x}_N - \mathbf{x}_{outer}$$

- Zero gradient at the outer boundary: In this case the values for two adjacent cells are set equal, to ensure a zero gradient.

$$\mathcal{G}_{m,1} = 0 = \mathbf{x}_1 - \mathbf{x}_2$$

$$\mathcal{G}_{m,N} = 0 = \mathbf{x}_N - \mathbf{x}_{N-1}$$

An example for the zero gradient boundary is to ensure a pressure-less flow over the boundaries of the disk.

7.2.3 Advection

The equations of hydrodynamics (see Chapter 6) are formulated as conservative equations. Hence, the quantities (mass, momentum and energy) described by these equations, are conserved during any physical process. Considering a physical process of a flowing fluid it is important to use methods that do not violate the conservation laws if this process is described in a finite numerical space. This advection step is illustrated in Figure 7.4.
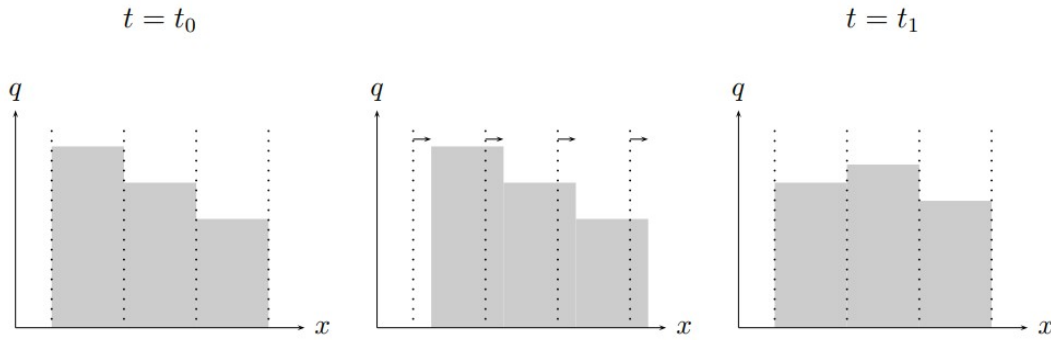
Figure 7.4: A conservative quantity q within a cell (space between the dashed lines) is transported to the adjacent cell from time $t = t_0 \to t_1$. During that flux from one to an other cell (denoted with the arrows in the middle plot) this quantity has to be conserved. Credits: Florian Ragossnig

The simplest scheme, that facilitates the conservation of flux, is the Donor-Cell advection (e.g. LeVeque 2002). This scheme assumes, that the conserved quantity q remains constant within a cell. Considering a flux $\mathcal{F}_i$ across the boundary of a cell i with a velocity u_i, the direction of the flow depends on the sign of the velocity. Depending on the selected coordinate system, the matter flows in the positive direction if $u_i > 0$ or in the negative direction if $u_i < 0$. For explicit integration schemes, the time-step $t = t_0 \to t_1$ is limited due to the CFL

condition (see Chapter 7.1) to ensure, that the time-step is is smaller than the velocity/sound-crossing time through a computational cell.

$$\mathcal{F}_i = \begin{cases} \tilde{q}_i u_i \text{ for } u_i < 0 \\ \tilde{q}_{i-1} u_i \text{ for } u_i > 0 \end{cases}$$

where $\tilde{q}$ is the advected quantity. In this case a positive direction of counting (left to right) from x_1 at the inner to x_N at the outer boundary is utilized. Note that scalar quantities (e.g. mass, energy, ...) are defined in the middle of a grid cell, so $\tilde{q} = q_{i+1/2}$ (see staggered mesh, Subsection 7.2.1). The calculation of the flux for the Donor-Cell advection scheme is illustrated in Figure 7.5. For the transport of a scalar quantity with a velocity $u_i < 0$ across the cell boundary i, the quantity to the right of this border is used to calculate the flux $\mathcal{F}^- = \tilde{q}_i u_i$ (e.g. mass is accreted towards the star, if the radius increases from the center of the star to the outer edge of the disk).
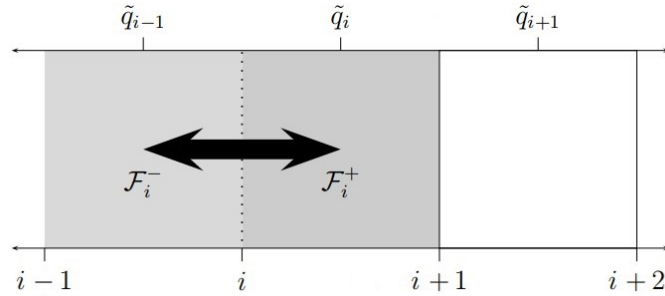
Figure 7.5: A conserved quantity $\tilde{q}$ remains constant within a cell. Depending on the direction of flow across an arbitrary cell boundary i, the quantity left ($\tilde{q}_{i-1}$) or right ($\tilde{q}_i$) is used to calculate the flux $\mathcal{F}_i$. Credits: Florian Ragossnig

Although this scheme is easily applicable it is a first order advection scheme and thus very diffusive. In this thesis, the a second order advection scheme developed by van Leer (1977) is used to compute the flux, which modifies the advected quantities by constructed internal slopes.

7.2.4   Scalar Discretization
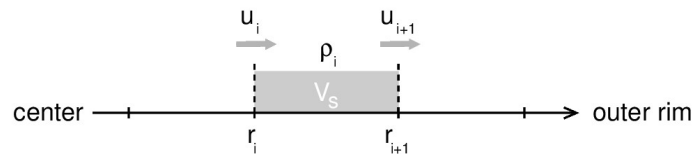
Figure 7.6: Discretization of a volume for scalar quantities (in the following section, $V_S = S_{vol,i}$). Credits: Alexander Stökl

Scalar volume element

Figure7.6 shows the scalar discretization of the integration volume. The arrows indicate the direction the flow (positive velocities). The volume inside a cell

between r_i and r_{i+1} reads

$$S_{\text{vol,i}} = \pi \left(r_{i+1}^2 - r_i^2 \right) .\tag{7.2.1}$$

Scalar flux element

The advected volume, which is transported over the cell boundaries a flux element is defined as

$$S_{\text{flux,i}} = 2\pi r_i u_i \delta t = S_i u_i \delta t ,\tag{7.2.2}$$

where δt represents the time step and $S_i = 2\pi r_i$ the element of the annulus at r_i

7.2.5 Vectorial Discretization
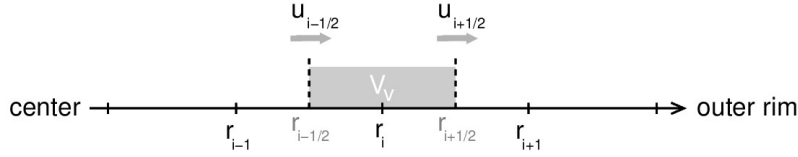
Figure 7.7: Discretization of a volume for vectorial quantitities (in the following section, $V_V = V_{\text{vol,i}}$). Credits: Alexander Stökl

Vectorial volume element

$$V_{\text{vol,i}} = \pi \left(r_{i+\frac{1}{2}}^2 - r_{i-\frac{1}{2}}^2 \right) = \frac{\pi}{2} \left(r_{i+1}^2 - r_{i-1}^2 \right)\tag{7.2.3}$$

where

$$r_{i+\frac{1}{2}}^2 = \frac{1}{2} \left(r_i^2 + r_{i+1}^2 \right)\tag{7.2.4}$$

By adding $\frac{\pi}{2}(r_i^2 - r_i^2)$ to the left and right hand side of Eq. 7.2.3 gives

$$\frac{\pi}{2} \left(r_{i+1}^2 - r_{i-1}^2 \right) + \frac{\pi}{2}(r_i^2 - r_i^2) = \frac{\pi}{2} \left(\underbrace{r_{i+1}^2 - r_i^2}_{S_{\text{vol,i}}/\pi} + \underbrace{r_i^2 - r_{i-1}^2}_{S_{\text{vol,i-1}}/\pi} \right) ,\tag{7.2.5}$$

and thus V_{vol} can be expressed with the corresponding scalar volumes

$$V_{\text{vol,i}} = \frac{1}{2} \left(S_{\text{vol,i}} + S_{\text{vol,i-1}} \right) .\tag{7.2.6}$$

Vectorial flux element

The advective volume flux is calculated analogous to $S_{\text{flux,i}}$

$$u_{i+\frac{1}{2}} r_{i+\frac{1}{2}} = \frac{1}{2} \left(u_i r_i + u_{i+1} r_{i+1} \right) ,\tag{7.2.7}$$

$$V_{\text{flux,i}} = 2\pi r_{i+\frac{1}{2}} u_{i+\frac{1}{2}} \delta t = \pi \left(u_i r_i + u_{i+1} r_{i+1} \right) \delta t .\tag{7.2.8}$$

7.2.6 Integrated and Derived Quantities

The discretization of the integrated complete set of conservative equations (see Chapter 6) requires also the discretization of volume integrated, derived and advected quantities. This is possible by utilizing the discretization rules described in the subsections 7.2.4 and 7.2.5. If Φ is a scalar quantity $S_{vol,i}$ (the scalar volume element) and $S_{flux,i}$ (the scalar flux element) are used and vice versa for a vectorial quantity.

Integral over the Control Volume

The integral of a scalar quantity over the control volume reads

$$\int_V \Phi \, dV \Rightarrow \Phi_i S_{vol,i} \, . \tag{7.2.9}$$

Partial Temporal Derivative

The partial temporal derivative of a scalar quantity can be expressed as

$$\frac{\partial}{\partial t} \Phi = \partial_t \Phi \Rightarrow \frac{\delta}{\delta t} \Phi_i = \frac{1}{\delta t} \left(\Phi_i - \Phi_i^{old} \right) \, , \tag{7.2.10}$$

where stands δt for the time step, Φ_i for the value at the new, Φ_i^{old} the value at the old time at the grid point i.

Volume and Advection Term

The conservation of mass, momentum and energy is basically described by a volume and an advection term (e.g. Landau & Lifschitz 2019). The volume term can be discretized as

$$\frac{\partial}{\partial t} \int_V \Phi \, dV \approx \frac{1}{\delta t} \left[\left(\int_V \Phi \, dV \right) - \left(\int_V \Phi \, dV \right)^{old} \right] \tag{7.2.11}$$

where Φ stands for the value at the new and Φ^{old} the value at the old time step. Utilizing Eq. 7.2.9 to discretize the remaining integral leads to an expression for the discretized volume term, that reads

$$\frac{\partial}{\partial t} \int_V \Phi \, dV \Rightarrow \frac{\delta}{\delta t} \Phi_i S_{vol,i} = \frac{1}{\delta t} \left(\Phi_i S_{vol,i} - \Phi_i^{old} S_{vol,i}^{old} \right) \, . \tag{7.2.12}$$

The advection term is defined as the integral over the boundary surface of the integration volume with flux $\Phi \mathbf{u}$. The replacement $S \rightarrow S_{flux}$ is done by utilizing Eq. 7.2.2.

$$\oint_{\partial V = S(V)} \Phi \mathbf{u} \cdot \mathbf{n} \, dS \Rightarrow \Phi_{i+1} u_{i+1} S_{i+1} - \Phi_i u_i S_i = \Phi_{i+1} \frac{S_{flux,i+1}}{\delta t} - \Phi_i \frac{S_{flux,i}}{\delta t} \tag{7.2.13}$$

Using this scheme, all equations of RHD (see Chapter 6) can be discretized.

7.2.7 Discretization of the Equation of Continuity

The procedure when discretizing the physical equations (see Chapter 6) will be first demonstrated on basis of the equation if continuity. Thus, utilizing the integrated form and identifying temporal difference and the advection form, Eq. 4.4.3 reads

$$\underbrace{\frac{\partial}{\partial t} \int_V \rho \, dV}_{①} + \underbrace{\oint_{\partial V = S(V)} \rho \mathbf{u} \cdot \mathbf{n} \, dS}_{②} = 0 \,. \tag{7.2.14}$$

Applying the discretization of the volume term ① (Eq. 7.2.12) and the advection term ② (Eq. 7.2.13) gives

$$① \; : \; \frac{1}{\delta t} \left(\rho_i S_{\text{vol},i} - \rho_i^{\text{old}} S_{\text{vol},i}^{\text{old}} \right) \,, \tag{7.2.15}$$

$$② \; : \; \tilde{\rho}_{i+1} \frac{S_{\text{flux},i+1}}{\delta t} - \tilde{\rho}_i \frac{S_{\text{flux},i}}{\delta t} \,. \tag{7.2.16}$$

After reorganizing and multiplying by δt, the discrete form of the equation of continuity reads

$$\rho_i S_{\text{vol},i} - \rho_i^{\text{old}} S_{\text{vol},i}^{\text{old}} + \tilde{\rho}_{i+1} S_{\text{flux},i+1} - \tilde{\rho}_i S_{\text{flux},i} = 0 \,. \tag{7.2.17}$$

A quantity $\tilde{\Phi}$ is advected with the flux S_{vol} depending on the used advection scheme (see Subsection 7.2.3).

7.2.8 Discretization of the Equation of Motion

Due to the geometry of a protostellar disk, the equations are written in cylindrical coordinates. Hence, the equation of motion is splitted into an r-component (radial) and φ-component (toroidal). Since similar considerations are done for both, just the radial component is discussed in the following. The integration form of Eq. 4.5.9 reads

$$\underbrace{\partial_t \int_V \rho \mathbf{u} \, dV}_{①} + \underbrace{\int_V \nabla \cdot (\rho \mathbf{u} \mathbf{u}) \, \mathbf{n} dS}_{②} + \underbrace{\int_V \nabla P \, dV}_{③} + \underbrace{\int_V \rho \nabla \psi \, dV}_{④} + \underbrace{\int_V \nabla \cdot \underline{\underline{Q}} \, dV}_{⑤} = 0 \,,$$
$$\tag{7.2.18}$$

where

$$\nabla \psi = -\frac{\text{GM}_\star}{\text{r}^2} \,. \tag{7.2.19}$$

The discussed discretization scheme is utilized on ① to ⑤. Due to the staggered mesh, spatial differences are defined between gird points $(i+1)$ and (i) for scalar and between (i) and $(i-1)$ for vectorial volume elements.

$$① \; : \; \frac{\delta}{\delta t} \left(\rho_i u_i V_{\text{vol},i} \right) = \frac{1}{\delta t} \left(\rho_i u_i V_{\text{vol},i} - \rho_i^{\text{old}} u_i^{\text{old}} V_{\text{vol},i}^{\text{old}} \right) \tag{7.2.20}$$

The equations are solved in cylindrical coordinates, thus the divergence in ② has to be rewritten. The r-component reads

$$[\nabla(\rho\mathbf{u}\mathbf{u})]_r = \frac{1}{r}\partial_r\left(r\rho u_r u_r\right) - \frac{\rho u_\varphi u_\varphi}{r}\,, \qquad (7.2.21)$$

if skipping the derivatives ∂_φ and ∂_z. Integration over the cell volume leads to

$$\int_V [\nabla(\rho\mathbf{u}\mathbf{u})]_r\ dV = \int_{\bar{r}_{i-1}}^{\bar{r}_i}\frac{1}{r}\partial_r\left(r\rho u_r u_r\right)\ 2\pi r dr - \int_V \frac{\rho u_\varphi u_\varphi}{r}\ dV\,, \qquad (7.2.22)$$

where the first term can be identified as advection term and the second one as centrifugal force. Discretization aims

$$2\pi\Delta\left(\bar{r}\rho\bar{u}_r\right) - \frac{\rho u_\varphi u_\varphi}{r}V_{\mathrm{vol}}\,, \qquad (7.2.23)$$

for the right part of Eq. 7.2.22, where $\bar{r}$ and $\bar{u}_r$ denote for radii and velocities at half indices. The spatial difference Δ denotes for the difference between values at grid point i and $i-1$, because the velocity is a vectorial quantity. By using Eq. 7.2.8 the first part can be written as

$$\tilde{p}_i\frac{V_{\mathrm{flux},i}}{\delta t} - \tilde{p}_{i-1}\frac{V_{\mathrm{flux},i-1}}{\delta t}\ \text{where}\ \tilde{p}_n = \rho_n u_n\,. \qquad (7.2.24)$$

For the second part V_{vol} is expressed by the scalar volume element S_{vol} using Eq. 7.2.6 and thus reads

$$\frac{1}{2r_i}\left(u_{\varphi,i}^2 S_{\mathrm{vol},i} + u_{\varphi,i-1}^2 S_{\mathrm{vol},i-1}\right)\rho_i\,. \qquad (7.2.25)$$

For the discretization of the gas pressure term it is necessary to write the gradient in cylindrical coordinates and dropping every derivation besides the radial component. Utilizing an isotropic gas pressure, the gradient in ③ reads

$$\nabla P = \partial_r P = \frac{\partial P}{\partial r}\,. \qquad (7.2.26)$$

Integration is easier if the transformation $dV = 2\pi r\ dr$ is done, the integral can be rewritten as

$$\int_V \frac{\partial P}{\partial r}\ dV = \int_r \frac{\partial P}{\partial r}\ 2\pi r\ dr \approx 2\pi r\int_r \frac{\partial P}{\partial r}\ dr \Rightarrow 2\pi r_i(P_i - P_{i-1})\,. \qquad (7.2.27)$$

The gas pressure P has to be integrated in z-direction in principle. This can be done by using the scale height H_P and the same procedure utilized for the calculation if the mid-plane density (see Eq. 5.5.12). Hence, the z-integrated gas pressure in the disk can be expressed by the mid-plane gas pressure P_0 using

$$P_i = P_{0,i}\sqrt{2\pi}H_{P,i}\,, \qquad (7.2.28)$$

for an arbitrary grid point i. Thus

$$③\ :\ 2\pi r_i\sqrt{2\pi}\left(P_{0,i}H_{P,i} - P_{0,i-1}H_{P,i-1}\right)\,, \qquad (7.2.29)$$

$$\text{④} : -\rho_i \frac{GM_\star}{r_i^2} V_{vol,i} . \tag{7.2.30}$$

In the following the viscous pressure term is discretized. The definition of the viscous pressure tensor (see 10.1.12) reads

$$\underline{\underline{Q}} = \mu_Q \left[[\nabla \mathbf{u}]_s - \mathbb{1}\frac{1}{2}\nabla \cdot \mathbf{u} \right] , \tag{7.2.31}$$

where $[\nabla \mathbf{u}]_s$ is the symmetric velocity gradient. Utilizing the description of Tscharnuter & Winkler (1979) in cylindrical coordinates, the radial component of the divergence of the viscous pressure tensor can be written as

$$\left(\nabla \cdot \underline{\underline{Q}} \right)_r = -\frac{2}{r}\frac{\partial}{\partial r^2} \left[r^2 \mu_Q \frac{1}{2} \left(\frac{\partial u_r}{\partial r} - \frac{u_r}{r} \right) \right] , \tag{7.2.32}$$

where μ_Q is the dynamic viscosity. To discretize the differential operator in the equation above Eq. 7.2.3 is used and rewritten as difference,

$$V_{vol,i} = \pi \left(r_{i+\frac{1}{2}}^2 - r_{i-\frac{1}{2}}^2 \right) \rightarrow V_{vol} = \pi \Delta(\bar{r}^2) , \tag{7.2.33}$$

where $\bar{r}$ denotes for radii at half indices. Thus, the differential operator in Eq. 7.2.34 can be discretized as

$$\frac{\partial}{\partial r^2} \rightarrow \frac{\Delta}{\Delta \bar{r}^2} = \frac{\pi}{V_{vol}}\Delta . \tag{7.2.34}$$

To calculate vectorial and scalar quantities at the same discrete location, it is important to treat quantities in spatial differences (denoted by Δ) in Eq. 7.2.32 correctly if replacing the differential operator by Eq. 7.2.34. The Δ alternates between whole and half indices. Hence, defining Eq. 7.2.32 at the $i-$th grid point, the expression $\frac{2}{r}$ outside the brackets becomes $\frac{2}{r_i}$, while the radius in the brackets needs to be a half quantity $(r^2 \rightarrow \bar{r}^2 = r_{i+\frac{1}{2}}^2)$ so that the same discrete location i is attained after taking the difference. The velocity term has to be treated the same way. Thus Eq. 7.2.32 can be approximated by

$$\left(\nabla \cdot \underline{\underline{Q}} \right)_r \approx -\frac{2}{r}\frac{\pi}{V_{vol}}\Delta \left[\bar{r}^2 \mu_Q \frac{1}{2} \left(\frac{\Delta u_r}{\Delta r} - \frac{\bar{u}_r}{\bar{r}} \right) \right] . \tag{7.2.35}$$

We can approximate the integral ⑤ and substitute Eq. 7.2.35 afterwards into this equation.

$$\int_V \nabla \cdot \underline{\underline{Q}} dV \approx \left(\nabla \cdot \underline{\underline{Q}} \right)_r V_{vol} = -\frac{\pi}{r}\Delta \left[\bar{r}^2 \mu_Q \left(\frac{\Delta u_r}{\Delta r} - \frac{\bar{u}_r}{\bar{r}} \right) \right] \tag{7.2.36}$$

$$\text{⑤} : \frac{\pi}{r_i} \left[\mu_{Q,i} \left(\frac{r_{i+1}^2 + r_i^2}{2} \right) U_{r,i} - \mu_{Q,i-1} \left(\frac{r_i^2 + r_{i-1}^2}{2} \right) U_{r,i-1} \right] \tag{7.2.37}$$

where $U_{r,n}$ for n either i or $i-1$ denotes for the velocity term. Recalling Eq. 7.2.7, the velocity at half index $i+\frac{1}{2}$ can be written as

$$u_{i+\frac{1}{2}} = \frac{1}{2}\frac{(u_i r_i + u_{i+1}r_{i+1})}{r_{i+\frac{1}{2}}} \rightarrow \frac{u_{i+\frac{1}{2}}}{r_{i+\frac{1}{2}}} = \frac{1}{2}\frac{(u_i r_i + u_{i+1}r_{i+1})}{r_{i+\frac{1}{2}}^2} \tag{7.2.38}$$

Substituting Eq. 7.2.4 into the equation above gives

$$\frac{u_{i+\frac{1}{2}}}{r_{i+\frac{1}{2}}} = \frac{u_i r_i + u_{i+1} r_{i+1}}{r_i^2 + r_{i+1}^2} \tag{7.2.39}$$

for the ratio between the velocity and the radius for half indices. Using this formalism the velocity term in r-direction can be discretized as follows.

$$U_n = \frac{u_{n+1} - u_n}{r_{n+1} - r_n} - \frac{u_n r_n + u_{n+1} r_{n+1}}{r_n^2 + r_{n+1}^2} \tag{7.2.40}$$

The discretization of μ_Q is also described by Tscharnuter & Winkler (1979), reading

$$\mu_Q = -q_1 \lambda c_S + q_2^2 \lambda^2 \max(-\nabla \cdot \mathbf{u}, 0) \tag{7.2.41}$$

where λ is a typical viscous length. The variables q_1 and q_2 are weights for linear and quadratic viscosity, respectively.

7.2.9 Discretization of the Equation of Energy

Ignoring the heat due to diffusion $\mathbf{q}$, the integration of Eq. 4.6.2 leads to

$$\partial_t \underbrace{\int_V \rho e \, dV}_{①} + \underbrace{\oint_{\partial V = S(V)} \rho \mathbf{u} e \, \mathbf{n} \, dS}_{②} + \underbrace{\int_V P \nabla \cdot \mathbf{u} \, dV}_{③} +$$
$$\underbrace{\int_V \underline{\underline{Q}} : \nabla \mathbf{u} \, dV}_{④} - \underbrace{4\pi \int_V \rho \kappa \, (J - S) \, dV}_{⑤} = 0 \, . \tag{7.2.42}$$

Since the energy is a scalar quantity, the scalar volume element for the $i-$th cell $V_{S,i}$ is used for the discretization. The terms ① and ② in discretized form read

$$① : \frac{\delta}{\delta t} \left(\rho_i e_i S_{\text{vol},i} \right) = \frac{1}{\delta t} \left(\rho_i e_i S_{\text{vol},i} - \rho_i^{\text{old}} e_i^{\text{old}} S_{\text{vol},i}^{\text{old}} \right) , \tag{7.2.43}$$

$$② : \tilde{b}_i \frac{S_{\text{flux},i}}{\delta t} - \tilde{b}_{i-1} \frac{S_{\text{flux},i-1}}{\delta t} \quad \text{where } b_n = \rho_n e_n \, . \tag{7.2.44}$$

For term ③, the pressure P is considered as averaged value for the respective discretized volume. Hence, P can be drawn out of the integration and thus reads

$$\int_V P \nabla \cdot \mathbf{u} \, dV \approx P \int_V \nabla \cdot \mathbf{u} \, . \tag{7.2.45}$$

Since the equations are calculated in cylindrical geometry, $\nabla \cdot \mathbf{u}$ has to be rewritten as

$$\nabla \cdot \mathbf{u} = \frac{1}{r} \partial_r \left(r u_r \right) \, . \tag{7.2.46}$$

Using these results, integration of over the scalar cell volume in cylindrical geometry yields

$$P \int_V \nabla \cdot \mathbf{u} = P \int_{r_i}^{r_{i+1}} \frac{1}{r} \partial_r (r u_r) \, dr \Rightarrow 2 P_i \pi \left(r_{i+1} u_{r,i+1} - r_i u_{r,i} \right). \tag{7.2.47}$$

Utilizing Eq. 7.2.28 to represent the z-integrated gas pressure by the mid-plane gas pressure the last equation can be assigned as

$$2\pi P_{0,i} \sqrt{2\pi} H_{P,i} \left(r_{i+1} u_{r,i+1} - r_i u_{r,i} \right). \tag{7.2.48}$$

The last step to complete ③ is to add a term describing the expansion in z-direction.

$$③ : 2\pi P_{0,i} \sqrt{2\pi} H_{P,i} \left(r_{i+1} u_{r,i+1} - r_i u_{r,i} \right) + P_{0,i} S_{vol,i} \left(H_{P,i} - H_{P,i}^{old} \right) \tag{7.2.49}$$

For ④ the velocity tensor $\nabla \mathbf{u}$ and Eq. 7.2.31 are used. Simplification aims

$$\underline{\underline{Q}} : \nabla \mathbf{u} \approx -\frac{\mu_Q}{2} \left[\left(\partial_r u_r - \frac{u_r}{r} \right)^2 + \left(\partial_r u_\varphi - \frac{u_\varphi}{r} \right)^2 \right]. \tag{7.2.50}$$

The discretization is similar to Eq. 7.2.32 by rewriting the differential operator into differences. The right part of the last equation reads,

$$-\frac{\mu_Q}{2} \left[\left(\frac{\Delta u_r}{\Delta r} - \frac{\bar{u}_r}{\bar{r}} \right)^2 + \left(\frac{\Delta u_\varphi}{\Delta r} - \frac{\bar{u}_\varphi}{\bar{r}} \right)^2 \right]. \tag{7.2.51}$$

Further discretization yields,

$$④ : -\frac{\mu_{Q,i}}{2} \left(U_{r,i}^2 + U_{\varphi,i}^2 \right) S_{vol,i}, \tag{7.2.52}$$

where the velocity terms $U_{r,i}$ and $U_{\varphi,i}$ are discretized using Eq. 7.2.40.

For ⑤ some simplifications are necessary (Ragossnig et al. 2019a). If only considering the dominant terms of the radiation equations the simplification

$$\kappa \rho (J - S) = -\nabla \cdot \mathbf{H} \tag{7.2.53}$$

and

$$\kappa \rho \mathbf{H} = -\nabla \cdot \underline{\underline{K}} \approx \nabla \left(f_{edd} J \right) \tag{7.2.54}$$

where f_{edd} is the Eddington factor, $\mathbf{H}$ is the first moment (radiation flux) and $\underline{\underline{K}}$ is the second (radiation pressure) moment of the radiation transport. Skipping all derivatives beside the radial, Eq. 7.2.54 reads

$$\nabla \cdot \mathbf{H} \approx \frac{1}{r} \partial_r (r H_r). \tag{7.2.55}$$

Utilizing Eq. 7.2.53, the integral ⑤ reads

$$-4\pi \int_V \rho \kappa (J - S) \, dV = 4\pi \int_V \nabla \cdot \mathbf{H} \, dV = \int_{r_i}^{r_{i+1}} dr \int_{-\pi}^{\pi} r \nabla \cdot \mathbf{H} d\varphi, \tag{7.2.56}$$

and can be solved by substituting Eq. 7.2.55

$$\int_{r_i}^{r_{i+1}} \frac{1}{r} \partial_r \left(r H_r \right) 2\pi r \, dr = 4\pi 2\pi \Delta \left(r H_r \right) . \tag{7.2.57}$$

This equation can be expressed by the mid-plane radiation flux H_0 in the stationary limit. After further simplifications Eq. 7.2.57 reads

$$4\pi 2\pi \Delta \left(r H_r \right) \rightarrow 8\pi^2 \sqrt{2\pi} H_P \Delta \left(r H_0 \right) , \tag{7.2.58}$$

where H_P is the pressure scale height. Assuming, that pure radiation diffusion terms are more significant then time depended terms in the radiation flux equation, its simplified discretized version for and isotropic flux, $f_{edd} = \frac{1}{3}$ reads

$$\frac{2}{3} r \sigma \Delta \left(T^4 \right) + \overline{\kappa_R \rho_0} H_0 V_{vol} = 0 . \tag{7.2.59}$$

This gives an expression for H_0 by rearranging Eq. 7.2.59 equation

$$H_0 = -\frac{\frac{2}{3} r \sigma \Delta \left(T^4 \right)}{\kappa_R \rho_0 V_{vol}} . \tag{7.2.60}$$

Substituting Eq. 7.2.60 into Eq. 7.2.58 the discretization of ⑤ is obtained

$$⑤ : 8\pi^2 \sqrt{2\pi} H_P \Delta \left(\frac{\frac{2}{3} r^2 \sigma \Delta \left(T^4 \right)}{\kappa_R \rho_0 V_{vol}} \right) . \tag{7.2.61}$$

In the last step, the difference operator Δ has to be discretized (see e.g. Section 7.2.8).

Additionally, a term,

$$\Delta E = E_{irr} - E_{cool} + E_{amb} + F_{vert} , \tag{7.2.62}$$

considering the contribution of the stellar radiation E_{irr}, energy loss due to cooling E_{cool}, the influence of the ambient temperature, covered in E_{amb} and the vertical energy transfer F_{vert} has to be added to the equation of energy. Assuming the optical thin case, where the temperature within the disk adjusts to the value of the mid-plane temperature, as well as black body radiation, the vertical energy term can be neglected and the individual discretized energy terms can be written as

$$E_{irr} = 4\pi \kappa_P \rho_0 \sqrt{2\pi} H_P \frac{\sigma}{\pi} T_\star^4 S_{vol} \delta t \tag{7.2.63}$$

$$E_{amb} = 4\pi \kappa_P \rho_0 \sqrt{2\pi} H_P \frac{\sigma}{\pi} T_{amb}^4 S_{vol} \delta t , \tag{7.2.64}$$

$$E_{cool} = 4\pi \kappa_P \rho_0 \sqrt{2\pi} H_P \frac{\sigma}{\pi} T_0^4 S_{vol} \delta t \text{ and} \tag{7.2.65}$$

where κ_P is Planck's opacity and T_{amb} is the ambient temperature. In the optical thin case, the gas within the disk cools according to the mid-plane temperature

T_0, there is no explicit surface temperature T_{surf}. $T_\star$ is the temperature of the stellar radiation field an can be expressed by

$$\sigma T_\star^4 = \frac{L_\star}{4\pi r^2} \ ,\tag{7.2.66}$$

and also the equilibrium temperature if heating and cooling happens in the same cross-section. Summarizing the individual contributors to the energy and after some simplifications the additional energy term ΔE can be written as

$$\Delta E = 4\pi \kappa_P \rho_0 \sqrt{2\pi} H_P \left(\sigma T_0^4 - \sigma T_{\text{amb}}^4 + \frac{L_\star}{4\pi r^2} \right) \ .\tag{7.2.67}$$

Chapter 8

Simulation and Model Description

In this chapter the setup of the numerical simulation and model of the protoplanetary disk are described.

The TAPIR (The AdaPtive Implicit Radiation-hydrodynamics) Code (e.g. Ragossnig et al. (2019a); Stoekl & Dorfi (2014)) is an implicit 1+1D code. It utilizes axial-symmetry to solve the equations of radiation hydrodynamics (RHD, see Chapter 6) in radial direction. Even though the model is limited to axis-symmetry, recent ALMA observations (see Section 3.2) and other disk model results (e.g. Boss & Hartmann (2001); Vorobyov (2010); Yorke & Bodenheimer (1999)) suggest, that protostellar disks spend most of their lifetime in an axis-symmetric state.

In further assumption the protostellar disk is geometrically thin (H $\ll$ R), so that a vertical force balance (hydrostatic equilibrium) above the disk mid-plane defines the vertical structure of the disk. Hence, the physical quantities can be calculated by integration in z-direction utilizing the equation of state (EOS) (Ragossnig et al. 2019a).

For geometrical thin disks and high stellar radiation flux, the temperature rises to several 1000 K in the inner region of the disk (Kamp & Dullemond 2004). This high temperatures and low disk masses ($M_{disk}/M_\star \approx 1\%$), ensure no gravitational instabilities (Q > 1, Toomre (1964)) and thus a 1+1D description is sufficient to investigate the long term evolution of disks (Ragossnig et al. 2019a).

The aim of the simulation is to show, that accretion outbursts (e.g. FU-Ori bursts, see Section 3.1) can be triggered by thermal instabilities. This requires a non-constant disk viscosity to account for regions of low viscosity (dead-zones). The viscosity model follows the description of Shakura & Sunyaev (1973) and is described in Section 8.2.

8.1   Initial Model

An implicit integration scheme requires an initial model, that represents a solution which is a full solution of the underlying RHD equations of the numerical problem. The convergence of the simulation to a physical solution can be ensured by a well choosed initial model (Dorfi & Drury 1987; LeVeque et al. 1997).

Note, that the following methods are only pseudo-iterations to generate a proper initial model. This is rather a numerical trick than actual physics.

The initial disk is assumed to exhibit a constant density distribution (e.g Bath & Pringle 1981)

$$\Sigma(r) = \Sigma_0 \, r^{-n} \, ,$$

where $n = 0$, r is the radius and Σ_0 is the surface density at the outer boundary of the disk. Stellar parameters, like luminousity $L_\star$, mass $M_\star$ and radius $R_\star$ are specified according to e.g. Palla & Stahler (1991). An initially constant radial velocity $u_r = $ const. and an angular velocity equally to the Keplarian velocity ($u_\varphi = u_K$) is assumed. The position of the inner and outer boundary is hard to specify (see Subsection 7.2.2). In this thesis the outer radius is set to the position where the disk density drops below the averaged density of the ISM. The inner radius is set to the co-rotation radius r_{co}. At this point the stellar rotation is equal to the angular velocity of the disk and mass is assumed to be accreted onto the star in free-fall. This represents a physical boundary of the disk. Following Ragossnig et al. (2019b), the stellar rotation period can be defined as fraction of the Keplarian orbital period on the stellar surface $\Omega_{K,\star}$

$$\Omega_\star = \beta \Omega_{K,\star} \, , \tag{8.1.1}$$

where $\beta = 0.1$ for stars with masses between $0.1 \, M_\odot < M_\star < 2.0 \, M_\odot$. Hence, the co-rotation radius reads

$$r_{co} = \left[\frac{GM_\star}{(\beta\Omega_{K,\star})^2} \right]^{1/3} . \tag{8.1.2}$$

For T Tauri stars, stellar periods of 2 days (Herbst et al. 2001) are usual. This yields $r_{co} = 0.025$ AU for a star with $M_\star = 1 \, M_\odot$.

A stepwise adjustment of an initially arbitrary model ensures a convergence towards the final physical solution. The first step enables the disk to adjust thermally to the stellar environment (thermal relaxation) without considering a fluid flow. In the second step pressureless in and outflow conditions are established so the disk can evolve thermally and dynamically until a steads state, viscous initial disk is achieved (cf. Ragossnig et al. 2019b).

All initial disks in this thesis contain 1% of the host stars mass to prohibit the existence of gravitational unstable regions within the disk (Toomre 1964).

8.2   Viscosity Model

The dynamic viscosity μ (see Eq. 5.3.9) is linked to the kinematic viscosity ν by the column density of the fluid in the disk Σ (since the disk is calculated by a 1+1D code, volumes are reduced to areas thus $\rho \rightarrow \Sigma$).

$$\mu_Q = \nu \, \Sigma \tag{8.2.1}$$

The description of the viscosity follows Eq. 5.4.5 and can be written according to Shakura & Sunyaev (1973) as

$$\nu = \frac{\alpha c_S^2}{\Omega} = \alpha c_S H_P \,, \qquad (8.2.2)$$

where α is the viscous parameter, c_S the isothermal sound speed and Ω the Keplarian angular momentum. Applying $c_S H_P^{-1}$, where H_P is the pressure scale height of the vertical hydrostatic structure and an isothermal equation of state (EOS) $P_{gas,0} = \rho_0 c_S^2$ (where the index 0 is referring to values in the mid-plane of the disk at $z = 0$) the dynamical viscosity can be rewritten as

$$\mu_Q = \alpha H_P \Sigma \sqrt{\frac{P_{gas,0}}{\rho_0}} \,, \qquad (8.2.3)$$

what defines the linear term of the viscosity as function of the scale height of the disk. The total viscosity parameter α accounts for different transport mechanisms, similar to Hartmann & Bae (2018). Therefore the disk is divided into two layers, an active surface and a deep layer (layered disk model, see Subsection 5.4.3) regarding the transport associated with the MRI. This gives a possibility to artificially add a dead-zone region in the disk.

The assembled total viscosity parameter of the disk thus is

$$\alpha = \alpha_{base} + \alpha_{surf} + \alpha_{deep} + \alpha_{grav} \,, \qquad (8.2.4)$$

where α_{surf} accounts for the MRI viscosity in active surface layers, ionized by external radiation and α_{deep} for the MRI viscosity in deep disk layers thermally ionized when the temperature exceeds for example $T_{active} = 1500\,K$ (Bae et al. 2013) for thermal ionization. The exact value for T_{active} depends on the dust-to-gas ration, the grain size and the gas density (Desch & Turner 2015). However, this threshold value for magneto-rotational turbulences is assumed to be higher then 1000 K (Flock et al. 2016). The α_{grav} quantifies the viscosity in parts of the disk that become gravitational unstable (GI) and α_{base} accounts for any non-GI/MRI transport (base value of the viscosity within the dead-zone).

The separation of the two layers is controlled by the density profile $\Sigma(r)$ of the disk and a fixed parameter Σ_0 that specifies the column density for the MRI-active surface layer. If the column density $\Sigma(r)$ at a given radius r exceeds a certain value of $\Sigma_0 \approx 100$ g cm^{-2} (e.g. Armitage 2010, p. 99), the disk consists of an additional deep layer. This is numerically solved by the implementation of a switch s that is s = 1 if there is an additional deep layer, and else is s = 0. Taking that in account, the viscosity parameters read

$$\alpha_{surf}(r) = \alpha_{MRI} \left[s \frac{\Sigma_0}{\Sigma(r)} + (1 - s) \right] \,, \qquad (8.2.5)$$

for the surface layer and

$$\alpha_{deep}(r) = \alpha_{MRI} \, s \left(1 - \frac{\Sigma_0}{\Sigma(r)} \right) \varepsilon(T_{gas,z}) \,, \qquad (8.2.6)$$

for the deep layer, where

$$\varepsilon(\mathrm{T_{gas,z}}) = \frac{1}{2}\left[1 + \tanh\left(\frac{\mathrm{T_{gas,z}} - \mathrm{T_{active}}}{\mathrm{T_{width}}}\right)\right],\qquad(8.2.7)$$

is utilized for convergence reasons during the Newton-Raphson-iteration. Eq. 8.2.7 smooths an otherwise step-like transition between MRI-inactive and MRI-active layers. Here, $\mathrm{T_{gas,z}}$ is the vertical integrated gas temperature, $\mathrm{T_{active}}$ the temperature for thermal ionization of hydrogen. The parameter $\mathrm{T_{width}} = 10 - 100$ K (Armitage 2010) establishes a smooth transition between an MRI active and inactive deep layer if $\mathrm{T_{gas,z}} > \mathrm{T_{active}}$ (similar to Flock et al. 2016).

Looking at these equations we can summarize, that in regions with lower density, and thus only consisting of a surface layer, external radiation is sufficient to ionize parts of the disk while regions with higher density, and thus with an additional deep layer, are partially ionized by external radiation and stellar radiation (if the activation temperature is reached). The viscosity parameter for gravitational instabilities is defined by the Toomre parameter $\mathrm{Q_T}$

$$\alpha_{\mathrm{grav}} = \alpha_{\mathrm{GI}}\ \zeta\ \left(\frac{\mathrm{Q_{T,crit}^2}}{\mathrm{Q_T^2}} - 1\right),\qquad(8.2.8)$$

where $\zeta = 1$ if $\mathrm{Q_{T,crit}} > \mathrm{Q_T}$ and otherwise $\zeta = 0$. This means that the gravitational viscosity parameter is only non-zero if the disk is gravitational unstable. In this simulation $\mathrm{Q_{T,crit}} = 1.5$ although $\mathrm{Q_{T,crit}} = 1$ (Toomre 1964) would have been sufficient. The masses of all disks were chosen so that they remain gravitationally stable throughout their lifetime. As described by Toomre (1964) the equation for the Toomre parameter can be written as

$$\mathrm{Q_T} = \frac{c_S\Omega}{\pi G\Sigma}.\qquad(8.2.9)$$

In this equation $c_S = \sqrt{P/\rho}$ is the isothermal speed of sound, $\Omega = \sqrt{\mathrm{GM_\star/R^3}}$ is the Keplerian angular velocity, G is the gravitational constant and Σ is the surface density. This equation can be rewritten by an energy equation and the adiabatic index Γ_1.

$$e = \frac{1}{\Gamma_1 - 1}\frac{P}{\rho} = \frac{1}{\Gamma_1 - 1}c_S^2 \rightarrow c_S = \sqrt{e(\Gamma_1 - 1)}\qquad(8.2.10)$$

By multiplying the equation above with Ω we get the following expression for the sound speed

$$c_S\Omega = \sqrt{\frac{e(\Gamma_1 - 1)\mathrm{M_\star}G}{\mathrm{R^3}}}.\qquad(8.2.11)$$

By substituting this term into Eq. 8.2.9 and drawing G into the square root the Toomre parameter reads

$$\mathrm{Q_T} = \sqrt{\frac{e(\Gamma_1 - 1)\mathrm{M_\star}}{\mathrm{R^3}G}}\frac{1}{\pi\Sigma}.\qquad(8.2.12)$$

Usual values for the viscosity parameters are $\alpha_{\mathrm{MRI}} = 0.01$ (Hartmann & Bae (2018); Zhu et al. (2010)), $\alpha_{\mathrm{base}} \approx 10^{-5} - 10^{-4}$ (Hartmann & Bae 2018) and

$\alpha_{\mathrm{GI}} = 0.01$ (only if the disk gets gravitational unstable), thus resulting in an overall value of $\alpha \approx 0.01$. As mentioned by Rafikov (2017) a value of $\alpha \approx 0.01$ corresponds to the explanation of observed averaged properties of protoplanetary disks by their viscous evolution, which was primarily found by Hartmann et al. (1998) and Calvet et al. (2000).

Chapter 9

Results and Discussion

In this chapter the results of the simulation are presented. I will show, how the onset of the stellar outburst is connected to a thermal instability close to the star and how disk parameters like scale height H_P, surface density Σ, gas temperature T_{gas} and viscosity parameter α. evolve from the on- to the off-set of the burst. Further, I present some examples of long term evolution of a protostellar disk, to show the periodical nature of the stellar burst. At last I will present the comparison of the simulation with observational data.

9.1 Burst Onset

It is assumed that variable accretion, such as stellar outbursts (e.g. FU-Ori outburst), requires the accumulation of material (e.g. Latter & Balbus 2012) within an region of low viscosity (dead-zone) at radii r < 0.5AU (Bae et al. 2013). A possible scenario for the onset of a burst is that a thermal instability (see Subsection 3.1.2) rapidly increases the accretion rate by releasing the stored mass within dead-zone. As expected the results (see Figure 9.2) show a rapid increase of T_{gas} as soon as a critical temperature $T_{crit} = 1500$ K (see Section 8.2) is exceeded. Additionally, the rise in viscosity within the dead-zone (see Figure 9.3) is demonstrated

The physical constraint for the onset of an accretion burst is demonstrated for a $M_\star = 0.1$ $M_\odot$ star and a disk that extents from $r = 0.02 - 1.54$ AU. The time-evolution shows the development from a MRI inactive to a fully MRI active deep disk layer. For the viscosity parameters $\alpha_{MRI} = 0.01$ for MRI active regions, $\alpha_{GI} = 0.01$ for gravitative unstable regions and $\alpha_{base} = 10^{-5}$ for a base viscosity are used. The following subsections show the evolution of the scale height H_P, surface density Σ, gas temperature T_{gas} and viscosity parameter α in 8 time steps (τ_0 to τ_7, see Table 9.1). The duration from τ_0 to τ_7 is about 8.8 kyrs and from τ_5 to τ_7 about 1.5 yrs.

Table 9.1: Summary of the time steps used for the demonstration of the onset of the accretion outburst. I emphasize, that these time steps are only valid for a given set of parameters and are only of qualitative nature.

Age	Description
τ_0	MRI inactive deep layer
τ_1	Mass piles up close to the star $\rightarrow H_P \uparrow$
τ_2	T_{gas} starts to rise since the surface heated by $L_\star$ is larger due to the increased H_P
τ_3	A enhanced temperature is attended by expansion $\rightarrow H_P \uparrow \rightarrow T_{gas} \uparrow$ parts of the inner disk reached temperatures close to $T_{active} = 1500$ K
τ_4	$T_{gas} > T_{active}$ in some parts of the disk
τ_5	$\Sigma \uparrow$ as mass is rapidly transported to the inner edge of the disk as the viscosity ν in the former dead zone has increased due to Eq. 5.4.5
τ_6	A run away process (thermal instability) has developed as $\nu \uparrow \rightarrow \dot{M} \uparrow \rightarrow \Sigma \uparrow \rightarrow H_P \uparrow \rightarrow T_{gas} \uparrow \rightarrow \nu \uparrow$
τ_7	The inner regions of the disk where $\Sigma > 100$ g/cm^2 and $T_{gas} > 1500$ K have developed a fully MRI active deep layer

A more detailed description of these results can be found in the Appendix 10.2.

The simulation shows, that the following conditions are important requirements for FU-Ori bursts due to pure MRI and in absence of GIs.

- A region of low viscosity (dead-zone) has to exist in the quiet phase (phase of low accretion rate) of the disk. The temperature in this region is below the critical temperature $T_{active} = 1500$ K for MRI.

- Thermal instabilities cause $T_{gas} > T_{active}$ in this formally viscous inefficient regions results in an outburst phase (phase of enhanced mass flow).

9.1.1 Scale Height

In Figure 9.1 the evolution of the pressure scale height H_P between 0.02 to 0.05 AU at the onset of the burst is described. Initially (Figure 9.1; τ_0; solid, red) the disk is in its quiet phase, where mass is slowly redistributed in direction of the central star. Due to a limited mass transfer efficiency in regions with low viscosity, material piles up in such dead-zones, leading to an increase in H_P (Figure 9.1; τ_1 to τ_2; solid, green to solid, blue). From τ_3 (Figure 9.1; solid, yellow) to τ_4 (Figure 9.1; dashed, red) the temperature in the mid-plane reaches the activation temperature $T_{active} = 1500$ K for MRI. This leads to thermal instability causing an extreme rise in T_{gas} (see Figure 9.2) and thus P_{gas}. This leads to an expansion of the disk causing H_P to rise further (Figure 9.1; τ_5 to τ_7; dashed, green to dashed, yellow). A larger scale height aims a more efficient heating by the star because a larger irradiated surface area is available. Hence, a further rise of T_{gas} happens.
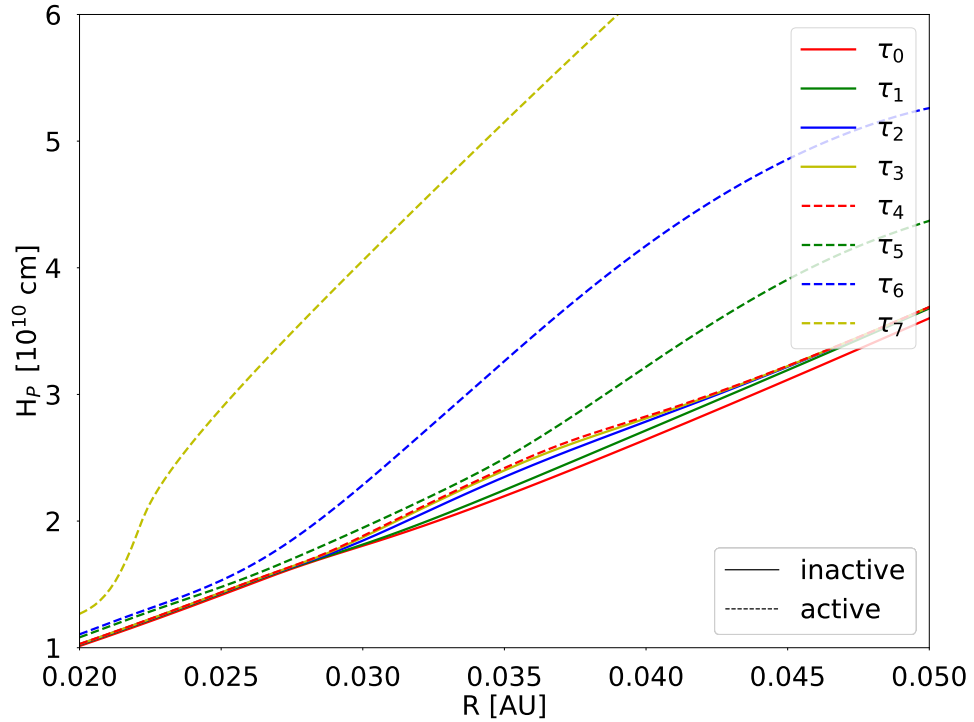

Figure 9.1: Evolution of the pressure scale height H_P between 0.02 to 0.05 AU at the onset of the burst. Solid lines represent models before and dashed lines models after the onset of the thermal instability. The scale height rises as the gas temperature rises. This corresponds to an expansion of the disk in z-direction. Therefore a larger surface irradiated surface area is available, what causes T_{gas} to rise further.

9.1.2   Gas Temperature

In Figure 9.2 the evolution of the gas temperature T_{gas} between 0.02 to 0.05 AU at the onset of the burst is described. Note, that the plot shows only a section of the overall temperature profile. Due to the increase in H_P, the available surface to be irradiated by the star increases and thus formally cold regions are efficiently heated by the star. From τ_3 to τ_4, the gas temperature T_{gas} reaches the activation temperature $T_{active} = 1500$ K for MRI. This leads to thermal instability causing an extreme and fast (the duration between τ_5 and τ_7 is about 1.5 yrs) rise of T_{gas}. Since viscosity is proportional to temperature (see Eq. 3.1.1), a high temperature will lead to a high accretion rate due to a linear sound speed dependence.
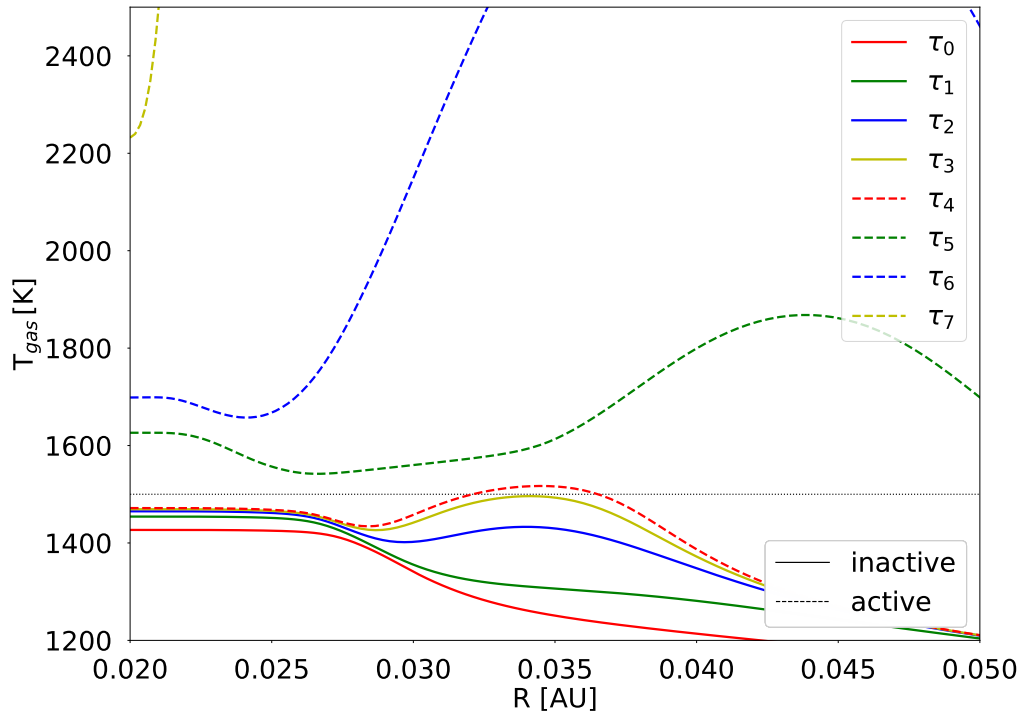

Figure 9.2: Evolution of the gas temperature T_{gas} between 0.02 to 0.05 AU at the onset of the burst. Solid lines represent models before and dashed lines models after the onset of the thermal instability. The vertical line resembles the activation temperature $T_{active} = 1500$ K. The plot shows, that the temperature rises initially slowly within the dead-zone. As T_{gas} exceeds the threshold, the thermal instability sets in. The duration between τ_5 and τ_7 is about 1.5 yrs.

9.1.3 Viscosity

In Figure 9.3 the evolution of the viscosity parameter α (see Eq. 5.4.5) between 0.02 to 0.05 AU at the onset of the burst is pictured. As the gas temperature T_{gas} rises, the deep viscosity does, as described in Section 8.2. If the temperature reaches the activation temperature $T_{active} = 1500$ K for MRI from τ_3 to τ_4, the efficiency of viscosity rapidly increases. Mass accumulates where α has its minima. It is notable, that this minimum shrinks while it moves towards the central star. Hence, the accumulated mass within this minimum of viscosity (dead-zone) is eventually accreted onto the star (see τ_5 to τ_6) as the viscosity rises.
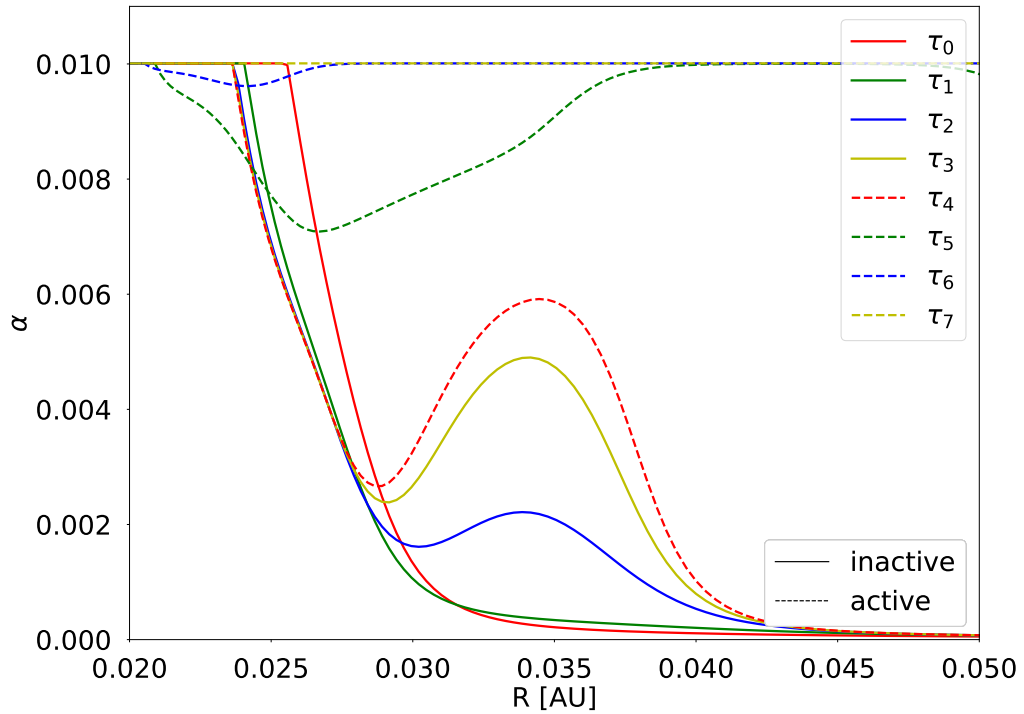
Figure 9.3: Evolution of the viscosity parameter α between 0.02 to 0.05 AU at the onset of the burst. Solid lines represent models before and dashed lines models after the onset of the thermal instability. Mass accumulates where α is minimal. This plot shows, that one minimum shrinks while it moves towards the central star. That can be interpreted as mass that has accumulated within the dead-zone is now efficiently transported towards the star.

9.1.4 Surface Density

In Figure 9.4 the evolution of the surface density Σ between 0.02 to 0.05 AU at the onset of the burst is illustrated. The redistribution of mass in the direction of the star and the development of a deep layer closer to th star can be tracked in this plot. The dotted line resembles the transition between a layered and a non-layered disk. At densities below 100 g/cm^2 (e.g Armitage 2010) no deep layer exists within the disk. As a result of the high accretion rate during the outburst, mass is transported efficiently towards the star, causing an increase of the surface density at small radii (Figure 9.4, τ_0 to τ_3; solid, red to solid, yellow). Although this leads to the development of a deep layer close to the star (Figure 9.4; τ_4 to τ_7; dashed, red to dashed, yellow), high temperatures (see Figure 9.2) however preserve a high viscosity (see Figure 9.3) and thus an efficient mass transfer onto the star.
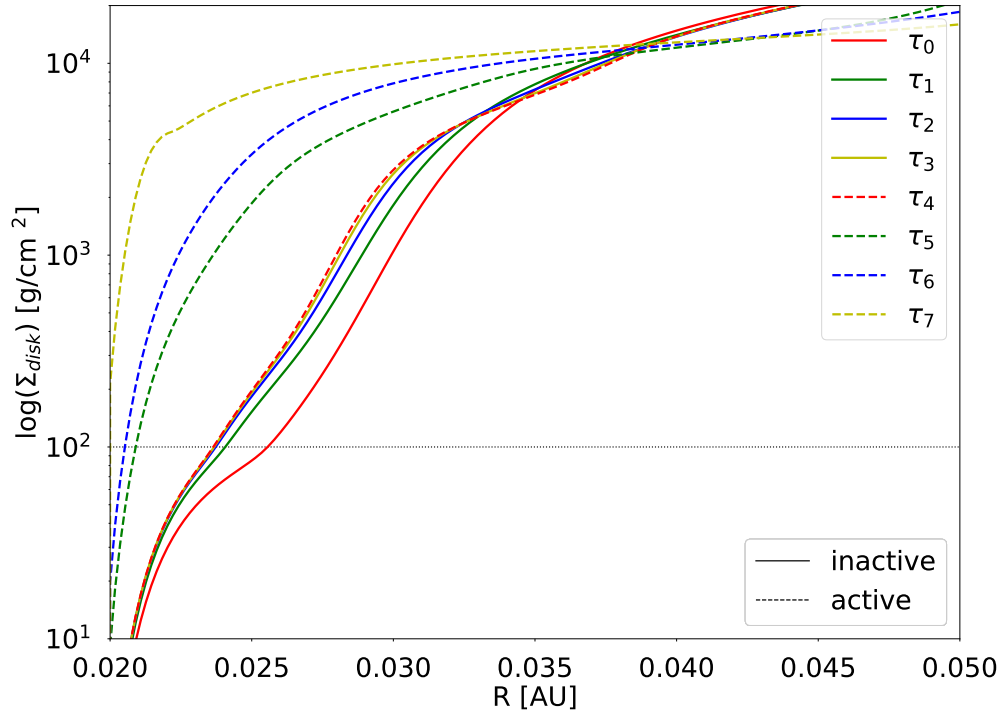
Figure 9.4: Evolution of the surface density Σ between 0.02 to 0.05 AU at the onset of the burst, showing how mass is transported towards the star. Solid lines represent models before and dashed lines models after the onset of the thermal instability. The vertical line resembles 100 g/cm^2, the density value that divides between layered and non-layered disk. This mass transfer results from the increase of viscosity within the dead-zone (see Figure 9.3).

9.2 Eruptive Phase: Disk Evolution

In the previous section the physical process of the onset of the burst was discussed by presenting the evolution of the scale height H_P, surface density Σ, gas temperature T_{gas} and viscosity parameter α. In this section I want to describe the evolution of the disk from the onset of an typical burst (eruptive phase, high accretion rate) until the quiet phase (low accretion rate) is attained again.

For this simulation the same configuration as described in Section 9.1 was adopted (stellar mass $M_\star = 0.1 \ M_\odot$; disk radius from $r = 0.02 - 1.54$ AU; viscosity parameters: $\alpha_{MRI} = 0.01$ for MRI active regions, $\alpha_{GI} = 0.01$ for gravitative unstable regions and $\alpha_{base} = 10^{-5}$ for the base viscosity; no further matter enters the disk over the outer boundary).
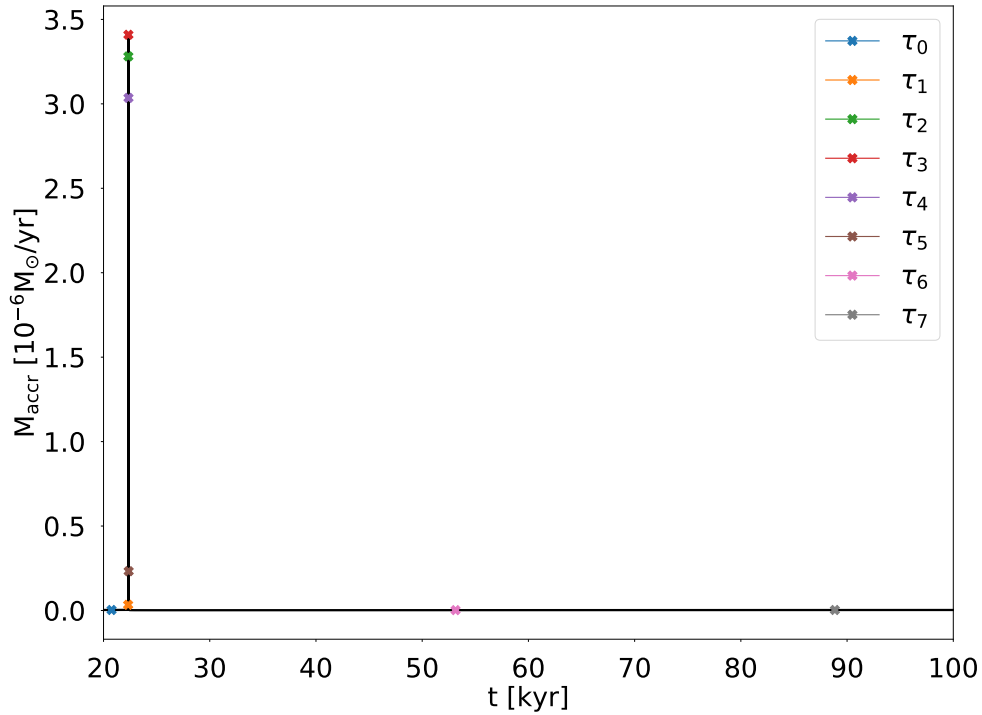

Figure 9.5: This figure shows a typical accretion outburst from the onset of the thermal instability until a stable configuration is obtained again. The y-axis shows the accretion rate onto the star in $10^{-6} M_\odot/yr$, the x-axis shows the time. The duration between τ_0 and τ_1 is about 2.5 kyrs and between τ_1 and τ_6 about 50 yrs. A zoom-in of this burst is presented in Figure 9.6.

Figure 9.5 illustrates an accretion outburst. It shows 8 time-steps (τ_0 to τ_7) where the disk is in the quite phase at τ_0 and τ_7. Figure 9.6 shows a zoom in for the same burst, that represents a detailed evolution. At τ_1 the thermal instability sets in until the maximal temperature of the disk is reached at τ_3 (Figure 9.7; τ_1; solid line, yellow). At this point also the accretion rate M_{accr} has its maximum.
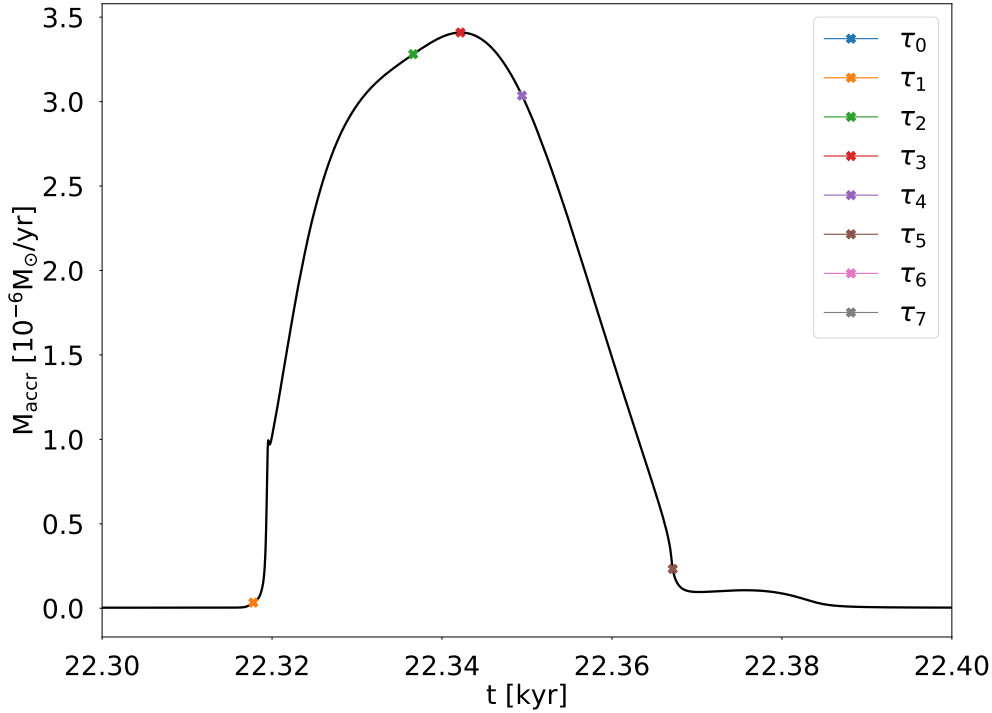
Figure 9.6: This figure illustrates the detailed evolution of the accretion rate onto the star during the accretion outburst showed in Figure 9.5. It shows an steep increase, a plateau like structure and a comparable slow decrease.

The accretion luminousity L_{accr}, and thus the increase in luminousity due to the outburst, is proportional to the accretion rate $M_{accr} = \dot{M}$, utilizing (e.g. Dunham et al. 2014)

$$L_{accr} = f_{accr} \frac{GM_\star M_{accr}}{R} \ , \tag{9.2.1}$$

where $f_{accr} \approx 0.8$ is the accretion efficiency (to consider the fraction of energy that is radiated away in the accretion shock), $M_\star$ is the mass of the protostar and R is the stellar radius.

From τ_4 to τ_7 the accretion rate decreases again until a thermal stable configuration is attained again.

9.2.1   Gas Temperature

Figure 9.7 illustrates the evolution of the temperature for these 8 time steps (see Figure 9.5) from the onset of the thermal instability and the MRI (Figure 9.7; τ_1; solid line, green) until a stable configuration is attained again. The figure shows the outwards propagation of a thermal wave (e.g. visible by following Figure 9.7; τ_2 to τ_5; solid line, blue to dashed line, green). The morphology of the temperature profile in a system with a fast rise in temperature close to the star as well as thermal waves are described by Ragossnig et al. (2019a). After the

eruptive phase a stable temperature profile (Figure 9.7; τ_7; dashed line, yellow), similar to the initial profile, is attained.
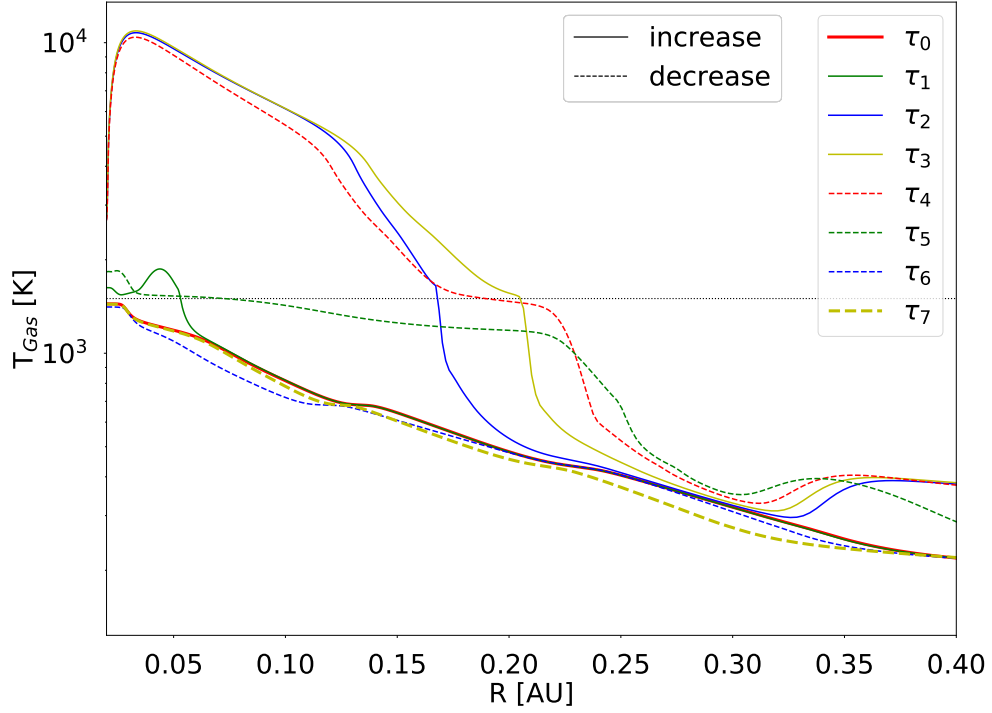

Figure 9.7: This figure shows the evolution of the gas temperature T_{Gas} during the eruptive phase from R = 0.02 − 0.4 AU. Solid lines represent models while the accretion rate is still rising and dashed lines represent models where the accretion rate is declining again. The thermal instability starts at τ_1 until the maximum temperature is reached at τ_3. At this point the instability ends (cf. Audard et al. 2014) and the temperature settles to an profile (τ_7) similar to the initial temperature profile (τ_0). The temperature wave (see τ_2 to τ_5) is described in Ragossnig et al. (2019a).

9.2.2 Surface Density

Figure 9.8 shows the evolution of the surface density for the same 8 time steps and represents the redistribution of matter within the disk. The high accretion rate onto the star results in an fast increase in stellar mass. As described by Ragossnig et al. (2019a), a fast change of stellar mass results in a density wave. The wave emerges close to the star (Figure 9.8; τ_1; solid line, green) propagates radial outwards (Figure 9.8; τ_2 to τ_4; solid line, green to dashed line, red) and pushes material away from the star. After the burst reaches its maximum (Figure 9.8; τ_3; solid line, yellow) the thermal instability ends. The surface density profile (Figure 9.8; τ_4 to τ_7; dashed line, red to dashed line, yellow) settles as expected to a solution representing a lower disk mass than before the outburst.
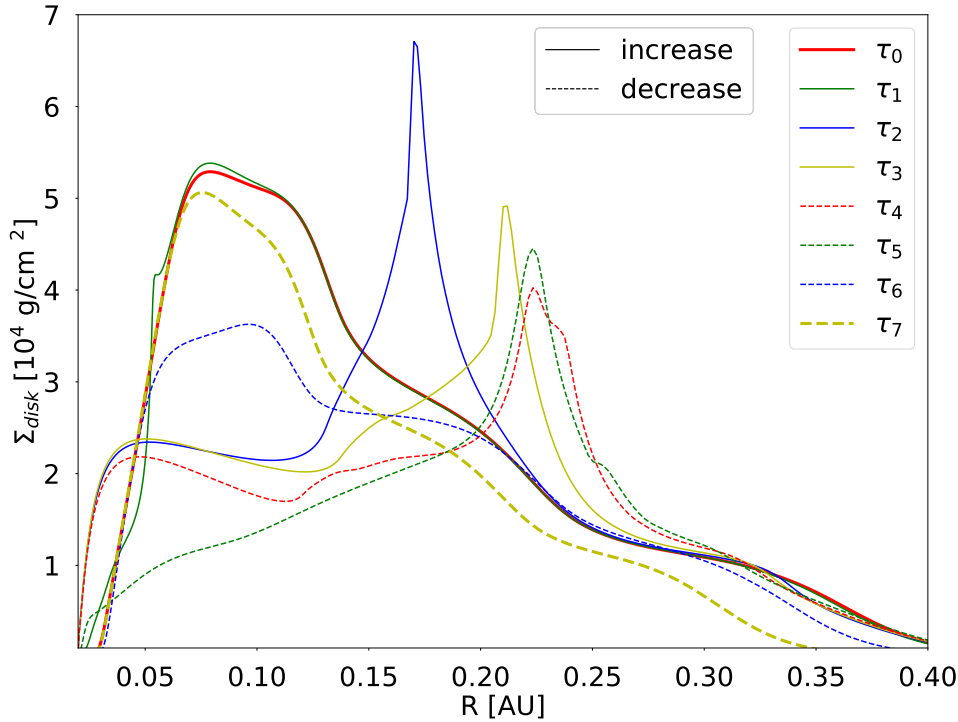
Figure 9.8: This figure shows the evolution of the surface density of the disk Σ_{disk} during the eruptive phase from $R = 0.02 - 0.4$ AU. Solid lines represent models while the accretion rate is still rising and dashed lines represent models where the accretion rate is declining again. This plot shows the redistribution of matter during the eruptive phase. The fast increase of stellar mass results in an outwards propagating density wave (τ_1 to τ_5). After the eruptive phase, the density profile settles to a solution similar to the initial profile but representing a disk with lower mass.

9.3 Global Disk Study: Viscosity Model

The aim of this section is to test the viscosity model, in particular the response of the disk onto a change of the base viscosity α_{base}. This value can also be understood as the viscous transport efficiency within the dead zone of the disk.

9.3.1 Different Dead Zone Viscosities

In this subsection I present the solution of the density profile for 4 different base values of the viscosity α_{base}. This parameter represents the viscosity within the dead-zone. As supposed the density profile of the disk steepens (Figure 9.9a) with decreasing α_{base} as the dead zone gets deeper (= the viscosity decreases, Figure 9.9b). Since the dead-zone is a region within the disk where mass accumulates, a deep dead-zone "holds" more mass locally. Contrary, a high value for for the base viscosity allows for a globally good mass transfer, so the disk density is nearly even distributed over the entire disk.

All models presented in the following section are calculated with a $M_\star = 1.0\,M_\odot$ star and disk masses of $M_{tot} \approx 0.01\,M_\star$. No additional mass enters the disk over the outer boundary. The viscosity parameters for MRI and GI are set to $\alpha_{MRI} = \alpha_{GI} = 0.01$. The disk are gravitational stable over the entire simulation time $(Q > 1.5)$.
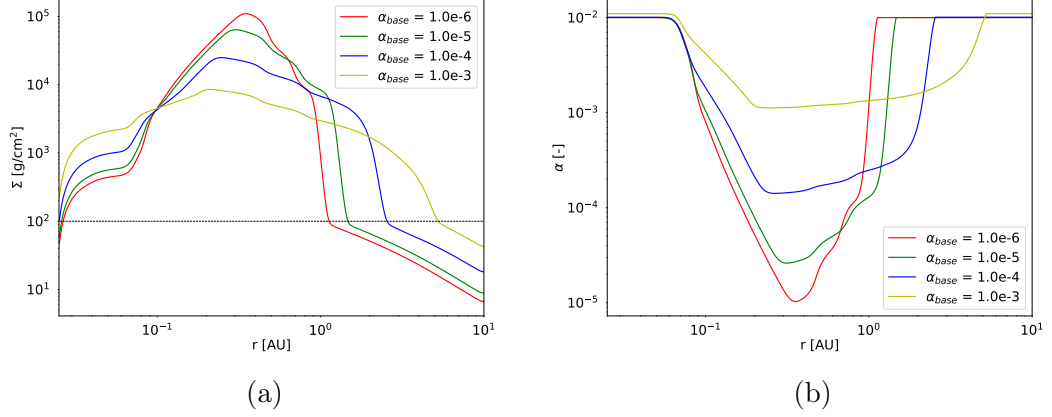
Figure 9.9: (a) Surface density Σ and (b) viscosity parameter α for 4 different values for α_{base}. The horizontal line represents the limit $(100\ \mathrm{g/cm}^2)$ for the development of a deep layer. This figure shows that the density distribution changes with the value of the dead-zone viscosity parameter α_{base}. The density profile broadens with increasing dead-zone viscosity but the maximal density decreases.

9.3.2 Time-Evolution

In this subsection I present the long term evolution of the protostellar disk for two different stars and base viscosity parameters α_{base}. Since a constant viscosity parameter results in no episodic accretion and thus no stellar outbursts, I utilized the viscosity model described in Chapter 8.2. Also viscosity parameters below 10^{-6} do not result in any burst. As expected higher values for the viscosity parameter result in more periodic but less luminous bursts than lower values. Table 9.2 additionally shows stellar masses and viscosity parameters for MRI and GI active regions.

Table 9.2: Values for the study of the viscosity model. The viscosity parameters α_{MRI} and α_{GI} account for mass transport due to magneto-rotational and gravitational instabilities.

Stellar Mass	α_{base}	α_{MRI}	α_{GI}
0.1 M$_\odot$	10^{-5}	0.01	0.01
0.1 M$_\odot$	10^{-4}	0.01	0.01
1.0 M$_\odot$	10^{-5}	0.01	0.01
1.0 M$_\odot$	10^{-4}	0.01	0.01

The accretion rates for FU-Ori objects during outburst are between 10^{-6} and 10^{-4} M$_\odot$ yr^{-1} (Audard et al. 2014, p. 4) and are comparable with the simulation results. Outbursts that show smaller values $\sim 10^{-7}$ M$_\odot$ yr^{-1} belong rather to the family of EX-Ori than FU-Ori objects (Audard et al. 2014).

The following plots represent disks according to Table 9.2, containing masses of 1% of the mass of the host star. The initial disk is always calculated as presented in Section 8.1. No further mass enters the disk during the simulation. Each figure consists of (a) the evolution of the accretion rate during the entire lifetime of the disk and (b) a zoom-in of an arbitrary burst where "onset" represents the (approximate) start of the thermal instability (see Section 9.1) and "offset" represents the (approximate) moment where the disk entered the quiescent phase. The zoom-in shows that the sequence of the burst strongly depends on the dead-zone viscosity. This seems comprehensible since the material, that accumulates within the dead zone, is released onto the star during the outburst.

Although the details of the morphology of the burst structure is still under investigation, I emphasize, that the dead-zone viscosity is primary responsible for structure and periodicity of the accretion outbursts. A more effective viscosity results in a higher outburst rate but a lower luminousity and the structure appears more detailed. Additionally, I note, that a higher temporal and spacial resolution is necessary to show the distinct burst structure.

Low-mass Star

The mass of the star is set to 0.1 M$_\odot$. The disk contains 1% of the stellar mass. The structure of the burst shows a steep rise in the accretion rate, that remains in an elevated state, which typically lasts according to observations for

several decades (Audard et al. 2014). For the selected parameters, two maxima in the accretion rate and thus in the luminousity are visible. The duration of the eruptive phase is about 100 yrs. As expected a higher viscosity (larger value of α) aims a higher periodicity and lower luminousity. Additionally the burst behavior of a low-mass stars shows less bursts compared to as solar like star. However, this is is due to the more massive disk around the solar-like star (each disk contains 1% of the stellar mass). If the disk is depleted, it has no more mass to produce accretion outbursts anymore.
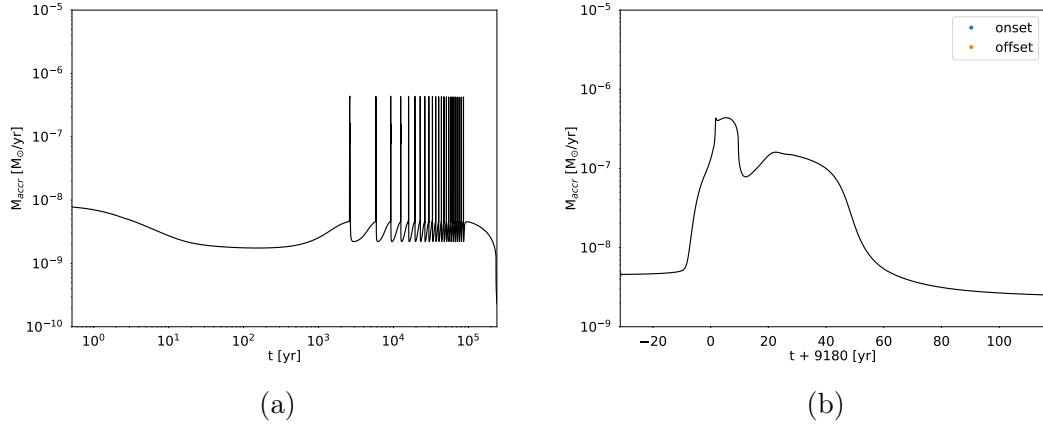

Figure 9.10: (a) Entire lifetime of the disk: evolution of the accretion rate for $M_\star = 0.1 M_\odot$ and $\alpha_{base} = 10^{-4}$. (b) Zoom in to show the detailed morphology of a typical burst. In this plot "onset" represents the (approximate) start of the thermal instability (see Section 9.1) and "offset" represents the (approximate) moment where the disk entered the quiescent phase. The accretion rate rises from about 5.0×10^{-9} to $5.0 \times 10^{-7} M_\odot/\text{yr}$.

Figure 9.11: (a) Entire lifetime of the disk: evolution of the accretion rate for $M_\star = 0.1 M_\odot$ and $\alpha_{base} = 10^{-5}$. (b) Zoom in to show the detailed morphology of a typical burst. The accretion rate rises from about 3.0×10^{-9} to $3.0 \times 10^{-6} M_\odot/\text{yr}$.

Solar-like Star

The mass of the star is now set to 1.0 $M_\odot$, again surrounded by a disk with 0.01 $M_\star$. The structure of the burst shows a steep rise in the accretion rate. For the selected parameters, several maxima in the accretion rate and thus in the luminousity are visible. I emphasize, that the presented structure of a single burst is biased due to a low resolution and should rather show differentiated high-frequency bursts. The duration of the eruptive phase is about 1 kyr. As expected a higher viscosity (larger value of α) aims a higher periodicity and lower luminousity.

(a)   (b)

Figure 9.12: (a) Entire lifetime of the disk: evolution of the accretion rate for $M_\star = 1.0$ $M_\odot$ and $\alpha_{base} = 10^{-4}$ (the simulation is not complete due to an computer error). (b) Zoom in to show the detailed morphology of a typical burst. The accretion rate rises from about 4.0×10^{-9} to $5.0 \times 10^{-7} M_\odot$/yr.
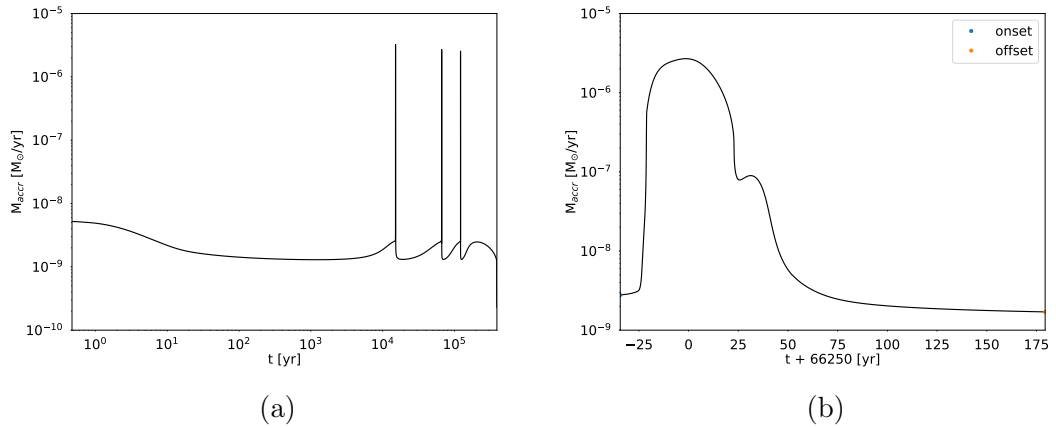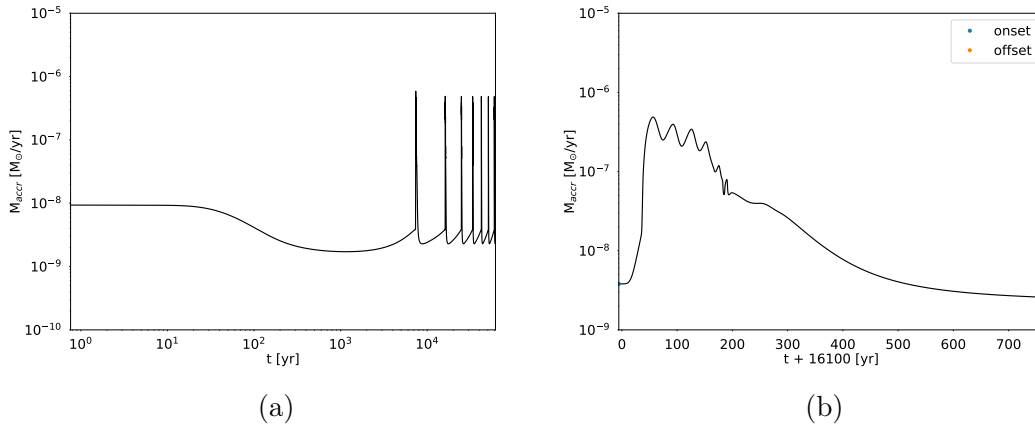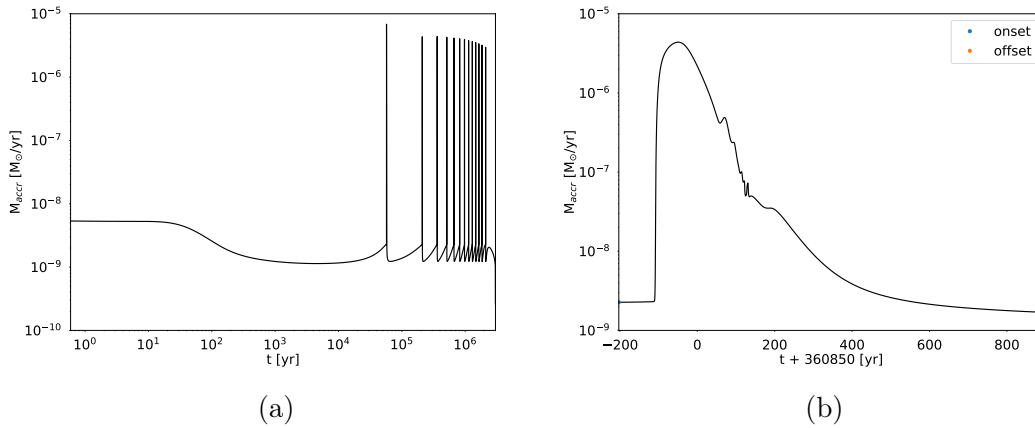

(a)   (b)

Figure 9.13: (a) Entire lifetime of the disk: evolution of the accretion rate for $M_\star = 1.0 M_\odot$ and $\alpha_{base} = 10^{-5}$. (b) Zoom in to show the detailed morphology of a typical burst. The accretion rate rises from about 2.0×10^{-9} to $7.0 \times 10^{-6} M_\odot$/yr.

9.4 Comparison with Observation

The outburst of the classical T Tauri star V 2493 Cyg (HBC 722) happened in summer 2010 and was observed in a wide spectral range (e.g. Semkov et al. 2012). After reaching its first maximum in October 2010, the objects brightness starts to weaken slowly until a new light increase occurred in 2011.

In this section I present a comparison of the observational data of V 2493 Cyg (see Figure 9.14) with a snapshot of the time evolution of a $M_\star = 0.1$ $M_\odot$ star and a base disc viscosity parameter $\alpha_{base} = 10^{-4}$ (see Figure 9.15).
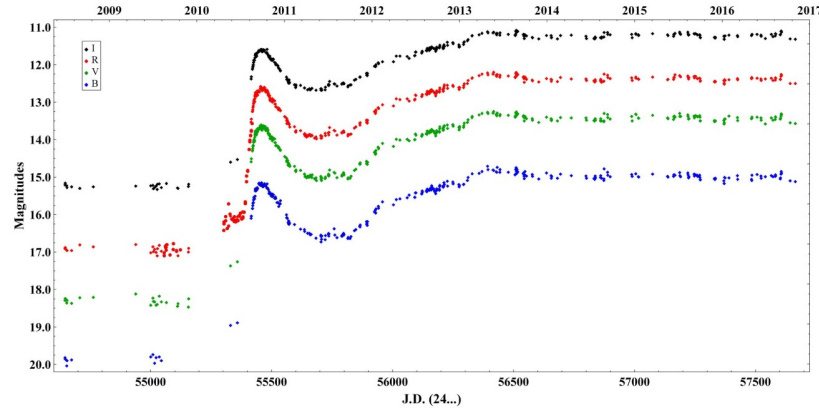

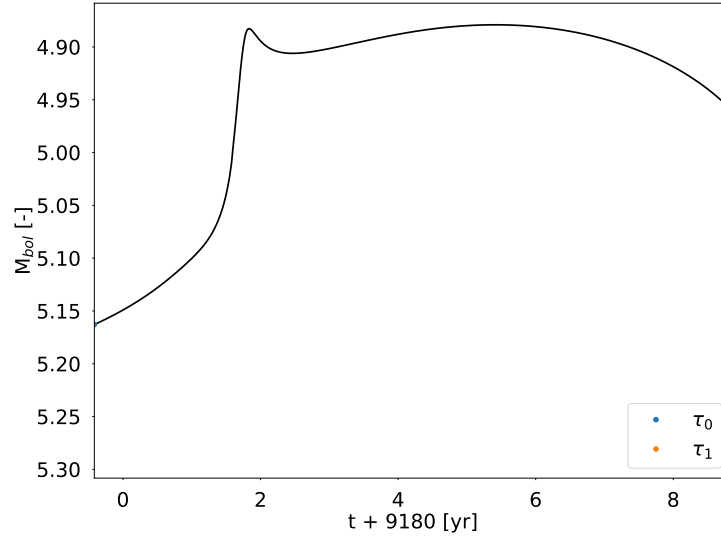Figure 9.14: Observational data of V 2493 Cyg (HBC 722) (Semkov et al. 2014)

Figure 9.15: Section of Figure 9.10a to show comparability between observation and simulation ($M_\star = 0.1 M_\odot$ and $\alpha_{base} = 10^{-4}$).

The magnitude is calculated by the relationship to luminosity given by

$$M_{bol} = -2.5 \log_{10} \frac{L_\star}{L_0} , \qquad (9.4.1)$$

where $L_0 = 3.0128\,10^{28}$ W (Mamajek et al. 2015) is defined as the zero point luminosity. Although the differences of the magnitude between quiet and burst phase is not comparable, the general morphology and duration are similar. Similar to the observational data, presented in Figure 9.14, the luminosity rises to its first maximum, and weakens slowly. After about 1 yr the luminosity increases again and remains on this level for ~ 4 yrs. A more detailed comparison will be given in an accompanying publication.

9.5 Discussion

In this thesis I have presented 1+1D simulations of the long term evolution of viscous protostellar disks. Although the 1D restriction is a simplification of this problem, it is sufficient to simulate the inner regions of the disk as described in Chapter 8. The aim is to demonstrate, that the occurrence of accretion outburst due to thermal instabilities is highly coupled with the viscosity model. This presuppose the existence of regions of low viscosity (dead zones) within the disk. I showed that adopting the layered disk model leads to episodic accretion events for comparatively low-mass disks without the occurrence of gravitational instabilities.

The results are in good agreement with observational data (Semkov et al. 2014). Since, the outburst behavior strongly depends on the inner boundary, I emphasize that a consistent treatment of the inner region of the disk is necessary. This finding is supported by Bae et al. (2013) who suggests that for an appropriate investigation of the detailed time evolution of an accretion burst the regions below r < 0.5 AU have to be included in the model.

Moreover, one can see that the viscosity parameter α (low α's represent less effective viscosity and vice versa) effects the periodic accretion frequency. A more effective viscosity results in a higher outburst but a lower luminousity (see Section 9.3.2). Additionally with higher viscosity the burst structure appears more detailed. This is still under debate and will be subject to further investigations.

The influence of the gravitational potential of the disk (see Ragossnig et al. 2019a) on accretion outburst has already been tested and showed only a time shift for the onset of the burst. Additionally, I aim to present simulation results that include the adaptive grid and higher time resolution in accompanying publications. Maybe they will help to understand how the accretion outburst are related to the disk structure. Moreover, I want to show the impact of different boundary condition as well as different stellar parameters.

It is still important to improve the numerical implementation of the boundary conditions and the connection between star and disk. A possible method is including stellar magnetic fields to determine the position of the inner boundary and to simulate magentospheric boundary accretion.

The TAPIR Code for disks and the simulation results provide new insights in the evolution of protoplanetary disks. However, it is necessary to extend the

code from 1+1D to two spatial dimensions to calculate more consistently the physical nature of these disk instabilities.

Chapter 10

Appendix

10.1 Auxiliary Calculation

10.1.1 Numerical advantages of the conservative form

The advantage in computational physics can be shown with an easy example. Imagine the conservative form of the partial derivative of $f\,g$ where $f = f(t, x)$ and $g = g(t, x)$ in one dimension.

$$\frac{\partial}{\partial x}(fg) \tag{10.1.1}$$

If discretizing this derivative in a simple numerical way, the following expression is obtained.

$$\frac{\partial}{\partial x}(fg) \approx \frac{(fg)_i - (fg)_{i-1}}{\Delta x} \tag{10.1.2}$$

On the other hand, the non-conservative form

$$f\frac{\partial g}{\partial x} + g\frac{\partial f}{\partial x} \tag{10.1.3}$$

can be discretized as follows

$$f\frac{\partial g}{\partial x} + g\frac{\partial f}{\partial x} \approx f_i\frac{g_i - g_{i-1}}{\Delta x} + g_i\frac{f_i - f_{i-1}}{\Delta x}\,. \tag{10.1.4}$$

Obviously both differentials are mathematically equal, but the discretized forms are not equal. In conservative form, as the name says, the quantity advected through a numerical grid has to be conserved. That means that a flux that enters one side, leaves the other side and everything that happens in between these boundaries has to be negligible. Mathematically a conservative derivative thus has to form a so called telescoping series. According to that, each term a_k of a series can be written as $a_k = b_k - b_{k-1}$ for $k = 1, 2, 3, ..., n$ and the sum

$$a_1 + a_2 + a_3 + ... + a_n = (b_1 - b_0) + (b_2 - b_1) + (b_3 - b_2) + ... + (b_n - b_{n-1}) = b_n - b_0\,, \tag{10.1.5}$$

is only dependent on the boundary values. If using an e.g. 4 point grid $k = 0, 1, 2, 3$ the conservative form expands as follows.

$$\frac{(fg)_1 - (fg)_0}{\Delta x} + \frac{(fg)_2 - (fg)_1}{\Delta x} + \frac{(fg)_3 - (fg)_2}{\Delta x} = \frac{(fg)_3 - (fg)_0}{\Delta x} \tag{10.1.6}$$

Clearly the internal points ($i = 1$ and $i = 2$) have canceled out. Looking at the non-conservative form

$$f_1 \frac{g_1 - g_0}{\Delta x} + g_1 \frac{f_1 - f_0}{\Delta x} + f_2 \frac{g_2 - g_1}{\Delta x} + g_2 \frac{f_2 - f_1}{\Delta x} + f_3 \frac{g_3 - g_2}{\Delta x} + g_3 \frac{f_3 - f_2}{\Delta x}, \quad (10.1.7)$$

shows, that such a canceling of terms is not possible - in contrary: the number of terms grows with the number of grid-points. Physically spoken, the incoming flux doesn't balance the outgoing flow - the equation is not conservative.

10.1.2   Momentum Equation

Starting with the **equation of momentum** in non-conservative (convective)

$$\rho \frac{D\mathbf{u}}{Dt} + \nabla \cdot P = \rho \left[\partial_t \mathbf{u} + (\mathbf{u} \cdot \nabla)\mathbf{u} \right] + \nabla P = 0, \quad (10.1.8)$$

and adding other external forces e.g. gravitational forces and viscosity to the conservation of momentum, the **Cauchy momentum equation**

$$\rho \left[\frac{\partial \mathbf{u}}{\partial t} + (\mathbf{u} \cdot \nabla)\mathbf{u} \right] = -\nabla P + \nabla \cdot \underline{\underline{\tau}} + \rho \mathbf{g} = \nabla \cdot \underline{\underline{\sigma}} + \rho \mathbf{g}, \quad (10.1.9)$$

is attain. The deviatoric stress tensor $\underline{\underline{\tau}}$ can be expressed by using the total Cauchy stress tensor $\underline{\underline{\sigma}}$ for a moving fluid as follows.

$$\tau_{ij} = P\delta_{ij} + \sigma_{ij} \quad (10.1.10)$$

The general form of the conservation of momentum is the Navier-Stokes momentum equation. To write this equation we write the viscous stress tensor as

$$\tau_{ij} = \mu_Q \left(\frac{\partial u_i}{\partial x_j} + \frac{\partial u_j}{\partial x_i} - \frac{2}{3}\delta_{ij} \frac{\partial u_k}{\partial x_k} \right) + \xi\delta_{ij} \frac{\partial u_k}{\partial x_k} \quad (10.1.11)$$

in literature often found in index notation or otherwise as follows.

$$\underline{\underline{\tau}} = \underbrace{\mu_Q \left[\nabla\mathbf{u} + (\nabla\mathbf{u})^T - \frac{2}{3}(\nabla \cdot \mathbf{u})\,\mathbb{1} \right]}_{\text{shear viscosity}} + \underbrace{\xi(\nabla \cdot \mathbf{u})\,\mathbb{1}}_{\text{bulk viscosity}} \quad (10.1.12)$$

The first part of the equation denotes for the shear stress where $\mu_Q = \rho\nu$ is the dynamic viscosity and the other part for the second viscosity (or bulk viscosity) - but this is rarely used in astronomy. The factor $\frac{2}{3}$ was found by Stokes and takes care, that the part containing the shear stress vanishes for self similar flows (means a flow whose shape doesn't change in time e.g. a spherical expansion, $\mathbf{u} = \mathbf{x}\,k$ for $k = $ const.) and $\mathbb{1}$ is the uniform tensor. Substituting this expression into the Cauchy momentum equation gives

$$\rho \left[\frac{\partial \mathbf{u}}{\partial t} + \underbrace{(\mathbf{u} \cdot \nabla)\mathbf{u}}_{\text{convection}} \right] = -\nabla P + \left(\frac{1}{3}\mu_Q + \xi \right) \nabla(\nabla \cdot \mathbf{u}) + \underbrace{\mu_Q \nabla^2 \mathbf{u}}_{\text{diffusion}} + \underbrace{\rho\mathbf{g}}_{\text{external source}}$$

$$(10.1.13)$$

the **Navier-Stokes momentum equation**. For incompressible fluids where changes in pressure and temperature stay constant along a line of flow, all terms with $\nabla \cdot \mathbf{u}$ vanish. This certainty arises by writing the equation of continuity Eq. 4.4.5 in Lagrangian (material) derivative

$$\partial_t \rho + \nabla \cdot (\rho \mathbf{u}) = \underbrace{\partial_t \rho + \mathbf{u} \cdot \nabla \rho}_{\frac{D\rho}{Dt}} + (\rho \nabla) \mathbf{u} = 0 \tag{10.1.14}$$

what shows that

$$\frac{D\rho}{Dt} = -(\rho \nabla) \mathbf{u} \tag{10.1.15}$$

If $\nabla \cdot \mathbf{u} \neq 0$ applies, the density would change in time what is attended by a change of mass in the constant control volume, a compression or expansion of the fluid. Since this is prohibited for incompressible flows, the material derivative of the density and thus the divergence of the velocity has to vanish for non-zero density values. This leaves the following equation.

$$\rho \left[\frac{\partial \mathbf{u}}{\partial t} + (\mathbf{u} \cdot \nabla) \mathbf{u} \right] = -\nabla P + \rho \nu \nabla^2 \mathbf{u} + \rho \mathbf{g} \tag{10.1.16}$$

10.1.3 Energy Equation

For the conservation of energy the total specific energy of the system is assumed to consist only of the thermal specific energy e_{th} and the kinetic specific energy $e_{kin} = |\mathbf{u}|^2/2$.

$$e_{tot} = \rho \left(e_{th} + \frac{|\mathbf{u}|^2}{2} \right) \tag{10.1.17}$$

Since $e_{tot} = $ const. the temporal change in a closed control volume is zero.

$$\partial_t e_{tot} = \partial_t \left(\rho e_{th} + \rho \frac{|\mathbf{u}|^2}{2} \right) = 0 \tag{10.1.18}$$

Using the specific enthalpy $h = e + \frac{P}{\rho}$, the first law of thermodynamic (in specific values) $de = Tds - Pdv$ (with v as the specific volume) with $dv = d(\frac{1}{\rho}) = -\frac{1}{\rho^2}d\rho$, the fact that $\frac{ds}{dt} = 0$ (conservation of entropy) the equations of continuity, motion and some algebra the **equation of energy** is obtained.

$$\partial_t \underbrace{\left(\rho e_{th} + \rho \frac{|\mathbf{u}|^2}{2} \right)}_{\text{total energy density}} + \nabla \cdot \underbrace{\left[\rho \mathbf{u} \left(\frac{|\mathbf{u}|^2}{2} + h \right) \right]}_{\text{energy flux density}} = 0 \tag{10.1.19}$$

This equation can again be simplified by substituting the specific enthalpy and the total energy $e_{tot} = e$.

$$\partial_t(\rho e) + \nabla \cdot (\rho \mathbf{u} e) + \nabla \cdot (P\mathbf{u}) = 0 \tag{10.1.20}$$

This is a conservative form of the inviscid equation of energy. If viscosity is included into the equation of state, a viscous force is exerted onto the fluid, acting against the fluid flow, and a viscous work is done. Thus the equation of

energy has to be modified in a way that this energy dissipation is considered. In this case kinetic energy is transformed to heat that contributes to the total energy due to friction and viscosity.

$$\partial_t(\rho e) + \nabla \cdot (\rho \mathbf{u} e) + \nabla \cdot (P\mathbf{u}) + \underbrace{\nabla \cdot \left(\underline{\underline{Q}}\mathbf{u}\right)}_{\text{viscosity}} + \underbrace{\nabla \cdot \mathbf{q}}_{\text{diffusion}} = 0 \qquad (10.1.21)$$

Here $\mathbf{q} = -D\nabla T$ is heat due to diffusion where D is the diffusion or conduction coefficient. To calculate the inner energy, the equation of motion times $\mathbf{u}$ is subtracted from the total energy. To achieve this Eq. 4.5.9 is used and the gravitation term is dropped. This leaves

$$\partial_t(\rho e) + \nabla \cdot (\rho \mathbf{u} e) + P\nabla \cdot \mathbf{u} + \underline{\underline{Q}} : \nabla \mathbf{u} + \nabla \cdot \mathbf{q} = 0 \qquad (10.1.22)$$

If considering radiation transport this equation is extended to

$$\partial_t(\rho e) + \nabla \cdot (\rho \mathbf{u} e) + P\nabla \cdot \mathbf{u} + \underline{\underline{Q}} : \nabla \mathbf{u} + \nabla \cdot \mathbf{q} - 4\pi\rho\kappa (J - S) = 0. \qquad (10.1.23)$$

10.1.4   Mid-plane density

Substituting $z = \sqrt{2}\,H\,u \rightarrow \mathrm{d}z = \sqrt{2}\,H\,\mathrm{d}u$, the integral in Eq. 5.5.11 can be rewritten as follows.

$$\int_{-\infty}^{+\infty} \rho_0 e^{-\frac{z^2}{2H^2}}\,\mathrm{d}z \Rightarrow \sqrt{2}\,H\,\rho_0 \int_{-\infty}^{+\infty} e^{-u^2}\,\mathrm{d}u = \sqrt{2}\,H\,\rho_0 \underbrace{\frac{\sqrt{\pi}}{2}\mathrm{erf}(u)\Big|_{-\infty}^{+\infty}}_{\text{solution of the integral}}$$

Since the $\mathrm{erf}(\infty) = 1$ and the error function is an odd function $\mathrm{erf}(-x) = -\mathrm{erf}(x)$, $\mathrm{erf}(-\infty) = -1$ what aims:

$$\frac{\sqrt{\pi}}{2}\underbrace{\mathrm{erf}(u)\Big|_{-\infty}^{+\infty}}_{=\,2} = \sqrt{\pi} \qquad (10.1.24)$$

10.1.5   Equation of Continuity - Protoplanetary Disk

The following equation in Section 5.3.1 (e.g. Pringle 1981)

$$\frac{\delta}{\delta t}\left(2\pi r\,\Delta r\Sigma(r,t)\right) = 2\pi r\,\Sigma(r,t)v_r(r,t) - 2\pi(r+\Delta r)\,\Sigma(r+\Delta r,t)v_r(r+\Delta r,t) \qquad (10.1.25)$$

can be simplified by a first order Taylor expansion for $\Sigma(r+\Delta r,t)$ and $v_r(r+\Delta r,t)$ at small δt

$$v_r(r+\Delta r) = v_r(r) + \frac{\partial v_r}{\partial r}\Delta r \qquad (10.1.26)$$

$$\Sigma(r+\Delta r) = \Sigma(r) + \frac{\partial \Sigma}{\partial r}\Delta r \qquad (10.1.27)$$

This aims

$$\delta m = -2\pi\Delta r\left(\frac{\partial v_r}{\partial r}\Sigma r + \Sigma v_r + \frac{\partial \Sigma}{\partial r}rv_r\right)\delta t \qquad (10.1.28)$$

$$\underbrace{\frac{\delta m}{\delta t}}_{\text{①}} = -2\pi\Delta r \underbrace{\left(\frac{\partial v_r}{\partial r}\Sigma r + \Sigma v_r + \frac{\partial \Sigma}{\partial r}r v_r\right)}_{\text{②}} \qquad (10.1.29)$$

Using the following assumptions and simplifications

- The total mass in an annuli is $m = 2\pi r \Delta r \Sigma$.

- At small time-steps δt we can change $\frac{\delta m}{\delta t} \to \frac{\partial m}{\partial t}$.

- So ① can be written as

$\frac{\delta m}{\delta t} = \frac{\partial m}{\partial t} = 2\pi r \Delta r \frac{\partial \Sigma}{\partial t}$

and the chain rule for derivatives aims the following expression for ②.

$\frac{\partial v_r}{\partial r}\Sigma r + \Sigma v_r + \frac{\partial \Sigma}{\partial r}r v_r = \frac{\partial v_r}{\partial r}\Sigma r + \frac{\partial r}{\partial r}\Sigma v_r + \frac{\partial \Sigma}{\partial r}r v_r = \frac{\partial}{\partial r}\Sigma v_r r$

10.2 Burst Onset in Detail

Initially (τ_0) there is no distinct MRI active deep layer within the disk. This is characterized by an exiguous value for the deep viscosity parameter α_{deep} (Figure 10.1e). Due to accretion, mass continuously flows in the direction of the star. The efficiency of the transport is limited by a viscous time scale t_ν defined by Eq. 5.5.21. A low viscosity ν yields a higher t_ν and thus an inefficient mass transport $\dot{M}$ also seen in Eq. 5.5.20. Hence, mass accumulates at these regions in the disk and piles up resulting in an increase of the pressure scale height H_P (τ_1) see Figure 10.1a. As H_P increases, a larger surface is illuminated by the star and initially colder regions start to heat up. This leads to an increase of the gas temperature T_{gas} (τ_2). The rising temperature leads to an expansion of the disk and thus again to a rising H_P and thus T_{gas} increases further. Parts of the inner disk gain temperatures close to the MRI activation temperature $T_{\text{active}} = 1500$ K (Fig 10.1c, dotted line), where gas is ionized and magnetic field lines couple to the disk (τ_3). Eventually $T_{\text{gas}} > T_{\text{active}}$ (Fig 10.1c) in some parts of the inner disk (τ_4). Since ν rises direct proportional with temperature and scale height, regions with initial inefficient mass transport now exhibit an enhanced mass flux. Mass, that accumulated in the former dead zone, now is efficiently transported closer to the star, again resulting in and rising H_P and T_{gas} (τ_5). The inner disk enters a runaway process (thermal instability) as the temperature rises and most parts of the inner disk reach $\alpha \approx 0.01$, the maximum value for α in this simulation of a gravitational stable disk (τ_6). The overall viscosity α remains at its maximum value (τ_7) until the dead zone is depleted and the burst is over.

(a) H_P

(b) Σ

(c) T_{gas}

(d) α

(e) α_{deep}

(f) α_{surf}

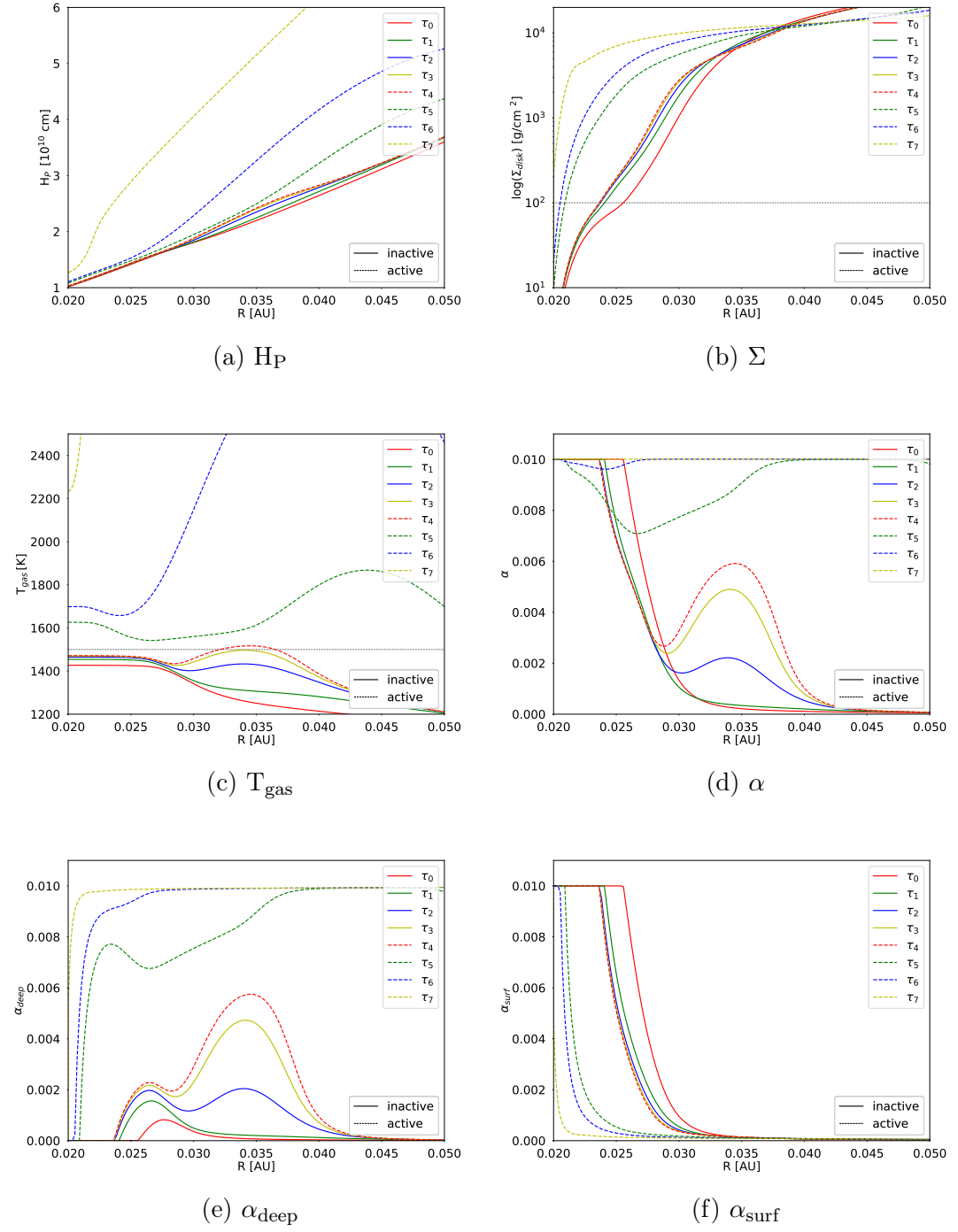Figure 10.1: Series of important parameters that represent the onset of a burst. Solid lines represent an MRI inactive protoplanetary disk, while dashed lines represent a MRI active disk. The models τ_3 and τ_4 represent the transition between an MRI inactive and active deep layer. This is best seen in 10.1c as the gas temperature exceeds the critical temperature and a thermal instability sets in.

10.3 Notation

Table 10.1

α	unit-less viscosity parameter (Shakura & Sunyaev 1973)	$-$
c_S	sound speed	$\mathrm{ms}^{-}1$
E_{kin}, T	kinetic energy	J
E_{pot}, U	potential energy	J
f	degree of freedom	$-$
G	gravitational constant	$6.674\,10^{-11}\mathrm{N\,kg}^{-2}\,\mathrm{m}^2$
Γ_1	first adiabatic index	$-$
H_P	pressure scale height	m
k	Boltzmann's constant	$1.381\,10^{-23}\mathrm{JK}^{-1}$
l_r	radial momentum	$\mathrm{kg\,ms}^{-1}$
l_ϕ	angular momentum	$\mathrm{kg\,m}^2\mathrm{s}^{-1}$
L	luminosity (in general)	W
L_{rad}	radiation luminosity	W
L_{surf}	surface luminosity	W
$L_\odot$	solar luminosity	$3.828\,10^{26}\mathrm{W}$
$\Lambda(T)$	cooling function	$\mathrm{Jm}^3\mathrm{s}^{-1}$
M, m	integrated mass	kg
M_J	Jeans mass	kg
$M_\odot$	solar mass	$1.989\,10^{30}\mathrm{kg}$
$M_\star$	stellar mass	kg
M_{mol}	molar mass	$\mathrm{kg\,mol}^{-1}$
m_H	hydrogen atom mass	kg
$\bar{m}$	average mass per particle	kg
μ	unit-less mean molecular weight	$-$
μ_Q	dynamic viscosity	$\mathrm{kg\,m}^{-1}\mathrm{s}^{-1}$
n	number density	m^{-3}
n_{mol}	amount of substance	mol
N	number of particles in a system	$-$
N_A	Avogadro constant	$6.022\,10^{23}\mathrm{mol}^{-1}$
∇_{rad}	radiative temperature gradient	$-$
∇_{ad}	adiabatic gradient, convection if $\nabla_{rad} > \nabla_{ad}$	$-$
ν	kinematic viscosity	$\mathrm{m}^2\mathrm{s}^{-1}$

Table 10.2

P	pressure	Pa
R	integrated radius	m
$R_\odot$	solar radius	$6.957\,10^8$m
$R_\star$	stellar radius	m
r_{co}	co-rotation radius	m
ρ	mass density	kg m^{-3}
σ_{SB}	Stefan Boltzmann's constant	$5.670\,10^{-8}\text{W m}^{-2}\,\text{K}^{-4}$
Σ	surface/column deńsity	kg m^{-2}
T	Temperature	K
τ_c	cooling timescale	s
τ_{ff}	free-fall timescale	s
τ_{KH}	Kelvin-Helmholtz timescale	s
$u_\phi,\ v_\phi$	toroidal velocity	ms^{-1}
$u_r,\ v_r$	radial velocity	ms^{-1}
$u_K,\ v_K$	Keplarian velocity	ms^{-1}
Ω	orbital frequency	s^{-1}

Bibliography

Armitage, P. J. 2010, Astrophysics of Planet Formation (University of Colorado, Boulder)

Armitage, P. J. 2011, ARAA, 49, 195

Armitage, P. J. 2011, Annual Review of Astronomy and Astrophysics, 49, 195

Armitage, P. J. 2015, arXiv e-prints, arXiv:1509.06382

Armitage, P. J., Livio, M., & Pringle, J. E. 2001, MNRAS, 324, 705

Audard, M., Ábrahám, P., Dunham, M. M., et al. 2014, Protostars and Planets VI, 387

Bae, J., Hartmann, L., Zhu, Z., & Gammie, C. 2013, ApJ, 764, 141

Balbus, S. A. & Hawley, J. F. 1991, ApJ, 376, 214

Bate, M. R. 2011, Monthly Notices of the Royal Astronomical Society, 417, 2036

Bath, G. T. & Pringle, J. E. 1981, MNRAS, 194, 967

Bell, K. R. & Lin, D. N. C. 1994, ApJ, 427, 987

Beuther, H., Klessen, R. S., Dullemond, C. P., & Henning, T. 2014, Protostars and Planets VI

Boss, A. P. & Hartmann, L. W. 2001, ApJ, 562, 842

Calvet, N., Hartmann, L., & Strom, S. E. 2000, Protostars and Planets IV, 377

Canuto, V. M., Goldman, I., & Hubickyj, O. 1984, ApJ, 280, L55

Chabrier, G., Baraffe, I., Allard, F., & P., H. 2000, ApJ, 542, 119

Chandrasekhar, S. 1960, Proceedings of the National Academy of Science, 46, 253

Clausius, R. 1870, Annalen der Physik, 217, 124

Desch, S. J. & Turner, N. J. 2015, The Astrophysical Journal, 811, 156

DeSouza, A. L. & Basu, S. 2017, NA, 51, 113

Dominik, C. 2015, in European Physical Journal Web of Conferences, Vol. 102, European Physical Journal Web of Conferences, 00002

Dorfi, E. A. & Drury, L. O. 1987, Journal of Computational Physics, 69, 175

Dunham, M. M., Stutz, A. M., Allen, L. E., et al. 2014, in Protostars and Planets VI, ed. H. Beuther, R. S. Klessen, C. P. Dullemond, & T. Henning, 195

Flock, M., Fromang, S., Turner, N. J., & Benisty, M. 2016, ApJ, 827, 144

Gammie, C. F. 1996, ApJ, 457, 355

Goodwin, S. P., Kroupa, P., Goodman, A., & Burkert, A. 2007, Protostars and Planets V, 133

Hartmann, L. & Bae, J. 2018, MNRAS, 474, 88

Hartmann, L., Calvet, N., Gullbring, E., & D'Alessio, P. 1998, ApJ, 495, 385

Hartmann, L., Herczeg, G., & Calvet1, N. 2016, ARAA, 53, 135

Hartmann, L. & Kenyon, S. J. 1996, Annual Review of Astronomy and Astrophysics, 34, 207

Hartmann, L., Zhu, Z., & Calvet, N. 2011, arXiv e-prints, arXiv:1106.3343

Herbig, G. H. 1977, ApJ, 217, 693

Herbst, W., Bailer-Jones, C. A. L., & Mundt, R. 2001, ApJ, 554, L197

Jeans, J. H. 1902, Philosophical Transactions of the Royal Society of London Series A, 199, 1

Kamp, I. & Dullemond, C. P. 2004, ApJ, 615, 991

Kippenhahn, R., Weigert, A., & Weiss, A. 2012, Stellar Structure and Evolution (Springer-Verlag Berlin Heidelberg, 2012)

Landau, L. D. & Lifschitz, E. M. 2019, Lehrbuch der theoretischen Physik, Band 6, Hydrodynamik (Verlag Europa-Lehrmittel)

Latter, H. N. & Balbus, S. 2012, MNRAS, 424, 1977

Lee, S., Lee, J.-E., Park, S., et al. 2016, ApJ, 826, 179

Lesur, G., Kunz, M. W., & Fromang, S. 2014, AAP, 566, A56

LeVeque, R. J. 2002, Finite Volume Methods for Hyperbolic Problems (Camebridge University Press)

LeVeque, R. J., Mihalas, D., Dorfi, E. A., & Müller, E. 1997, Astrophysics of Planet Formation (Saas-Fee Advanced Course 27. Lecture Notes 1997 Swiss Society for Astrophysics and Astronomy)

Lin, D. N. C. & Pringle, J. E. 1987, MNRAS, 225, 607

Lynden-Bell, D. & Pringle, J. E. 1974, MNRAS, 168, 603

Mamajek, E. E., Torres, G., Prsa, A., et al. 2015, arXiv e-prints, arXiv:1510.06262

McKee, C. F. & Ostriker, E. C. 2007, ARAA, 45, 565

Mihalas, D. & Binney, J. 1981, Galactic astronomy: Structure and kinematics /2nd edition/

Mo, H., van den Bosch, F., & White, S. 2010, Computational Methods for Astrophysical Fluid Flow (Cambridge University Press)

Nayakshin, S. & Lodato, G. 2012, MNRAS, 426, 70

Omukai, K., Nishi, R., Uehara, H., & Susa, H. 1998, Progress of Theoretical Physics, 99

Palla, F. & Stahler, S. W. 1991, ApJ, 375, 288

Parker, E. N. 1966, ApJ, 145, 811

Parker, E. N. 1967, ApJ, 149, 535

Pringle, J. E. 1981, ARAA, 19, 137

Rafikov, R. R. 2017, ApJ, 837, 163

Ragossnig, F., Dorfi, E., Ratschiner, B. W., et al. 2019a, 1+1D implicit disk computations (in preparation)

Ragossnig, F., Gehrig, L., Dorfi, E., Steiner, D., & Stoekl, A. 2019b, Mass limits for stationary protoplanetary accretion disks

Rees, M. J. & Ostriker, J. P. 1977, Monthly Notices of the Royal Astronomical Society, 179, 541

Riols, A. & Lesur, G. 2018, AAP, 617, A117

Samus, N. N., Kazarovets, E. V., & Durlevich, O. V. 2001, Odessa Astronomical Publications, 14, 266

Semkov, E. H., Peneva, S. P., & Ibryamov, S. I. 2017, Bulgarian Astronomical Journal, 26, 57

Semkov, E. H., Peneva, S. P., Ibryamov, S. I., & Dimitrov, D. P. 2014, Bulgarian Astronomical Journal, 20, 59

Semkov, E. H., Peneva, S. P., Munari, U., et al. 2012, AAP, 542, A43

Shakura, N. I. & Sunyaev, R. A. 1973, A&A, 24, 337

Stoekl, A. & Dorfi, E. 2014, in EGU General Assembly Conference Abstracts, Vol. 16, EGU General Assembly Conference Abstracts, 2472

Stökl, A. & Dorfi, E. A. 2014, in Search for Life Beyond the Solar System. Exoplanets, Biosignatures AMP Instruments, ed. D. Apai & P. Gabor, P2.7

Tey, W. Y., Asako, Y., Che Sidik, N. A., & Rui-Zher, G. 2017

Toomre, A. 1964, ApJ, 139, 1217

Tscharnuter, W. M. & Winkler, K.-H. A. 1979, Computer Physics Communications, 18, 171

Turner, N. J., Fromang, S., Gammie, C., et al. 2014, in Protostars and Planets VI, ed. H. Beuther, R. S. Klessen, C. P. Dullemond, & T. Henning, 411

Turner, N. J. J., Bodenheimer, P., & Bell, K. R. 1997, ApJ, 480, 754

van Leer, B. 1977, Journal of Computational Physics, 23, 276

Vorobyov, E. I. 2010, ApJ, 723, 1294

Vorobyov, E. I. & Basu, S. 2007, Monthly Notices of the Royal Astronomical Society, 381, 1009

Vorobyov, E. I. & Pavlyuchenkov, Y. N. 2017, AAP, 606, A5

Yorke, H. W. & Bodenheimer, P. 1999, ApJ, 525, 330

Zhu, Z., Hartmann, L., Calvet, N., et al. 2007, ApJ, 669, 483

Zhu, Z., Hartmann, L., Calvet, N., et al. 2008, ApJ, 684, 1281

Zhu, Z., Hartmann, L., Gammie, C. F., et al. 2010, ApJ, 713, 1134